



Develop Rapid Quality Control and Assurance Technologies for Pavements: Phase II Report

Technical Report 0-6874-R2

Cooperative Research Program

TEXAS A&M TRANSPORTATION INSTITUTE
COLLEGE STATION, TEXAS

in cooperation with the
Federal Highway Administration and the
Texas Department of Transportation
<http://tti.tamu.edu/documents/0-6874-R2.pdf>

1. Report No. FHWA/TX-21/0-6874-R2		2. Government Accession No.		3. Recipient's Catalog No.	
4. Title and Subtitle DEVELOP RAPID QUALITY CONTROL AND ASSURANCE TECHNOLOGIES FOR PAVEMENTS: PHASE II REPORT				5. Report Date Published: September 2021	
				6. Performing Organization Code	
7. Author(s) Bill Crockford, Yong Deng, Arvind Devadas, Fan Gu, Soohyok Im, Alireza Joshaghani, Wenting Liu, Xue Luo, Bob Lytton, Younho Rew, Sajib Saha, Stephen Sebesta, and Bryan Wilson				8. Performing Organization Report No. Report 0-6874-R2	
9. Performing Organization Name and Address Texas A&M Transportation Institute College Station, Texas 77843-3135				10. Work Unit No. (TRAIS)	
				11. Contract or Grant No. Project 0-6874	
12. Sponsoring Agency Name and Address Texas Department of Transportation Research and Technology Implementation Office 125 E. 11th Street Austin, Texas 78701-2483				13. Type of Report and Period Covered Technical Report	
				14. Sponsoring Agency Code	
15. Supplementary Notes Project performed in cooperation with the Texas Department of Transportation and the Federal Highway Administration. Project Title: Develop Nondestructive Rapid Pavement Quality Assurance/Quality Control Evaluation Test Methods and Supporting Technology URL: http://tti.tamu.edu/documents/0-6874-R2.pdf					
16. Abstract This project expanded on the technology readiness of three non-destructive tools for potentially enhancing quality inspection, asset management, or forensic investigations in flexible pavements. These tools included mechanics-based models for base course, compaction monitoring system (CMS) for asphalt mixture process control, and ground penetrating radar (GPR) for asphalt mixture construction quality assessment. The mechanics-based models showed good promise for measuring density and moisture content of the base course. Results showed estimating flexible base course modulus at a controlled test site tracked reasonably with the falling weight deflectometer (FWD) with an average error of about 14 ksi or less. The mechanics-based models did not work well on non-plastic base layers. On new pavements, the FWD shows more variability than the modulus predictions from mechanics-based results. The CMS provides real-time feedback of the adequacy of breakdown roller coverage, but the concept to estimate mat density from the CMS proved quite complex. Even after development of revised model factors, the ability of the CMS to estimate density is limited. The best potential use of the CMS is likely in process control to provide continuous feedback with far more testing coverage than routine use of a density gauge. The use of GPR for measuring asphalt mixture density has a high technology readiness. Applications in both construction and forensic settings show strong potential, and this tool should be viable for some form of implementation.					
17. Key Words Quality Control, Quality Assurance, Flexible Base, Resilient Modulus, Permanent Deformation, SWCC, Dielectric Constant, FWD, GPR, HMA, Asphalt Mixture, Compaction Monitoring				18. Distribution Statement No restrictions. This document is available to the public through NTIS: National Technical Information Service Alexandria, Virginia http://www.ntis.gov	
19. Security Classif. (of this report) Unclassified		20. Security Classif. (of this page) Unclassified		21. No. of Pages 106	
				22. Price	

DEVELOP RAPID QUALITY CONTROL AND ASSURANCE TECHNOLOGIES FOR PAVEMENTS: PHASE II REPORT

by

Bill Crockford, P.E.
Research Engineer
Texas A&M Transportation Institute

Xue Luo, Ph.D.
Assistant Research Scientist
Texas A&M Transportation Institute

Yong Deng
Graduate Assistant - Research
Texas A&M Transportation Institute

Bob Lytton, Ph.D., P.E.
Research Engineer
Texas A&M Transportation Institute

Arvind Devadas
Research Specialist I
Texas A&M Transportation Institute

Younho Rew, Ph.D.
Postdoctoral Research Assistant
Texas A&M Transportation Institute

Fan Gu, Ph.D.
Post Doctoral Research Associate
Texas A&M Transportation Institute

Sajib Saha
Graduate Assistant Researcher
Department of Civil Engineering
Texas A&M University

Soohyok Im, Ph.D., P.E.
Pavement Engineer
Texas Department of Transportation

Stephen Sebesta
Research Scientist
Texas A&M Transportation Institute

Alireza Joshaghani
Graduate Assistant – Research
Texas A&M Transportation Institute

and

Wenting Liu, P.E.
Research Engineer
Texas A&M Transportation Institute

Bryan Wilson
Associate Research Scientist
Texas A&M Transportation Institute

Report 0-6874-R2

Project 0-6874

Project Title: Develop Nondestructive Rapid Pavement Quality Assurance/Quality Control
Evaluation Test Methods and Supporting Technology

Performed in cooperation with the
Texas Department of Transportation
and the
Federal Highway Administration

Published: September 2021

TEXAS A&M TRANSPORTATION INSTITUTE
College Station, Texas 77843-3135

DISCLAIMER

This research was performed in cooperation with the Texas Department of Transportation (TxDOT) and the Federal Highway Administration (FHWA). The contents of this report reflect the views of the authors, who are responsible for the facts and the accuracy of the data presented herein. The contents do not necessarily reflect the official view or policies of the FHWA or TxDOT. This report does not constitute a standard, specification, or regulation.

ACKNOWLEDGMENTS

This project was conducted in cooperation with TxDOT and FHWA. The authors thank the TxDOT technical committee: Gisel Carrasco, Yvette Flores, Miles Garrison, Stephen Kasberg, Enad Mahmoud, Andy Naranjo, Travis Patton, Jimmy Si, and Stacey Strittmatter, and the TxDOT project managers: Sonya Badgley, Chris Glancy, and James Kuhr.

TABLE OF CONTENTS

	Page
List of Figures.....	ix
List of Tables	xi
Chapter 1. Use of Mechanics Based Models to Measure Flexible Base Quality	1
Background.....	1
Procedures.....	1
GPR Signal Pre-Processing.....	1
Filtering.....	1
Surface Normalization	2
Height Correction.....	2
Thin Layer Subtraction	2
Thickness, Dielectric, and Conductivity Calculations.....	2
Thickness and Dielectric Constant.....	2
Conductivity.....	3
Pavement Layer Composition Calculations.....	5
Self-Consistent Model	5
LayerMAPP	6
Supporting Lab Tests	6
Identification of Suitable Commercial GPR Systems.....	6
Results.....	7
Suitable GPR Systems	7
Pavement Test Site Results	7
Conclusions.....	17
Chapter 2. Compaction Monitoring for Quality Control during Asphalt Mixture	
Construction	19
Background.....	19
Procedures.....	19
Form Factor Development	19
Deployment of CMS on Test Sites	19
Density Prediction Model Development.....	20
Results.....	21
Form Factor Development	21
RELLIS Test Site Results	23
Construction Project Testing.....	35
Overall Results from Construction Project Deployments.....	38
Density Prediction Model Development.....	39
Conclusions.....	39
Chapter 3. High Frequency Ground-Penetrating Radar for Density of Asphalt	
Mixture Construction	41
Background.....	41
Procedures.....	41
New Construction	42
Forensic Investigations	43
Laboratory Sensitivity Analysis of Mixture Variability	43

Results.....	46
Shadow Quality Assurance Testing on New Construction	46
Forensic Testing.....	49
Laboratory Sensitivity Testing.....	52
Conclusions.....	54
Chapter 4. Conclusions.....	55
Mechanics Based Models for Base Course.....	55
Compaction Monitoring System	55
GPR for Asphalt Mixture Construction Quality	56
Appendix A. Test Plan for RELLIS Test Site with Compaction Monitoring System	57
Rolling Patterns for Asphalt Layers.....	57
Field Tests and Laboratory Tests.....	58
Density Tests on Asphalt Layers	59
Appendix B. Schedule of RELLIS Test Site Activities	63
Appendix C. Construction Activities for Pavement Layers at RELLIS Test Site.....	65
Subgrade	65
Lime Treated Subgrade.....	65
Flexible Base.....	67
Type-D Asphalt Layer	67
Thin Overlay Mix-F (TOM-F) Asphalt Layer	69
Appendix D. Compaction Index Model Development	71
Drum Factor	71
Temperature Factor	71
Vibration Factor	74
Lab Compaction Index.....	76
Appendix E. Test Details of GPR for Asphalt Mixture Construction	79

LIST OF FIGURES

	Page
Figure 1. Illustration of Normal Incidence Reflection.....	3
Figure 2. Modulus of Base, RELLIS Site, Sept 2017 and April 2018.....	7
Figure 3. Base Modulus at RELLIS Site from GPR (Blue) and FWD (Red).....	8
Figure 4. Estimated Dry Density with Distance, RELLIS Site, April 2018.	8
Figure 5. Base Dry Density and Moisture Content, RELLIS Site, April 2018.....	9
Figure 6. Modulus of Base, RELLIS Site, February 2019.....	9
Figure 7. Testing FM 159, April 2019.....	10
Figure 8. Estimated Dry Density with Distance, FM 159, April 2019.	10
Figure 9. Modulus with Distance, FM 159, April 2019.	11
Figure 10. Modulus with Distance, FM 159, June 2019.....	11
Figure 11. GPR Collection on SH 130 for Mechanics-Based Models.	12
Figure 12. Combined Effects of Evaporable Volumetric Water Content and Stabilizer Content on (a) Dielectric Constant; and (b) Electrical Conductivity.....	13
Figure 13. (a) Intersection Line between GPR Dielectric Constant Plane and Laboratory Measured Dielectric Constant Surface; and (b) Intersection Line between GPR Scanned Electrical Conductivity Plane and Laboratory Measured Electrical Conductivity Surface.	13
Figure 14. Estimating Percentage Stabilizer from Coinciding Point of Dielectric Constant and Electrical Conductivity Planes.	14
Figure 15. Illustration of Radar Waves with Non-normal Incident Angles.....	14
Figure 16. Layout of RELLIS Test Site.....	20
Figure 17. PLC System for Compaction Monitoring System.....	21
Figure 18. HMI Display for CMS.....	22
Figure 19. RTK vs. WAAS Coordinates.	22
Figure 20. CMS Testing at RELLIS Test Site.	23
Figure 21. Weighting Factor for Drum Position.	24
Figure 22. CMS Mapping of Roller Operations on Type-D Mix at Flexible Site.....	26
Figure 23. CMS Mapping of Roller Operations on Type-D Mix at Rigid Site.	26
Figure 24. Means Plot – D Mix, Sections Tested with PLC System.	27
Figure 25. Means Plot – D Mix, Sections Tested with PC System.	28
Figure 26. Observed versus Predicted Air Voids, D Mix, Tested with PC System.....	29
Figure 27. Track Data for TOM-F Compaction.....	30
Figure 28. Means Plot – TOM-F, Sections Tested with PLC System.	31
Figure 29. Observed versus Predicted Air Voids, TOM-F, Tested with PLC System.	33
Figure 30. Means Plot, TOM-F, Sections Tested with PC System.	33
Figure 31. Observed versus Predicted Air Voids, TOM-F, Tested with PC System.....	35
Figure 32. SH 77 Density and Core Locations.	36
Figure 33. IH 45 Density and Core Locations.	36
Figure 34. CMS Test Activities on FM 158.	37
Figure 35. FM 158 Density and Core Locations.....	37
Figure 36. SH 40 Density and Core Locations.	38
Figure 37. Core Density Results versus Compaction Index from All Projects.	39

Figure 38. GPR System for Measuring Density of Asphalt Mixture Construction.	41
Figure 39. Using GPR for Forensic Investigation.	43
Figure 40. Surface Dielectric Profiling on Lab Slabs.	45
Figure 41. Calibrations to Air Voids from GPR for All Projects.	46
Figure 42. Predicted vs Actual Air Voids.	47
Figure 43. Examples of Non-Biased (Left) and Biased (Right) Predictions.	47
Figure 44. Example Distribution of Air Voids by Sublot: (a) SH 6-Valley Mills and (b) IH 45-Hunstville.	48
Figure 45. Example Air Voids Heat Maps for SS 248-Tyler: (a) Built-in Software and (b) Mapping Software after Post-Processing.	49
Figure 46. Dielectric to Air Voids Calibration for US 287.	50
Figure 47. Overall Air Voids Distributions for US 287.	50
Figure 48. Excerpt from Air Void Distribution Map for US 287.	51
Figure 49. Calibration of Air Voids to GPR on SS 248.	52
Figure 50. Layout for Test Section Compaction Levels.	57
Figure 51. Density and Core Locations in Flexible Pavement Section.	60
Figure 52. Density and Core Locations in Rigid Pavement Test Section.	61
Figure 53. Subgrade Layer Construction.	65
Figure 54. Construction of LTS Layer.	66
Figure 55. Construction Process of Flexible Base Layer.	67
Figure 56. Type-D Placement at Flexible Pavement Test Section.	68
Figure 57. Type-D Placement at Rigid Pavement Test Section.	69
Figure 58. TOM-F Placement.	70
Figure 59. Revised Drum Efficiency Factor.	71
Figure 60. Temperature Factor Curve for IH 45 SMA Mix.	72
Figure 61. Temperature Factor Estimates Derived from Lab Compaction.	73
Figure 62. Recommended General Temperature Factor.	74
Figure 63. Type D Mix Vibration Factor Development.	75
Figure 64. TOM F Mix Vibration Factor Development.	75
Figure 65. Vibration Factor Development (All RELLIS Sections Combined).	76
Figure 66. Example SGC Compaction Curves for Developing LCI.	77
Figure 67. Correlation between LCI and CI.	77

LIST OF TABLES

	Page
Table 1. Nuclear and PaveSCM Density and Moisture, FM 159, April 2019.....	10
Table 2. Nuclear and PaveSCM Density and Moisture, SH 130, July 2019.	12
Table 3. Analysis of Variance for D Mix Core Air Voids from PLC System.....	27
Table 4. Analysis of Variance, D Mix Air Voids, Tested with PC System.....	28
Table 5. Type III Sums of Squares, D Mix Air Voids, Tested with PC System.	28
Table 6. Multiple Comparisons for TOM-F Air Voids, Sections Tested with PLC System.	31
Table 7. Analysis of Variance, TOM-F Air Voids, Tested with PLC System.	31
Table 8. Type III Sums of Squares, TOM-F Air Voids, Tested with PLC System.	32
Table 9. Multiple Comparisons TOM-F Air Voids, Sections Tested with PC System.	34
Table 10. Analysis of Variance, TOM-F Air Voids, Tested with PC System.....	34
Table 11. Type III Sums of Squares, TOM-F Air Voids, Tested with PC System.....	34
Table 12. Asphalt Mixture Summaries.	42
Table 13. Asphalt Mixture Summary for Forensic Projects.	43
Table 14. Production Summary and Expected Project Variance.....	44
Table 15. Baseline Mixture Designs for Lab Mixture Variability Study.	44
Table 16. Example Test Plan for One Mixture in Lab Variability Study.	45
Table 17. ANOVA Response Variable and Model Factors.....	46
Table 18. Example Summary Statistics of Air Voids on Two Projects.....	48
Table 19. Percent within Placement Categories for SS 248, between Wheel Paths Only.	52
Table 20. Summary of Dielectric Sensitivity Study.	53
Table 21. Application of Sensitivity Results.	54
Table 22. Rolling Patterns Used for Asphalt Layers.	58
Table 23. Field Tests on RELIS Pavement Test Site.	58
Table 24. Lab Tests on Cores and Loose Asphalt Mixtures.	59
Table 25. Daily Activity Record.....	63

CHAPTER 1. USE OF MECHANICS BASED MODELS TO MEASURE FLEXIBLE BASE QUALITY

BACKGROUND

Construction variability and isolated defects can be limiting factors in a pavement life. Ensuring quality construction of pavements currently uses small sample sizes, often missing defect areas. Using ground penetrating radar (GPR) for construction quality assurance and control and for condition or asset management applications could collect data at highway speeds and thus not pose safety hazards associated with either stationary or slowly moving testing methods. GPR also could provide detailed and closely spaced information nondestructively, which gives a much more complete picture of the condition of a pavement than is provided by the various sampling methods.

This chapter describes approaches to use GPR for evaluating the quality of construction and for performing asset management measurements on in-service pavements. Successful applications of GPR for require (1) equipment with all of the needed capabilities; (2) data collection methods that will provide the most accurate measurements; (3) supporting laboratory methods to provide materials properties that are needed to convert analyzed GPR data into useful engineering and construction information; and (4) analytical methods that can convert the raw GPR data into the material properties. This chapter describes approaches to use GPR for measuring base material properties including modulus, moisture content, and density.

PROCEDURES

GPR Signal Pre-Processing

Before readings of dielectric constant, thickness or any other pavement properties are estimated from a GPR scan, the raw GPR scan needs to be pre-processed. Pre-processing of the raw GPR scans helps remove background noise in the signals, reduce the effects of the antenna height variation due to the bounce of the vehicle while driving, and enables more accurate identification of layer interfaces. The pre-processing of the raw GPR scan is performed using the following methods:

- Filtering of the radar signals.
- Surface normalization.
- Height variation correction of signal amplitude.
- Thin-layer subtraction.

Filtering

Raw GPR scans can contain low and/or high frequency noise that would need to be removed. The low and high frequency noise can be removed by applying bandpass filters. The frequency of the bandpass filter will depend on the frequency of the GPR antenna.

Surface Normalization

The height of the antenna(s) can change due to the bounce of the vehicle during a scan. This height change results in the surface reflection of the signal to vary along the length of the scan. A surface normalization repositions the surface echo so that all the signals in the scan have the surface reflection located at the same depth (i.e., time). As a result, the variation of the position of the signal due to the antenna height variation is removed.

Height Correction

The variation in height of the antenna caused by vehicle bounce during a scan also affects the amplitude of the signal. When the antenna gets closer to the pavement the signal amplitude increases, and when the antenna is farther away from the pavement the signal amplitude decreases. This variation in antenna height which in turn affects the signal amplitude is corrected by applying a bounce correction.

Thin Layer Subtraction

The thin-layer subtraction allows identifying top layer(s) whose thickness is under 2 or 3 inches and also reduces background noise in the raw GPR signal. The thin-layer subtraction is performed by subtracting the raw GPR signal from the signal recorded over a metal plate.

THICKNESS, DIELECTRIC, AND CONDUCTIVITY CALCULATIONS

The mechanics-based approaches for using GPR to calculate base material properties begin with requiring a good GPR signal, and then largely relying on computation of thickness, dielectric, and conductivity measurements acquired by processing the GPR signals.

Thickness and Dielectric Constant

To calculate the thickness, the dielectric constant of each layer needs to be calculated first. The dielectric constant, ϵ , for a layer is calculated using these formulae:

$$\epsilon_i = \epsilon_{i-1} \times \left(\frac{1+\rho}{1-\rho} \right)^2 \quad (1)$$

where,

i – Layer number

When $i = 0$ the layer is air, the $\epsilon_0 = 1.0$

$$\rho_i = \frac{k_a \times \frac{A_i}{IA}}{T_i} \quad (2)$$

In which,

ρ_i – Reflection coefficient

k_a – Calibration amplitude correction factor

A_i – Layer amplitude

IA – Incident amplitude

$$T_i = T_{i-1} \times \frac{4 \times \sqrt{\epsilon_{i-1} \times \epsilon_i}}{(\sqrt{\epsilon_{i-1}} + \sqrt{\epsilon_i})^2} \quad (3)$$

where,

T_i – Transmission coefficient

When $i = 1$, $T_1 = 1.0$

The thickness of the layers is calculated using this formula:

$$Thickness = 5.9 \times \frac{(\Delta t + k_t)}{\sqrt{\epsilon_i}} \quad (4)$$

where,

$Thickness$, in inches

Δt – Time delay, in nano-seconds

k_t – Calibration time correction factor

The correction factors k_t and k_a are calculated using a ground-truth thickness from a core, with the GPR signal having been recorded precisely over the core location. The correction factor k_t is usually needed to be used for pavements with thin surface layers.

Conductivity

When using GPR to measure the conductivity, the angle of the GPR signal wave traveling from the antenna and reflecting from the pavement will affect the calculations. Two forms of angles are used in doing the calculations. One uses a perpendicular propagation of the GPR signal wave in reference to the ground, and the other uses a non-normal propagation.

In the non-normal incidence, the spacing of the transmitter and the receiver in the antenna, along with the height of the antenna from the ground are used as illustrated in Figure 1. This non-normal incidence of the GPR signal is especially useful in calculating the electrical conductivity of the pavement layer.

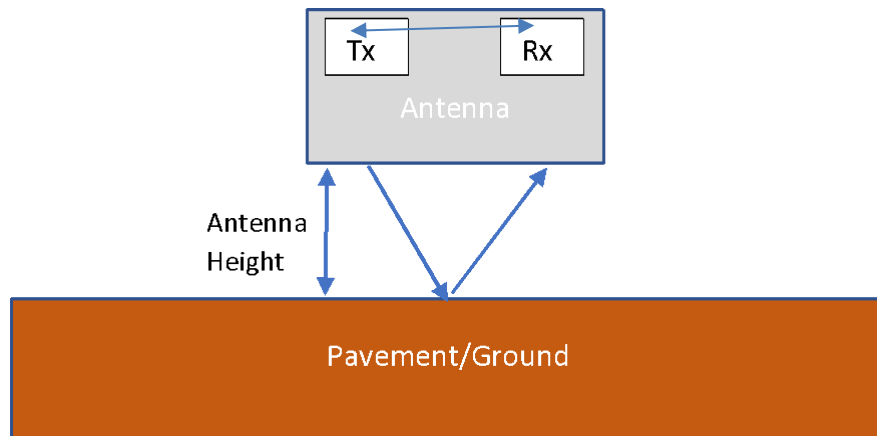


Figure 1. Illustration of Normal Incidence Reflection.

The calculations shown below are used to determine the surface electrical conductivity, the units of which are Siemens per meter. The analysis first requires that the dielectric constant is determined, and then the conductivity is calculated using the calculated dielectric constant and the angle of incidence:

$$\theta = \tan^{-1} \left(\frac{\left(\frac{\text{Antenna Spacing}}{2} \right)}{\text{Antenna Height}} \right) \quad (5)$$

where,

Antenna Spacing – Spacing between the transmitter and receiver of the antenna

Antenna Height – Height of the antenna from the ground surface

θ – Angle of incidence

$$b = \left(\frac{1}{\sin^2 \theta} \right) \times \left(\varepsilon_1 - \frac{\cos^2 \theta}{\varepsilon_1} \right) \quad (6)$$

where,

ε_1 – Dielectric constant of surface layer

$$\text{term}_{\omega E} = \frac{\varepsilon_1 \times 10^{-9}}{36\pi} \cdot 2 \cdot \pi \cdot f_{\text{Antenna}} \quad (7)$$

where,

f_{Antenna} – Frequency of antenna

$\text{term}_{\omega E}$ – Frequency $\left(\frac{\text{radians}}{\text{sec}} \right) \times$ Permittivity term

$$\text{term}_{bn} = b + \frac{1-2b}{n^2} \quad (8)$$

where,

n – Calculated constant (3×10^{-4} for base course)

$$\sigma_{\text{Positive}} = \text{term}_{\omega E} \times \sqrt{\frac{n^4}{2b} \cdot \text{term}_{bn} \cdot \left(-1 + \sqrt{1 - \frac{4 \cdot (b-1)}{\frac{n^4}{b} \cdot \text{term}_{bn}^2}} \right)} \quad (9)$$

where,

σ_{Positive} – Conductivity, positive term

$$\sigma_{\text{Negative}} = \text{term}_{\omega E} \times \sqrt{\frac{n^4}{2b} \cdot \text{term}_{bn} \cdot \left(-1 - \sqrt{1 - \frac{4 \cdot (b-1)}{\frac{n^4}{b} \cdot \text{term}_{bn}^2}} \right)} \quad (10)$$

where,

σ_{Negative} – Conductivity, negative term

PAVEMENT LAYER COMPOSITION CALCULATIONS

Self-Consistent Model

A pavement self-consistent model, or PaveSCM, was used on this work to calculate pavement layer compositional properties.

For asphalt layers the self-consistent micro-mechanics model's formula is:

$$f = \theta_s \times \left(\frac{\varepsilon_s - \varepsilon}{\varepsilon_s + 2\varepsilon} \right) + \theta_{as} \times \left(\frac{\varepsilon_{as} - \varepsilon}{\varepsilon_{as} + 2\varepsilon} \right) + \theta_a \times \left(\frac{\varepsilon_a - \varepsilon}{\varepsilon_a + 2\varepsilon} \right) \doteq 0 \quad (11)$$

where,

- f – Caps-f, this should be close to zero
- θ_s – Volumetric concentration of solids
- θ_{as} – Volumetric concentration of asphalt
- θ_a – Volumetric concentration of air
- ε_s – Dielectric constant of solids
- ε_{as} – Dielectric constant of asphalt
- ε_a – Dielectric constant of air, 1.0
- ε – Dielectric constant of the layer measured using GPR

For concrete, base course and soil layers the model's formula is:

$$f = \theta_s \times \left(\frac{\varepsilon_s - \varepsilon}{\varepsilon_s + 2\varepsilon} \right) + \theta_w \times \left(\frac{\varepsilon_w - \varepsilon}{\varepsilon_w + 2\varepsilon} \right) + \theta_a \times \left(\frac{\varepsilon_a - \varepsilon}{\varepsilon_a + 2\varepsilon} \right) \doteq 0 \quad (12)$$

where,

- f – Caps-f, this should be close to zero
- θ_s – Volumetric concentration of solids
- θ_w – Volumetric concentration of water
- θ_a – Volumetric concentration of air
- ε_s – Dielectric constant of solids
- ε_w – Dielectric constant of water
- ε_a – Dielectric constant of air, 1.0
- ε – Dielectric constant of the layer measured using GPR

The PaveSCM method uses the core values and the dielectric constant measured using GPR at the core location to obtain the calibration parameters.

For asphalt layers, the calibration process consists of performing an exhaustive search for every possible combination of ε_s and ε_{as} . For concrete, base course, and soil layers, the exhaustive search is done for every possible combination of ε_s , ε_w and G_s . This exhaustive search is done in two steps. In the first step, the exhaustive search is done using coarse increment of the calibration parameters, and for each set of the parameters the caps-f value is determined. Then the set of calibration parameters that produced the lowest caps-f value is recorded.

In the second step of the exhaustive search, the calibration parameters from the coarse method are then searched using finer increments. Again the caps-f value is determined for each combination of the calibration parameters. In the fine-tune step, along with the caps-f criteria, a second criterion is

used based on the composite-dielectric constant. The composite-dielectric constant is calculated using the Newton-Raphson method:

$$a = \varepsilon_s \times (-1 + 3\theta_s) + \varepsilon_{air} \times (2 - 3\theta_s - 3\theta_f) + \varepsilon_f \times (-1 + 3\theta_f) \quad (13)$$

$$b = \varepsilon_s \varepsilon_{air} (2 - 3\theta_f) + \varepsilon_s \varepsilon_f \times (-1 + 3\theta_s + 3\theta_f) + \varepsilon_f \varepsilon_{air} \times (2 - 3\theta_s) \quad (14)$$

$$c = \varepsilon_s \varepsilon_f \varepsilon_{air} \quad (15)$$

$$\varepsilon_{comp-new} = \varepsilon_{comp} - \frac{(-4\varepsilon_{comp}^3 + 2a\varepsilon_{comp}^2 + b\varepsilon_{comp} + c)}{(-12\varepsilon_{comp}^2 + 4a\varepsilon_{comp} + b)} \quad (16)$$

The Newton-Raphson method involves iterating through the above equations until the change between $\varepsilon_{comp-new}$ and ε_{comp} is less than 1 percent.

LayerMAPP

A tool for measurement and analysis of pavement performance (LayerMAPP) was also used in this work for exploration in quality control or assurance applications. The primary goal of this tool is to use GPR, along with supporting lab tests, to estimate in-place resilient modulus of the base course.

Supporting Lab Tests

Prior project documentation (Phase I Report) presented the supporting lab tests used with the LayerMAPP approach. These supporting lab tests include: soil water characteristic curve (SWCC), measurement of dielectric constant and electrical conductivity in the lab with a percometer, laboratory moisture-density curve, percent fines content using particle size analyzer, methylene blue value, and aggregate imaging system.

IDENTIFICATION OF SUITABLE COMMERCIAL GPR SYSTEMS

Commercially available GPR system(s) that can be used with the PaveSCM and LayerMAPP tools are necessary if widespread implementation of the mechanics-based models from this project would be feasible. The criteria that the GPR systems need to meet have been broken down into new pavements and existing pavement applications:

- New Pavements:
 - Depth of penetration: 12–14 inches.
 - Layer consisting of same material.
 - Scan at highways speeds.
 - Able to scan simultaneously with 1–4 antenna systems.
 - GPR Antenna Frequency: 2 GHz.
- Existing Pavements:
 - Depth of penetration: 18–20 inches.
 - Multiple layers.
 - Scan at highways speeds.
 - Able to scan simultaneously with 1–4 antenna systems.
 - GPR Antenna Frequency: 1 GHz.

RESULTS

Researchers evaluated multiple possible GPR systems that may be suitable for use with the micromechanics models for base course. They deployed GPR systems on multiple projects representing both new construction/quality control and existing pavement/asset management applications. Exploratory work also was performed using the micromechanics tools on stabilized materials.

Suitable GPR Systems

After searching through 26 companies, based on availability and operating characteristics, researchers proceeded with evaluations using a 2 GHz system and a 2.5 GHz system manufactured by GSSI.

Pavement Test Site Results

Researchers evaluated pavement sections at a controlled test site, in-place new construction on a rehab project, and a stabilized base course in Phase II. Field tests for roadway applications of the mechanics-based models using the falling weight deflectometer (FWD), nuclear density testing, and collection of physical roadway materials for measurement of actual moisture content were used as much as possible for reference values. One pavement section also was only used for laboratory evaluation exploring the measurement of stabilizer content using micromechanics models.

Roadway Applications

In Phase II of this project, researchers deployed GPR tools and evaluated pavement sections using mechanics-based models at a controlled test site on Texas A&M's RELIS campus, on base course at a rehab project on FM159, and on a cement-treated base on SH 130.

RELIS Test Site Results

Researchers tested the RELIS site in September 2017, April 2018, and February 2019. Figure 2 shows the modulus of the base course estimated from LayerMAPP with the backcalculated modulus from the FWD. The data suggest three distinct zones of pavement base layer modulus and general tracking of the observed with the predicted values. The FWD backcalculations show more variability than the modulus predictions using mechanics-based models and GPR.

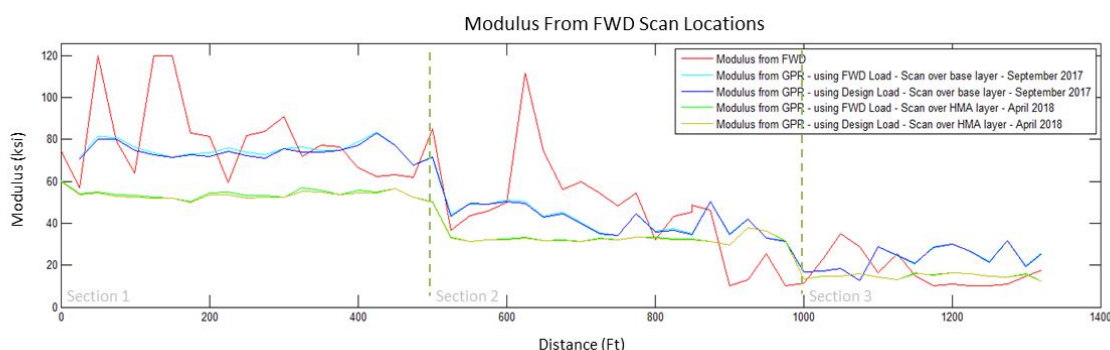


Figure 2. Modulus of Base, RELIS Site, Sept 2017 and April 2018.

Figure 3 illustrates the difference in the base course modulus from the FWD and the predicted values. The average difference is 14.5 ksi between the observed and predicted values.

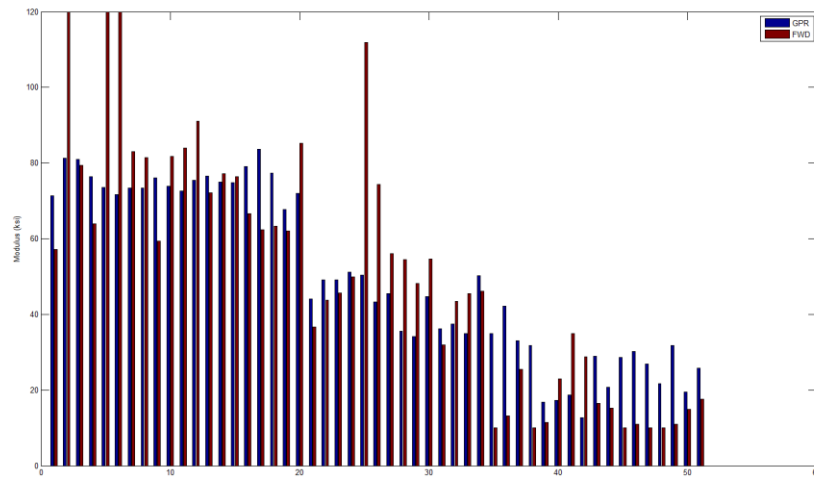


Figure 3. Base Modulus at RELLIS Site from GPR (Blue) and FWD (Red).

Figure 4 shows GPR-predicted density, with two reference values of measured density, from April 2018 using LayerMAPP. Although the number of validation points is limited, the results suggest reasonable agreement between actual and predicted values.

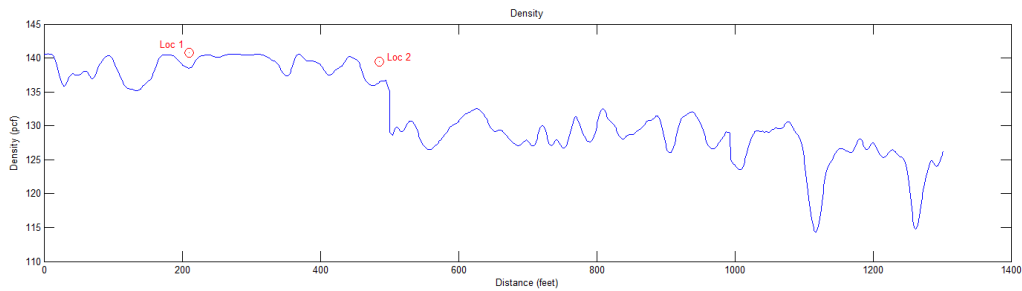


Figure 4. Estimated Dry Density with Distance, RELLIS Site, April 2018.

Figure 5 presents base composition properties estimated from PaveSCM with three reference values. The results suggest good agreement between actual and predicted values.

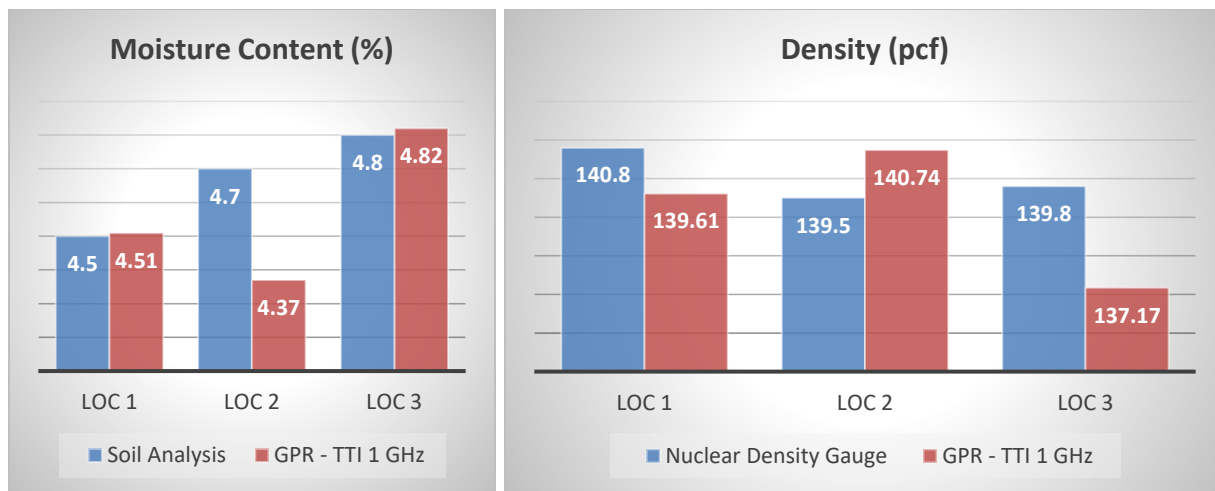


Figure 5. Base Dry Density and Moisture Content, RELLIS Site, April 2018.

Figure 6 presents the modulus with distance predicted from LayerMAPP and measured with the FWD in February 2019. At this time, the pavement was approximately 2 years old, and the data suggest that while three distinct zones of base modulus are still evident, the variability particularly under the FWD within each zone has decreased as the pavement reaches an equilibrium state.

At the February 2019 test date, the average difference between observed and predicted modulus was 6.4 ksi.

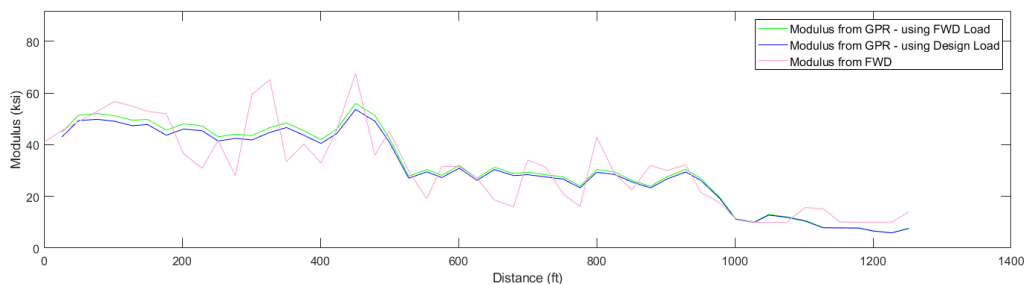


Figure 6. Modulus of Base, RELLIS Site, February 2019.

FM 159 Results

Researchers tested a 1500 ft section of FM 159 in April and again in June 2019. Tests in April were conducted on top of the exposed base surface, as illustrated in Figure 7. In June 2019, researchers tested on top of the surface treatment.



Figure 7. Testing FM 159, April 2019.

Table 1 shows GPR and nuclear gauge results from April 2019. The results show good agreement between observed and predicted values.

Table 1. Nuclear and PaveSCM Density and Moisture, FM 159, April 2019.

No.	Station or Marker	Distance (ft)	Dry Density (pcf)			Moisture Content (%)		
			Nuclear Gauge	PaveSCM	Error	Nuclear Gauge	PaveSCM	Error
1	Station - 373	196	128.4	129.3	0.9	5.91	5.77	0.1
2	Station - 369	597	131.3	130.3	1.1	6.27	5.92	0.3
3	Marker - 424	1121	124.1	122.4	1.8	7.48	6.04	1.4
4	Station - 361	1399	133.5	131.7	1.8	6.40	5.86	0.5

Figure 8 presents estimated density with distance. The red dots are locations of nuclear tests.

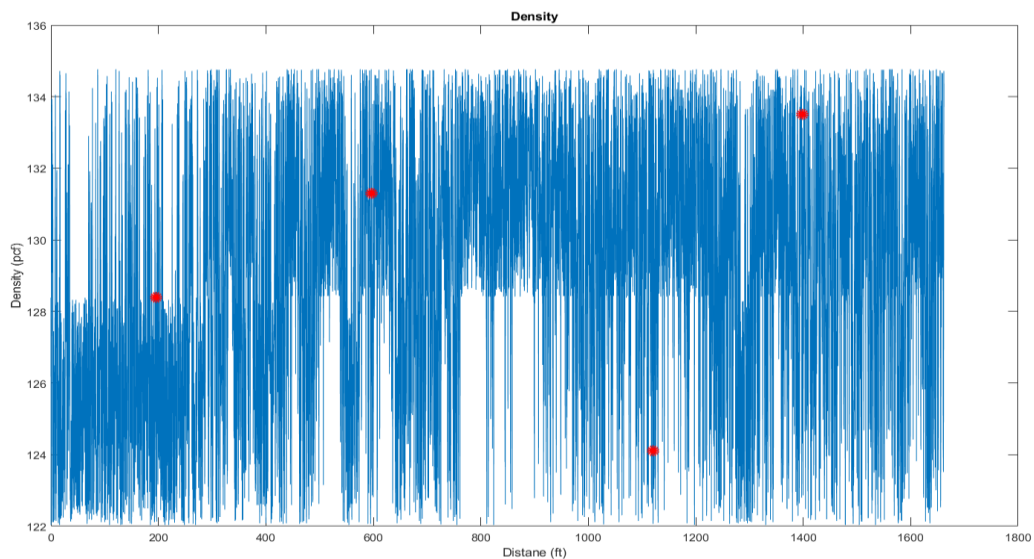


Figure 8. Estimated Dry Density with Distance, FM 159, April 2019.

To calculate the modulus of the base course layer, samples of the base were extracted and analyzed in the lab. Two of the measurements made in the lab are the methylene blue value and the percent fines content. These two parameters are used in the process of calculating the modulus in LayerMAPP. This base course was distinctively different from those that were originally used to develop the coefficients for the soil-water characteristic curve, soil-dielectric characteristic curve, the modulus model, and the compaction model in the LayerMAPP software. The FM 159 base course had a MBV of 0.0 and percent fines content (PFC) around 1.5 percent. Because of this, the methodology used in LayerMAPP could not be used. Researchers employed an alternate method to predict the modulus, and this method affected the calculations. Figure 9 presents the results with distance. The results suggest sporadic agreement, and in some zones significant disagreement, between the predicted and FWD-measured values.

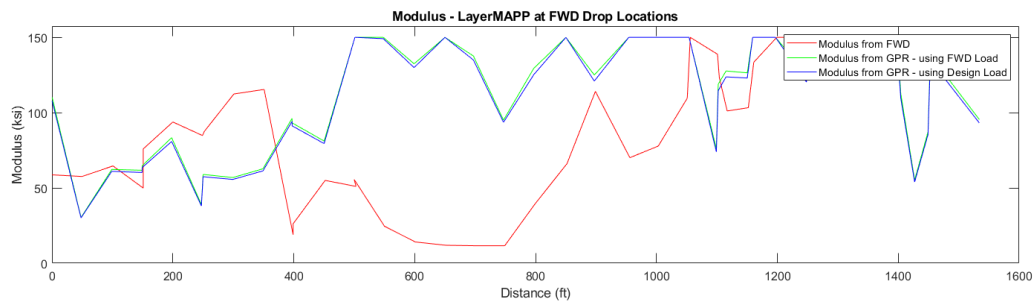


Figure 9. Modulus with Distance, FM 159, April 2019.

After placement of the surface treatment, researchers tested FM 159 again with the FWD and GPR. Figure 10 presents the results of modulus with distance. The results suggest significant disagreement between FWD and LayerMAPP-predicted over at least half the section.

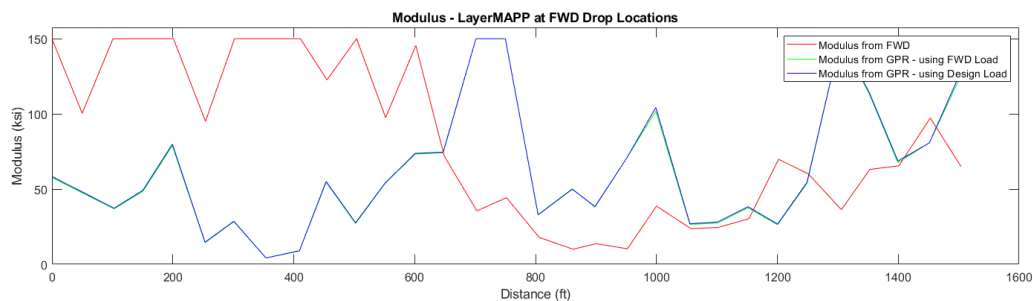


Figure 10. Modulus with Distance, FM 159, June 2019.

From GPR, the estimated surface thickness at the time of testing was 0.6 inches. Upon evaluation of the signals, researchers concluded a quality reflection was not obtained in the GPR at the surface/base interface, and that if using the 2 GHz system with the mechanics-based models, the asphalt thickness must exceed $\frac{3}{4}$ inch.

SH 130 Results

In July 2019, researchers evaluated a pugmill-mixed, cement-treated base on SH 130. Researchers used both 2 GHz and 2.5 GHz radar systems shown in Figure 11.



Figure 11. GPR Collection on SH 130 for Mechanics-Based Models.

Left: 2.5 GHZ; Right: 2 GHz

Table 2 presents measurements of dry density and moisture content using a nuclear gauge and predicted from PavSCM. The results show good agreement between observed and predicted values.

Table 2. Nuclear and PavSCM Density and Moisture, SH 130, July 2019.

No.	Station	Distance (ft)	Dry Density			Moisture Content (%)		
			Nuclear Gauge	GPR	Error	Nuclear Gauge	GPR	Error
1	Location 1	69	122.90	122.95	0.05	6.19	6.18	0.01
2	Location 2	284	123.90	124.15	0.25	6.05	6.07	0.02
3	Location 3	490	130.00	129.31	0.69	6.53	6.85	0.32
4	Location 4	682	126.40	127.52	1.12	6.10	6.50	0.40
5	Location 5	881	126.20	125.39	0.81	6.02	6.36	0.34

Laboratory Applications—US 259 Results

Part of Phase II in this project explored applications of micromechanics models and non-destructive GPR measurements for stabilized materials. A question that often arises is whether the proper dosage rate of stabilizer was applied to the material. Researchers used materials from US 259 to explore estimated stabilizer content from non-destructive tests (NDT).

Figure 12 presents a graphical approach of the determination of percentage of stabilizer in the base course. Different percentage of cement were added, and filter paper and percometer tests conducted to measure suction, dielectric constant, and electrical conductivity, respectively.

Figure 12(a) plots the dielectric constant surface showing the effects of both evaporable water content and cement stabilizer content. Figure 12(b) depicts the electrical conductivity surface

versus evaporable volumetric water content and stabilizer content. Both dielectric and conductivity show a proportional trend with water and stabilizer content.

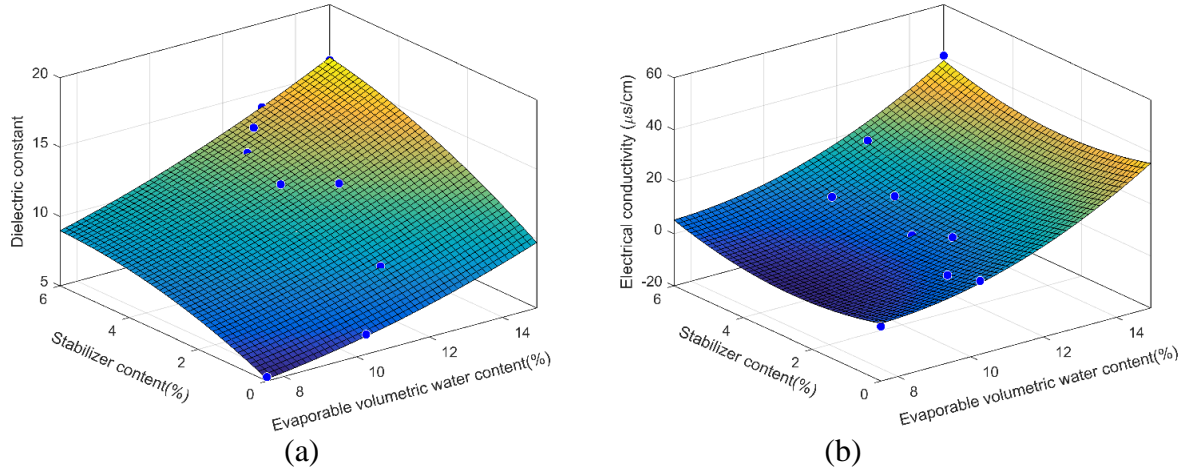


Figure 12. Combined Effects of Evaporable Volumetric Water Content and Stabilizer Content on (a) Dielectric Constant; and (b) Electrical Conductivity.

Figure 13 shows an example case of GPR-scanned dielectric and conductivity planes intersecting the surface of measured values.

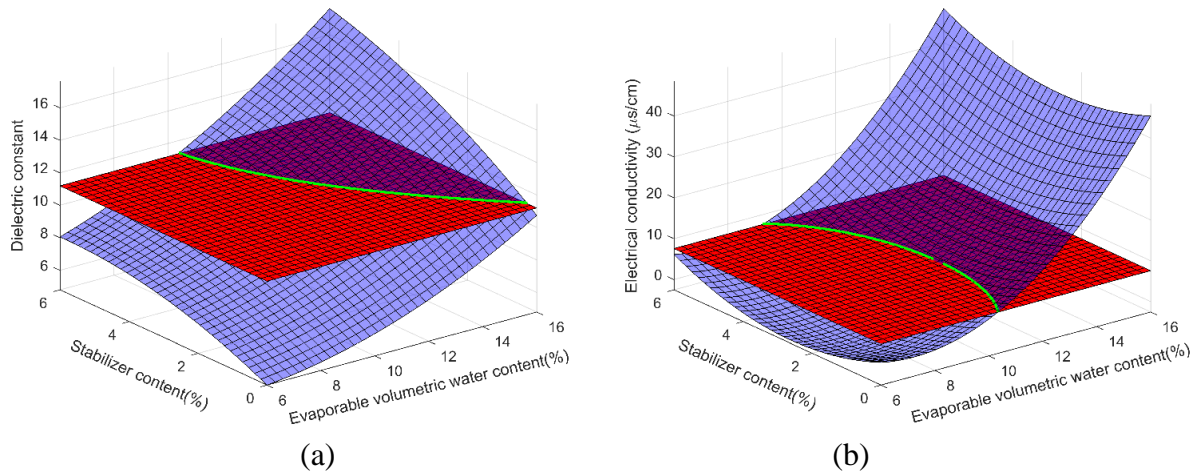


Figure 13. (a) Intersection Line between GPR Dielectric Constant Plane and Laboratory Measured Dielectric Constant Surface; and (b) Intersection Line between GPR Scanned Electrical Conductivity Plane and Laboratory Measured Electrical Conductivity Surface.

Figure 14 plots the intersecting line on the dielectric constant surface and electrical conductivity surface. Both lines are plotted together, and they intersect each other. That coinciding point depicts the predicted percentage of stabilizer in the field. If both dielectric constant and electrical conductivity could be rapidly measured in the field with GPR, near-full coverage estimation of stabilizer content may be possible.

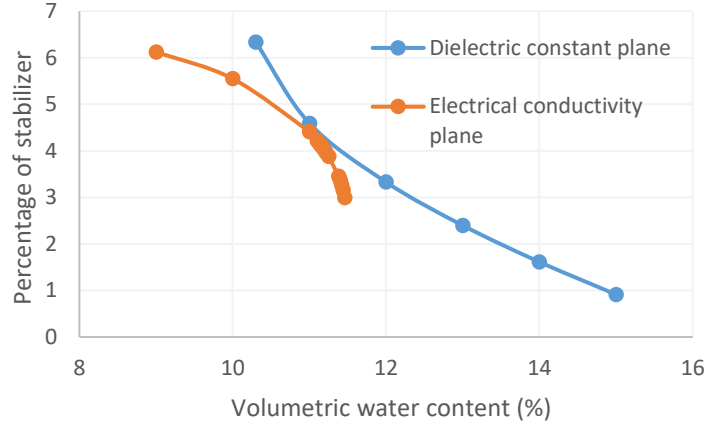


Figure 14. Estimating Percentage Stabilizer from Coinciding Point of Dielectric Constant and Electrical Conductivity Planes.

To support this potential application of GPR, researchers developed an analytical method to determine both dielectric constant and electrical conductivity from GPR surface reflections. Figure 15 illustrates the incidence of a non-normal radar wave at the intersection between two layers.

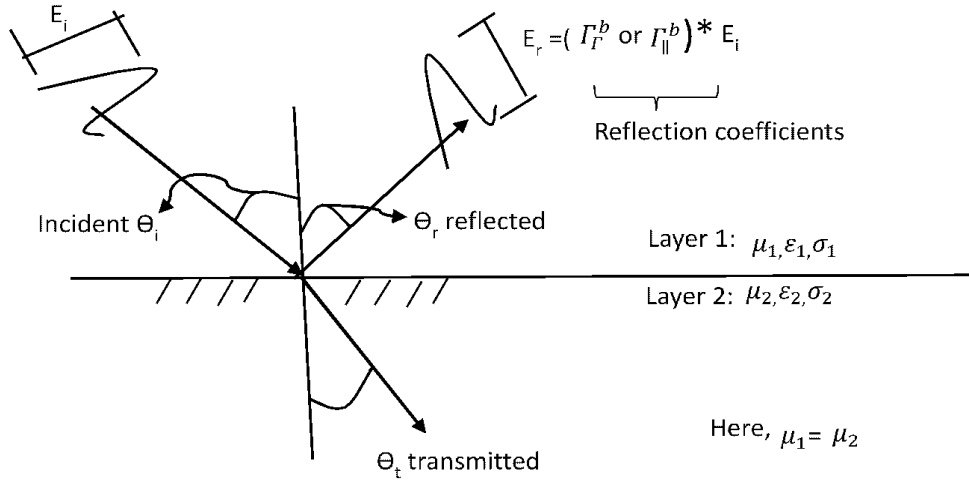


Figure 15. Illustration of Radar Waves with Non-normal Incident Angles.

From Balanis, C. A. (2012):

$$\alpha \cong \frac{\sigma}{2} \sqrt{\frac{\mu}{\epsilon}}, \text{ the attenuation constant} \quad (17)$$

$$\beta \cong \omega \sqrt{\mu \epsilon}, \text{ the phase constant} \quad (18)$$

where σ = electrical conductivity

μ = magnetic permeability

ϵ = dielectric constant

ω = frequency

The complex wave propagation constant, γ , includes the attenuation constant, α , and the phase constant, β .

$$\gamma = \alpha + i\beta \quad (19)$$

The non-normal incident reflection coefficient for a perpendicularly polarized GPR signal, Γ_{\perp}^b , is:

$$\Gamma_{\perp}^b = \frac{\sqrt{\frac{\mu_2}{\epsilon_2}} \cos \theta_i - \sqrt{\frac{\mu_1}{\epsilon_1}} \cos \theta_t}{\sqrt{\frac{\mu_2}{\epsilon_2}} \cos \theta_i + \sqrt{\frac{\mu_1}{\epsilon_1}} \cos \theta_t} \quad (20)$$

According to Snell's law:

$$\begin{aligned} \gamma_1 \sin \theta_i &= \gamma_2 \sin \theta_t \\ \left(\frac{\gamma_1}{\gamma_2}\right)^2 \sin^2 \theta_i &= \sin^2 \theta_t \\ [1 - \left(\frac{\gamma_1}{\gamma_2}\right)^2 \sin^2 \theta_i]^{1/2} &= \cos \theta_t \end{aligned} \quad (21)$$

where θ_i is the incident angle
 θ_t is the transmission angle

From Equation 20 and 21:

$$\Gamma_{\perp}^b = \frac{\sqrt{\frac{\mu_2}{\epsilon_2}} \cos \theta_i - \sqrt{\frac{\mu_1}{\epsilon_1}} [1 - \left(\frac{\gamma_1}{\gamma_2}\right)^2 \sin^2 \theta_i]^{1/2}}{\sqrt{\frac{\mu_2}{\epsilon_2}} \cos \theta_i + \sqrt{\frac{\mu_1}{\epsilon_1}} [1 - \left(\frac{\gamma_1}{\gamma_2}\right)^2 \sin^2 \theta_i]^{1/2}} \quad (22)$$

If Layer 1 is air, then $\gamma_1 = j\omega\sqrt{\mu_1\epsilon_1}$ and if Layer 2 is a material with both dielectric and electrical conductivity properties:

$$\begin{aligned} \gamma_2 &= \frac{\sigma_2}{2} \sqrt{\frac{\mu_2}{\epsilon_2}} + j\omega\sqrt{\mu_2\epsilon_2} \\ \frac{\gamma_1}{\gamma_2} &= \frac{j\omega\sqrt{\mu_1\epsilon_1}}{\frac{\sigma_2}{2} \sqrt{\frac{\mu_2}{\epsilon_2}} + j\omega\sqrt{\mu_2\epsilon_2}} \end{aligned}$$

$$\left(\frac{\gamma_1}{\gamma_2}\right)^2 = \frac{-\omega^2 \mu_1 \epsilon_1}{\frac{\sigma_2^2 \mu_2}{4\epsilon_2} - \omega^2 \mu_2 \epsilon_2 + j\omega \mu_2 \epsilon_2} \quad (23)$$

From Equation 22 and 23, the reflection coefficient is:

$$\Gamma_{\perp}^b = \frac{\cos \theta_i - \sqrt{\frac{\epsilon_2}{\epsilon_1}} \left\{ 1 - \left[\frac{\epsilon_1 / \epsilon_2}{1 - \left(\frac{\sigma_2}{2\omega \epsilon_2} \right)^2 - j \left(\frac{\sigma_2}{\omega \epsilon_2} \right)} \right] \sin^2 \theta_i \right\}^{1/2}}{\cos \theta_i + \sqrt{\frac{\epsilon_2}{\epsilon_1}} \left\{ 1 - \left[\frac{\epsilon_1 / \epsilon_2}{1 - \left(\frac{\sigma_2}{2\omega \epsilon_2} \right)^2 - j \left(\frac{\sigma_2}{\omega \epsilon_2} \right)} \right] \sin^2 \theta_i \right\}^{1/2}} \quad (24)$$

The real part of the reflection coefficient is:

$$\text{Re}[\Gamma_{\perp}^b] = \rho_{12} = \left\{ \left(\frac{\epsilon_1}{\epsilon_2} \right) \left[\cos^2 \theta_i \left(\frac{1 - \rho_{12}}{1 + \rho_{12}} \right)^2 \right] - 1 \right\} \frac{1}{\left[-\frac{\epsilon_1}{\epsilon_2} \sin^2 \theta_i \right]} = \frac{1}{\left[1 - \left(\frac{\sigma_2}{2\omega \epsilon_2} \right)^2 \right] - j \left(\frac{\sigma_2}{\omega \epsilon_2} \right)} \quad (25)$$

The ratio of the two dielectric constants is related to the reflection coefficient as follows:

$$\left(\frac{1 - \rho_{12}}{1 + \rho_{12}} \right)^2 = \frac{\epsilon_2}{\epsilon_1} \quad (26)$$

The general equation becomes:

$$r = \frac{n^4}{2b} \left[b + \frac{1 - 2b}{n^2} \right] \left\{ -1 \pm \left[1 - \frac{4(b-1)}{\frac{n^4}{b} \left(b + \frac{1 - 2b}{n^2} \right)^2} \right]^{1/2} \right\} \quad (27)$$

where $r = \left(\frac{\sigma_2}{\omega \epsilon_2} \right)^2$

$$b = \frac{\epsilon_2}{\epsilon_1}$$

n = calibration factor

Using $r = \left(\frac{\sigma_2}{\omega \epsilon_2} \right)^2$ in Equation 27, the result is in Equation 28.

$$\sigma_2 = \omega \epsilon_2 \left\{ \left[n^4 \left(\frac{2b-1}{2b} \right) - \frac{1}{2} \right] \left\{ 1 \pm \left[1 - \frac{4(b-1)}{b \left(n^2 + \frac{1-2b}{b} \right)^2} \right]^{1/2} \right\} \right\}^{1/2} \quad (28)$$

CONCLUSIONS

Results from Phase II of this research project exploring the further development and utility of mechanics-based models for base courses support the following conclusions:

- The self-consistent model, PaveSCM, shows good promise for estimating density and moisture content.
- Results estimating modulus with LayerMAPP at a controlled test site tracked reasonably with the FWD with an average error of about 14 ksi or less.
- Results estimating modulus did not match well with a base containing a very low percent of non-plastic fines, suggesting an alternate model is needed for these special cases.
- Data suggest that in new pavements the modulus measured with the FWD is more variable than the modulus predicted from the mechanics-based approach.
- Data suggest that better agreement exists between the mechanics-based models and the FWD when evaluating pavements that have an existing surface.
- The LayerMAPP tool can be used on unsurfaced base course. If a surfacing exists, the surface thickness should be at least $\frac{3}{4}$ in.
- Exploratory work and theoretical derivations suggest GPR may be able to simultaneously estimate both dielectric constant and electrical conductivity from the surface reflection, thus allowing estimation of stabilizer content.

CHAPTER 2. COMPACTION MONITORING FOR QUALITY CONTROL DURING ASPHALT MIXTURE CONSTRUCTION

BACKGROUND

Attaining uniform construction of the required specification quality serves to maximize pavement life and minimize life-cycle costs. Often, localized defects govern pavement life. The compaction monitoring system (CMS) installs onto the breakdown roller during asphalt mixture construction with the intent of validating that proper compaction passes were applied and, if feasible through the CMS model, provides an estimator of compacted mat density. The premise of the CMS is to use a compaction index (CI) concept, where the CI is weighted according to the compaction efficiency across the roller drum's width and the number of passes of the roller.

Phase I of this project, documented separately, showed the CMS a potentially viable process-control tool, but documented further steps were needed in development of the technology. Improvements needed included integration of the system to a more field-friendly form factor, further evaluation of the CMS density prediction model, and further deployment and validation of suitable applications of the CMS. This chapter presents Phase II work addressing those topics.

PROCEDURES

Form Factor Development

Researchers performed continuous development of a revised form factor using a programmable logic controller (PLC) and human-machine interface (HMI). Goals included developing a platform that was:

- Relatively inexpensive, ideally less than \$5,000.
- Rugged.
- Portable.
- Lightweight.
- Rapid and easy to install and remove.

Deployment of CMS on Test Sites

Researchers deployed the CMS on multiple construction projects throughout Phase II. First, the team planned and oversaw the construction of a test site at Texas A&M's RELIS campus. This test site included Type D and TOM-F mixes, and two different levels of pavement foundational support. The first track comprised two 12-ft lanes of flexible pavement with a total centerline distance of approximately 1,300 ft. Four categories of materials were used to construct the flexible pavement:

- Lime treated subgrade.
- Flexible base.
- Hot mix asphalt (Type-D).
- Thin overlay mix (TOM-F).

The other track comprised a 12-ft Type-D/TOM-F overlay on an existing Portland cement concrete pavement (rigid pavement) approximately 1,000 ft long. A local contractor constructed the test sections, and researchers managed, inspected, and performed extensive testing during construction. Figure 16 presents the test layout. Appendix A presents details of the test plan.

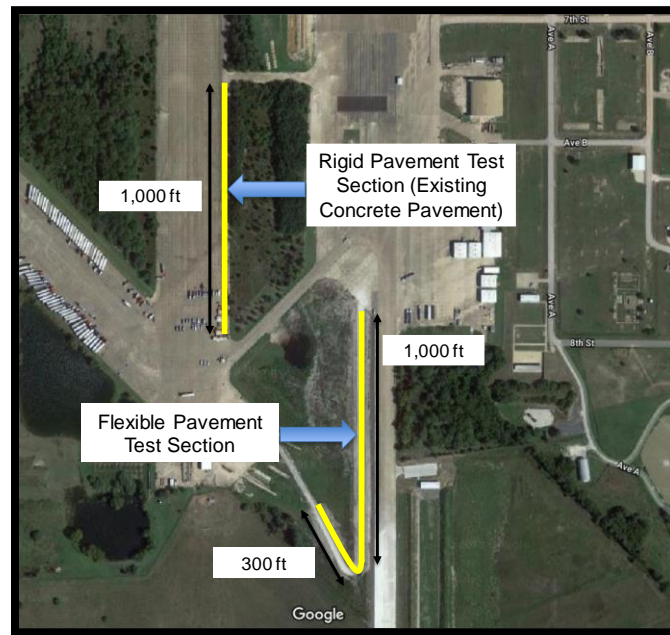


Figure 16. Layout of RELLIS Test Site.

Next, the team deployed the CMS on four construction projects and evaluated the utility of the CMS in actual production environments. These construction projects also served as proving grounds for evaluating refinements of the CMS density prediction model.

For collection of CMS data in all deployments, researchers installed the CMS onto the compaction roller, mounted a GPS unit on the top of the roller to track the roller's location, and installed an accelerometer to measure roller vibration. Infrared temperature sensors installed to the sides of the roller measured the temperature of the mat surface. Upon field evaluation of data, researchers selected core locations, determined precisely the GPS coordinate for each core location, collected nuclear density readings over each core location, and then cut and collected pavement cores. The laboratory then determined the density and air void content of each core.

Density Prediction Model Development

Prior work with the CMS did not account for whether the roller was vibrating or not, and also prior work did not employ the temperature of the mix at time of rolling in the CMS model.

Researchers performed lab compaction curves with asphalt mixtures at different temperatures to evaluate temperature factors in the CMS density prediction model. Researchers evaluated various potential updates to the CMS model using actual field construction project data to analyze whether the model updates improved the ability of the CMS to relate to asphalt mixture density.

Researchers also used finite element analysis to evaluate drum CI weighting factors and the distribution of those weighting factors across the width of the roller drum. Finally, researchers explored use of a lab compaction index approach to help define the required field compaction

index. Researchers performed these density model development activities in parallel with deployment procedures and evaluated model updates as they developed and obtained test data.

RESULTS

Form Factor Development

Researchers identified, procured, and system-integrated a suitable PLC/HMI system from Automation Direct. The Productivity 2000 platform was originally used for the PLC, which was changed later to a smaller footprint BRX platform. Figure 17 shows the PLC system, and Figure 18 illustrates the HMI interface.

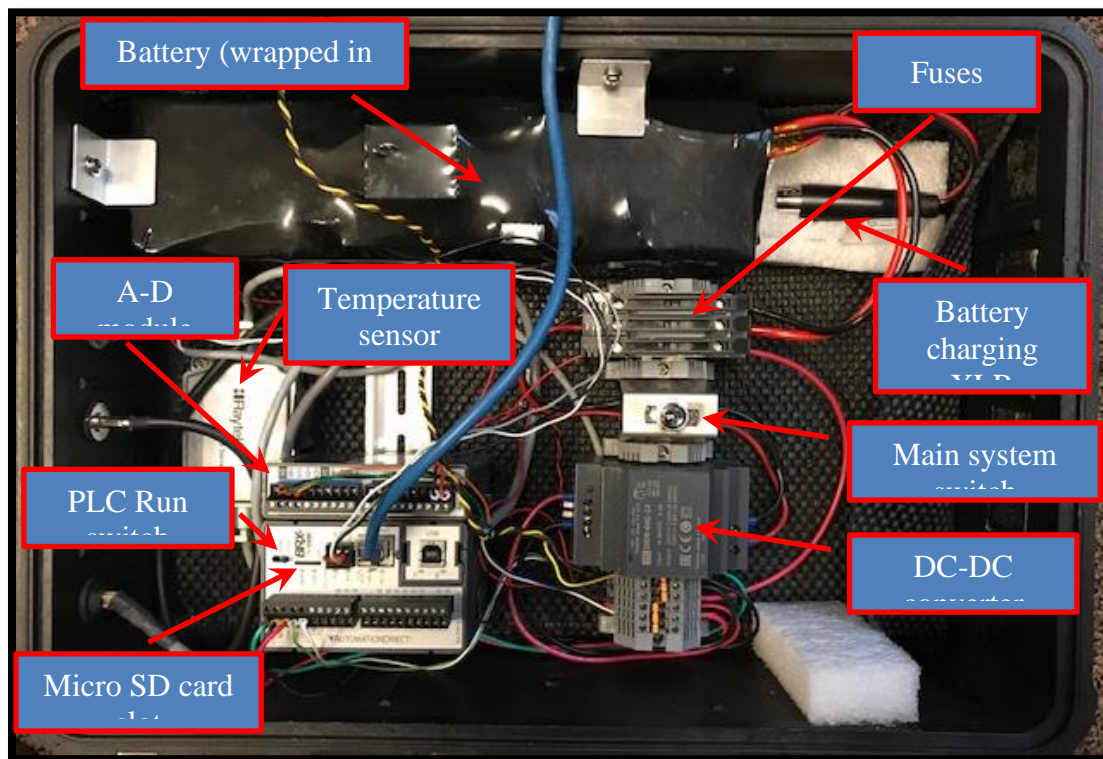


Figure 17. PLC System for Compaction Monitoring System.

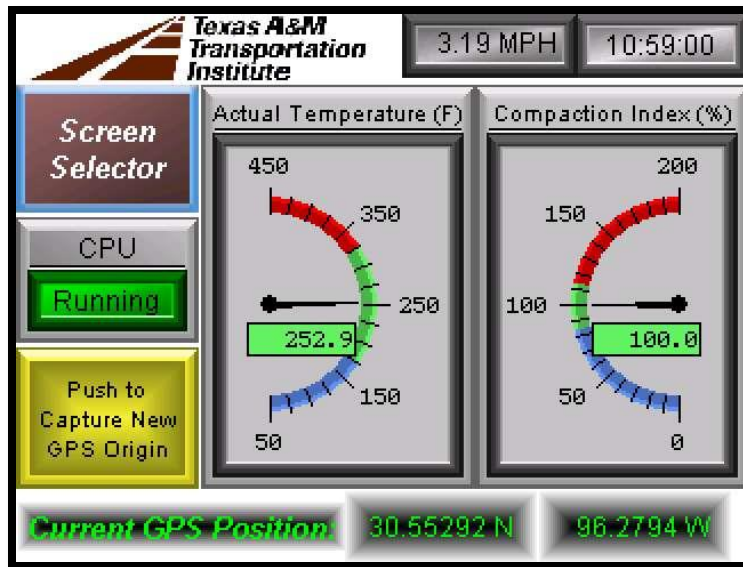


Figure 18. HMI Display for CMS.

Both components of the PLC system were housed in a Pelican case for protection in the field. A lithium battery was used because of the reduced weight compared to lead acid. In some cases, it may be possible to use power from the compactor, but some compactor's power supplies are incompatible with the CMS. Therefore, the use of a dedicated CMS system battery is recommended.

The PLC system did not include real time kinematic (RTK) corrections due to lack of a suitable cellular system. The PLC system was changed from the Trimble system to a wide area augmentation system (WAAS)-enabled Garmin GPS. The coordinates using RTK versus WAAS were found to be within approximately $\pm 0.000025^\circ$ of each other or better as Figure 19 illustrates.

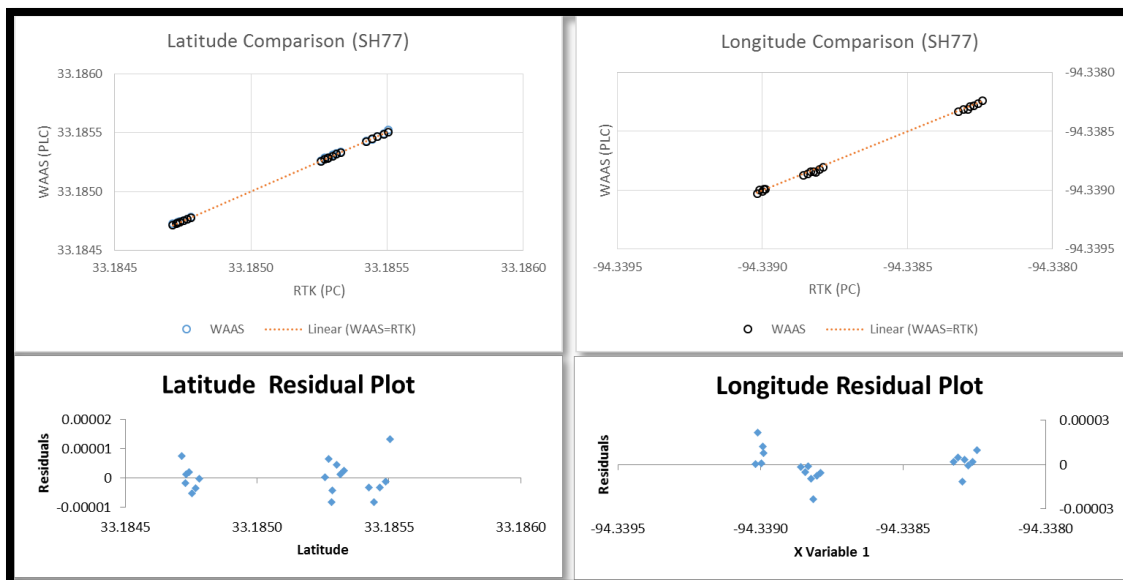


Figure 19. RTK vs. WAAS Coordinates.

Given all the sources of variability associated with hot mix construction, it does not seem to be necessary to have RTK if WAAS is available. However, to implement future cloud-based storage,

local machine to machine communication, and monitoring of the HMI with a cell phone from a remote location, a suitable cellular system with a data plan must be implemented and connected to the PLC, which may have the added benefit of providing access to RTK if desired. A device such as the Digi Transport model WR31-L52A-DE1-TB with a suitable data plan SIM card would be required. This unit provides for both wireless and wired communication and includes Ethernet LAN connectors that could be used with the PLC systems.

RELLIS Test Site Results

Two CMS systems were used on the RELLIS test site. One used a Windows laptop PC system while the other used a PLC system with an HMI. Both systems acquired similar data, but there were some differences between the systems. Most notably:

- The Windows-based system used essentially the same GPS hardware, but the type of message used to get speed and direction information directly from the satellite was different from the PLC.
- The HMI has much less capable graphics than the laptop, but it is adequate for the task.
- The PLC system recorded acceleration in three orthogonal directions. The laptop recorded vertical acceleration and performed Fast Fourier Transform analysis on the data.
- The Windows system used RTK position corrections through the use of a cellular Wi-fi hot spot. While the PLC might be able to use RTK in the future through a hard wired Ethernet port to a cellular device, it was not attempted on this project.

Figure 20 illustrates CMS testing. Appendix B presents a summary of daily construction and test phasing. Appendix C presents a summary of the construction activities.

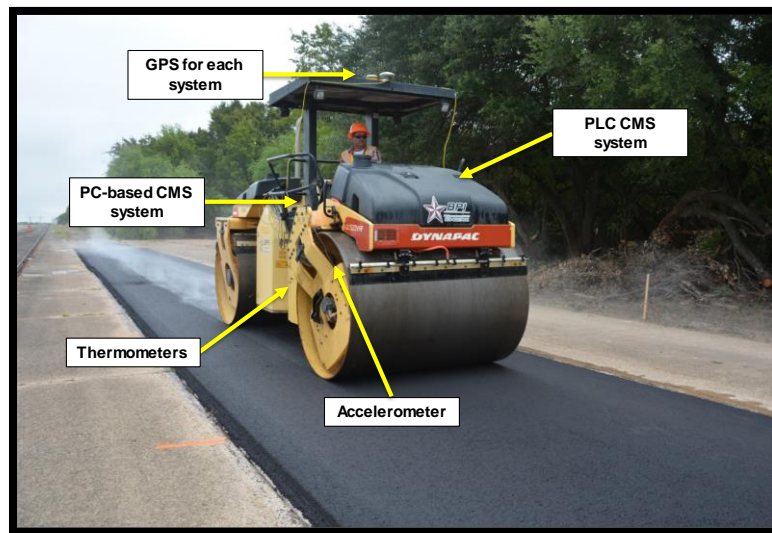


Figure 20. CMS Testing at RELLIS Test Site.

CI Calculation

The method for computing the compaction index with the PLC data was:

$$CI = \sum(WFD * WFT * WFg) \quad (29)$$

Where

WFD = weighting factor for drum position

WFT = weighting factor for temperature

WFg = weighting factor vibration

In this compaction index model, WFD becomes zero if the point of interest is not within the width of the drum (i.e., the roller does not roll over the point), and the weighting factor for temperature (WFT) becomes zero if the asphalt mat is below the cessation temperature. The weighting factor for vibration (WFg) is never zero, or even less than 1.0 in this model, but that concept of WFg deserves further evaluation.

Drum Weighting Factor

At the RELLIS test site, a 6.4-ft drum was used, and researchers assumed that the drop in compaction efficiency would occur at 28.571 percent of the width of the drum (from the edge of the drum) according to the data shown in Figure 21. The efficiency weighting factor remains at 1.0 in the center part of the drum.

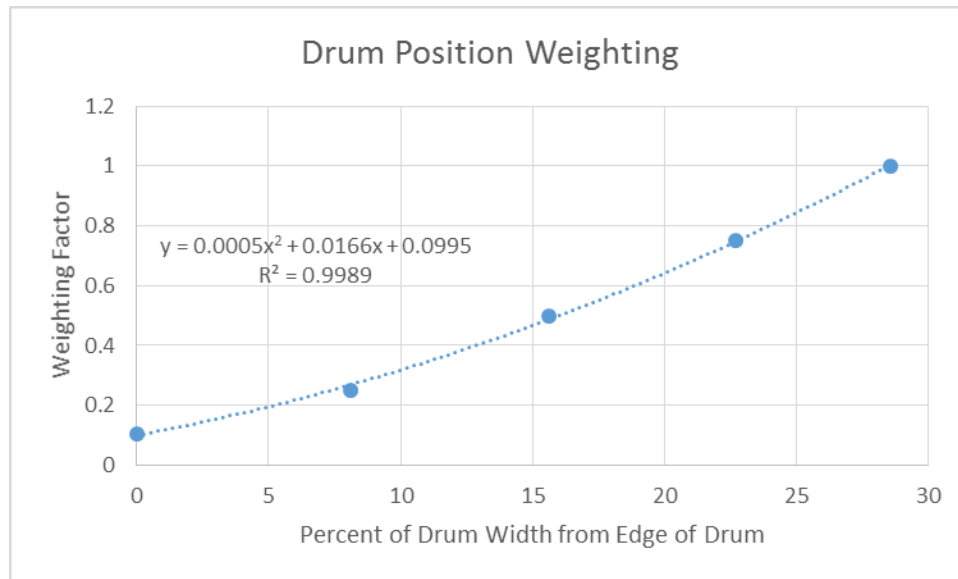


Figure 21. Weighting Factor for Drum Position.

Temperature Weighting Factor

WFT should preferably be based on the asphalt binder rheology. In the absence of direct measurements, the following assumptions were made:

- For the Type-D mix, a maximum temperature of 325°F, a cessation temperature of 175°F–200°F, and a descriptive equation of the form $WFT_{Type\ D} = T^{0.305} - 4.83$ were used. The boundary temperatures were estimated from literature sources such as The Asphalt Institute, and are general numbers for asphalt. A better procedure would be to establish better estimates from measurements in the field or lab on the job mix formula (JMF). This approach does not handle the possibility of the weighting factor dropping off on the hot side of the maximum temperature due to adverse effects of tenderness.
- For the TOM-F mix, the same maximum temperature as the Type-D mix was used, a cessation temperature of 125°F, and an equation of the form $WFT_{TOM\ F} = T^{0.26} - 3.5$ were used.

Vibration Weighting Factor

WFg should preferably be based on testing with the JMF. At present, this factor was assumed to be the number of g's applied. When the vibration is turned off and the voltage coming from the accelerometer is zero, the acceleration is 1g and the weighting factor is 1.0 (note that this relationship between voltage and acceleration depends on the type of accelerometer used and its calibration). With the vibration turned on, the weighting factor will become whatever the accelerometer reads (e.g., 2g is a weighting of 2.0). At this time, it seems to be a reasonable assumption that a 2g acceleration is applying twice as much compaction effort to the mat. However, this assumption does not address the following considerations:

- A 2g impact is followed by an upward movement that makes the compactor go below 1g load applied to the mat (depending on the forward speed). Therefore, there is a little bit of poetic license involved in the assumption that 2g is twice as effective as static rolling everywhere.
- A 2g impact may actually reduce compaction efficiency; it may not always be a valid assumption that impact increases compaction efficiency. This is particularly so with thin TOM mixes that may begin to break down and experience increasing air voids and lower densities when vibration is used.
- For standard eccentric weight compactors that perform mostly up and down impacts, a single axis accelerometer is adequate to measure the response. However, a 3-axis accelerometer was selected for the PLC because it may become important if the contractor uses one of the newer oscillatory compactors because it may be important to know which direction the load vector is pointed.

Type-D Layer CMS Results

Figure 22 and Figure 23 illustrate the CMS mapping of compaction index, number of roller passes, and temperature for the Type-D mix placement on the flexible and rigid pavement sections, respectively.

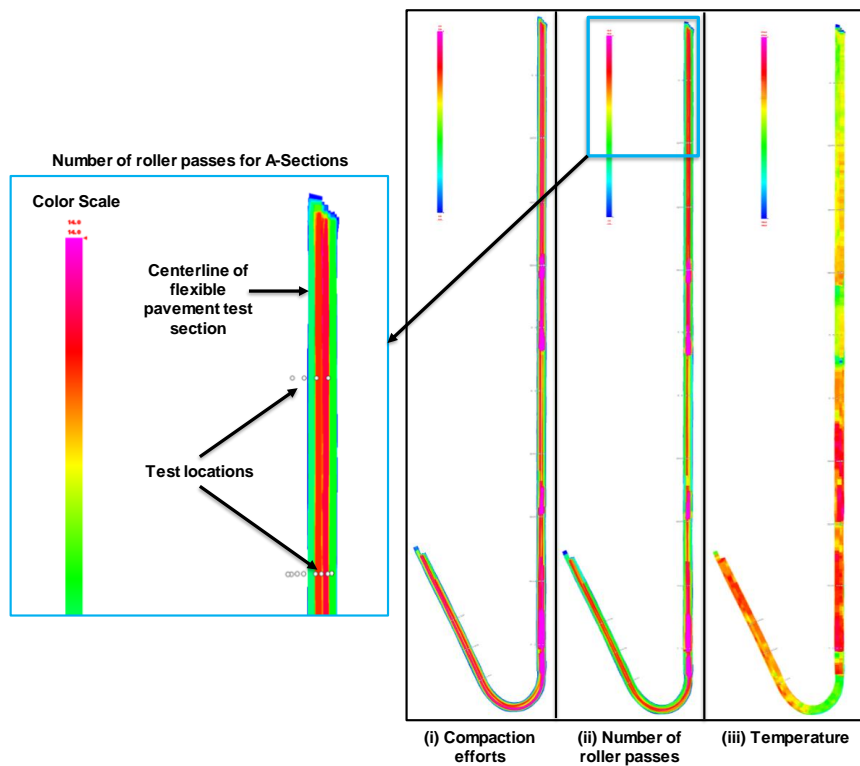


Figure 22. CMS Mapping of Roller Operations on Type-D Mix at Flexible Site.

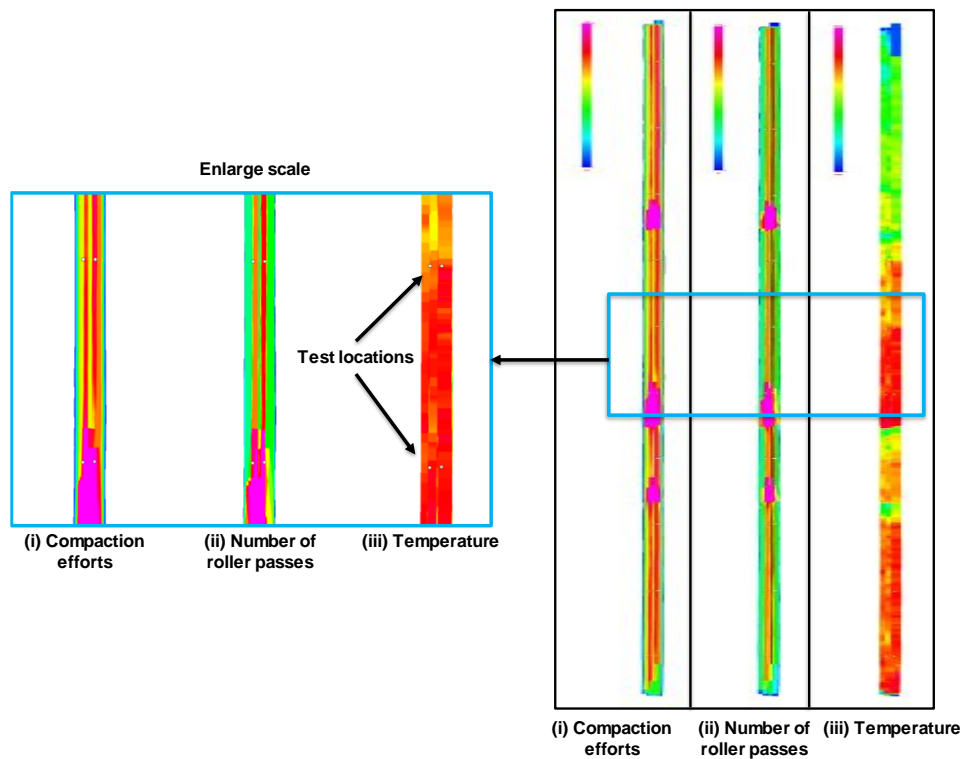


Figure 23. CMS Mapping of Roller Operations on Type-D Mix at Rigid Site.

Analysis of PLC CI for Type D Mixes

Figure 24 and Table 3 present the statistical results for CI using the PLC system on the D mix. All *F*-ratios are based on the residual mean square error. The analysis included 43 complete cases. The results show:

- The mean density was equivalent between section 3B and section 5.
- Since the two *P*-values were less than 0.05, both compaction index and section had a statistically significant effect on the core air voids at the 95 percent confidence level.

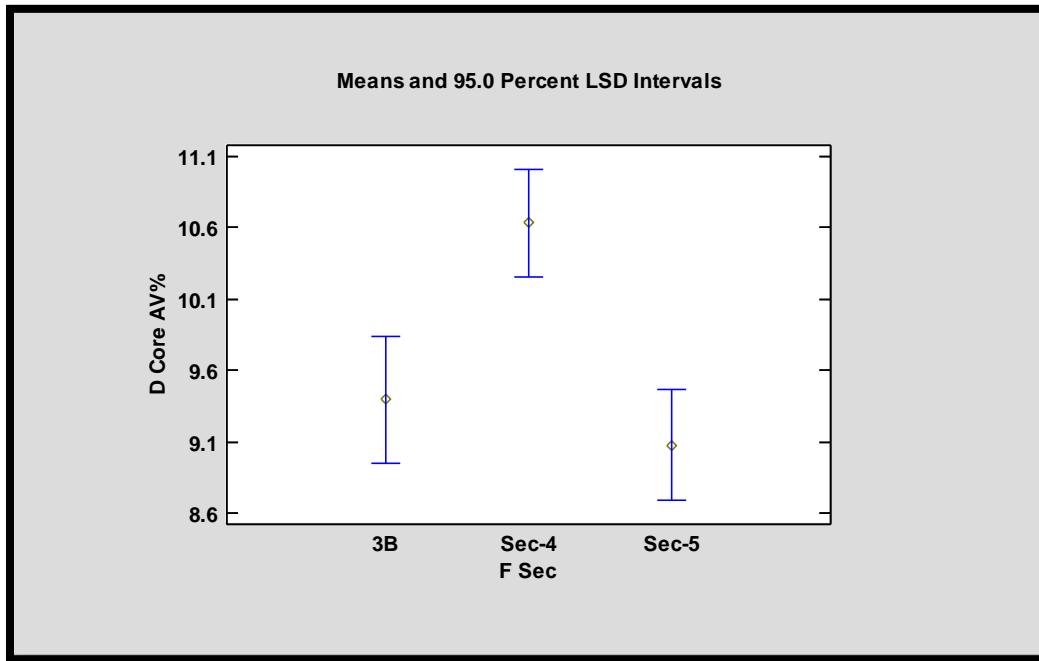


Figure 24. Means Plot – D Mix, Sections Tested with PLC System.

Table 3. Analysis of Variance for D Mix Core Air Voids from PLC System.

<i>Source</i>	<i>Sum of Squares</i>	<i>Df</i>	<i>Mean Square</i>	<i>F-Ratio</i>	<i>P-Value</i>
COVARIATES					
D PLC CI	11.402	1	11.402	11.09	0.0019
MAIN EFFECTS					
A:F Sec	18.1368	2	9.06839	8.82	0.0007
RESIDUAL	40.102	39	1.02826		
TOTAL (CORRECTED)	62.3559	42			

Analysis of PC CI for Type D Mixes

Figure 25, Table 4, and Table 5 present the statistical results for CI using the PC system on the D mix. Due to a power issue and a water spray bar leak on the front drum spray bar hitting the temperature sensor, only three sections of data were available with the PLC system on the Type-D layer, so the analysis for the PC system includes more data. The analysis with data from the PC system included 118 observations. The results show:

- The mean density was equivalent between section 1A, 1B, and 2A.
- The mean density was equivalent between sections 2B, 3A, 3B, and 5.
- The mean density in section 4 was different than any of the other sections.
- Both compaction index and section factors had a statistically significant effect on the core air voids at the 95 percent confidence level.

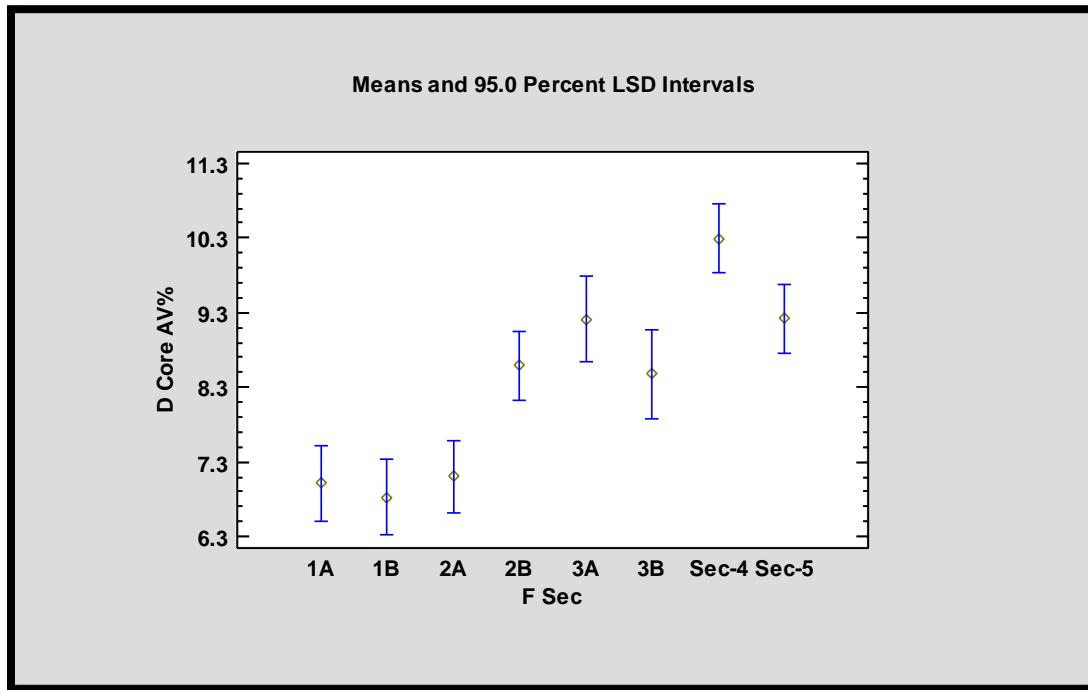


Figure 25. Means Plot – D Mix, Sections Tested with PC System.

Table 4. Analysis of Variance, D Mix Air Voids, Tested with PC System.

<i>Source</i>	<i>Sum of Squares</i>	<i>Df</i>	<i>Mean Square</i>	<i>F-Ratio</i>	<i>P-Value</i>
Model	300.73	8	37.5913	21.65	0.0000
Residual	189.273	109	1.73645		
Total (Corr.)	490.004	117			

Table 5. Type III Sums of Squares, D Mix Air Voids, Tested with PC System.

<i>Source</i>	<i>Sum of Squares</i>	<i>Df</i>	<i>Mean Square</i>	<i>F-Ratio</i>	<i>P-Value</i>
F Sec	170.013	7	24.2875	13.99	0.0000
D PC CI	55.9006	1	55.9006	32.19	0.0000
Residual	189.273	109	1.73645		
Total (corrected)	490.004	117			

Details of this model follow:

$$\begin{aligned} \text{D Core AV\%} = & 10.6311 - 1.32836 * I1(1) - 1.5177 * I1(2) - 1.23862 * I1(3) + 0.246767 * I1(4) \\ & + 0.869563 * I1(5) + 0.137341 * I1(6) + 1.95239 * I1(7) - \\ & 0.414169 * \text{D PC CI} \end{aligned}$$

where

$I1(1)$ = 1 if F Sec=1A, -1 if F Sec=Sec-5, 0 otherwise
 $I1(2)$ = 1 if F Sec=1B, -1 if F Sec=Sec-5, 0 otherwise
 $I1(3)$ = 1 if F Sec=2A, -1 if F Sec=Sec-5, 0 otherwise
 $I1(4)$ = 1 if F Sec=2B, -1 if F Sec=Sec-5, 0 otherwise
 $I1(5)$ = 1 if F Sec=3A, -1 if F Sec=Sec-5, 0 otherwise
 $I1(6)$ = 1 if F Sec=3B, -1 if F Sec=Sec-5, 0 otherwise
 $I1(7)$ = 1 if F Sec=Sec-4, -1 if F Sec=Sec-5, 0 otherwise

R-Squared = 61.3731 percent
R-Squared (adjusted for d.f.) = 58.5381 percent
Standard Error of Est. = 1.31775
Mean absolute error = 0.910576
Durbin-Watson statistic = 1.34536 (P=0.0001)

Figure 26 shows the observed versus predicted core air voids from this model.

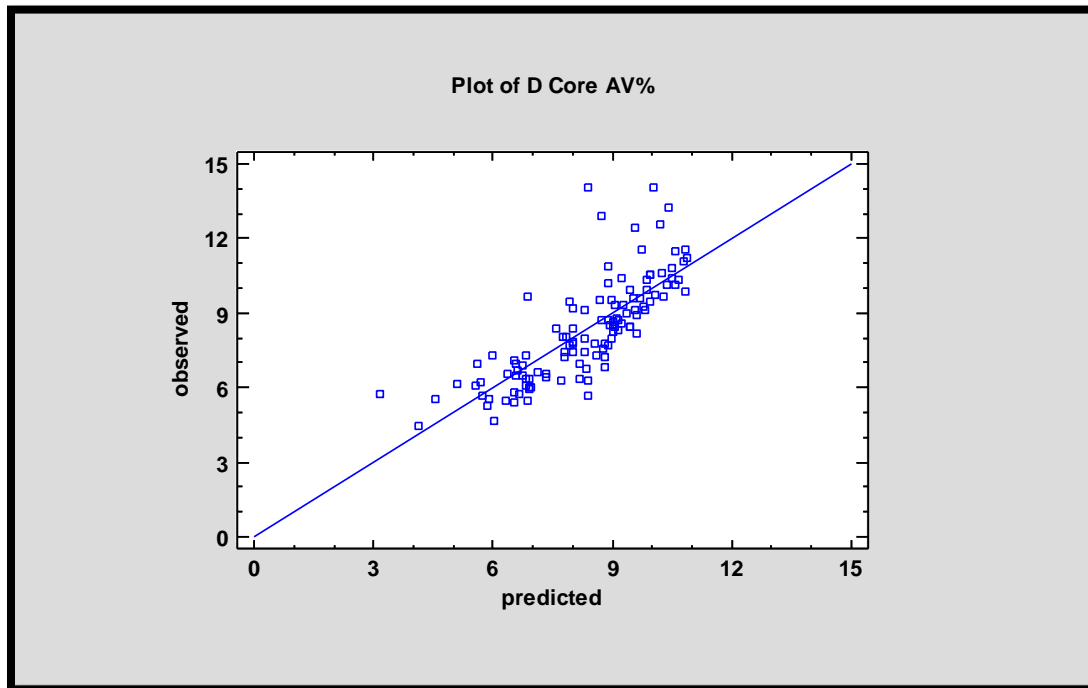


Figure 26. Observed versus Predicted Air Voids, D Mix, Tested with PC System.

TOM-F Layer CMS Results

Figure 27 shows the roller track for the TOM-F layer. Track areas that do not have RTK core positions superimposed are paths that the roller traveled going between the flexible and rigid pavement sites.

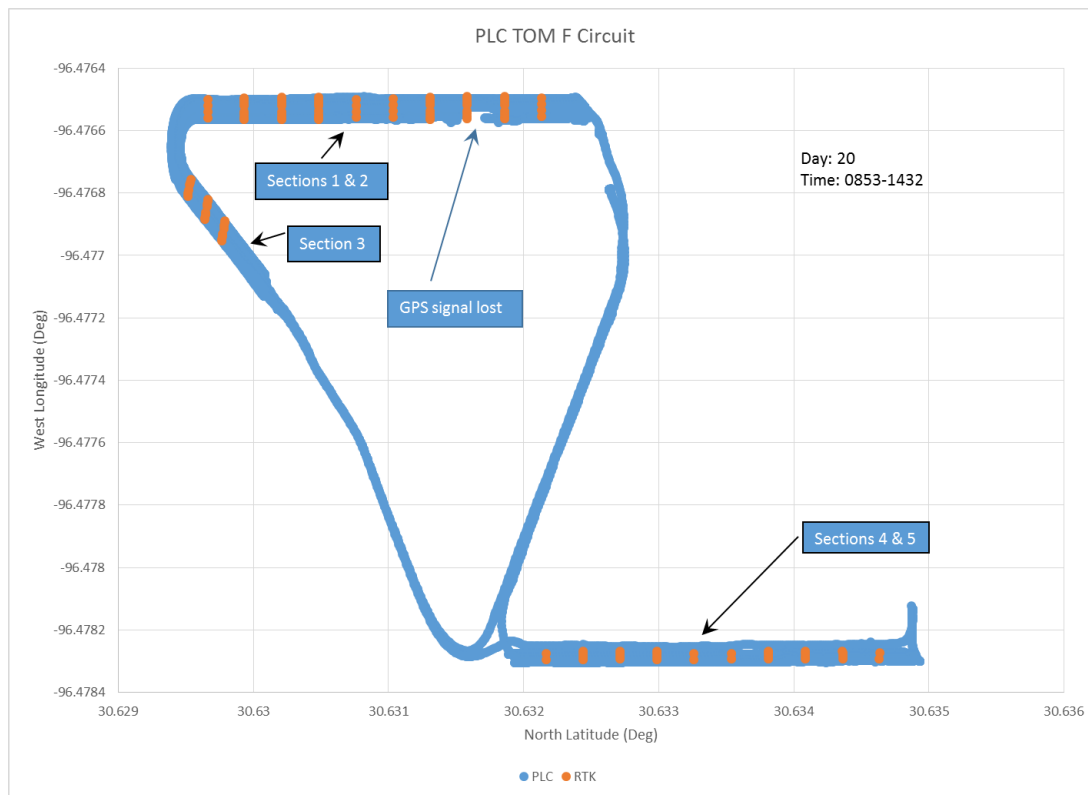


Figure 27. Track Data for TOM-F Compaction.

Analysis of PLC CI for TOM F Mixes

Figure 28 and Table 6 present which sections had equivalent air voids. In many cases, the mean air voids were equivalent across several different sections. The data include 118 observations.

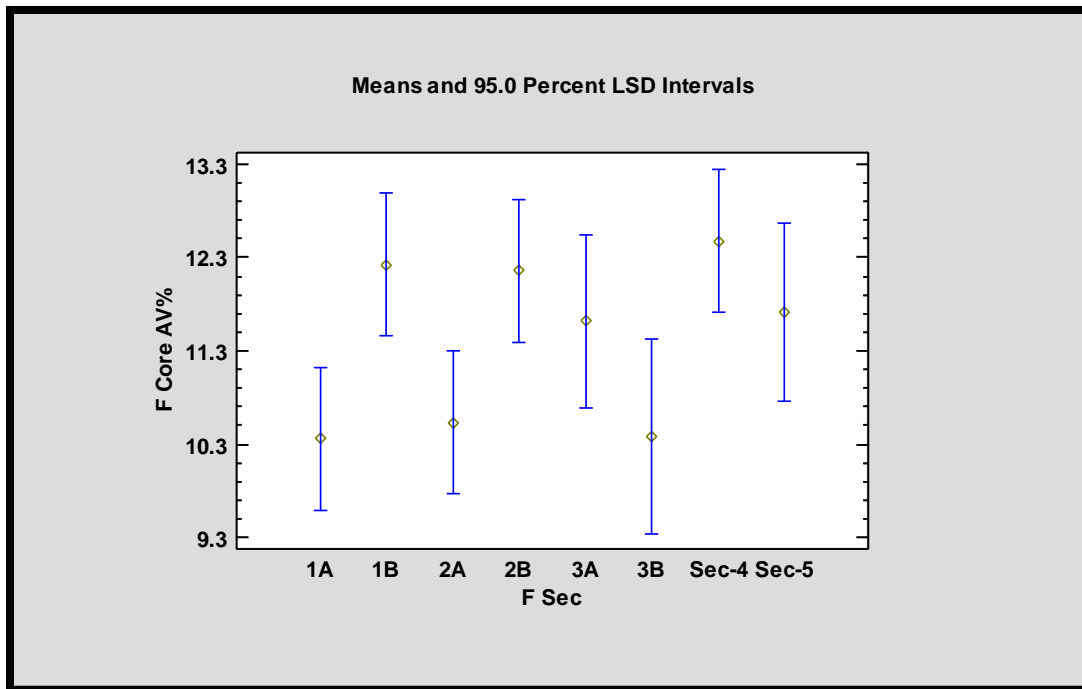


Figure 28. Means Plot – TOM-F, Sections Tested with PLC System.

Table 6. Multiple Comparisons for TOM-F Air Voids, Sections Tested with PLC System.

<i>F Sec</i>	<i>Count</i>	<i>LS Mean</i>	<i>LS Sigma</i>	<i>Homogeneous Groups</i>
1A	16	10.3569	0.546077	X
3B	11	10.3853	0.748951	XX
2A	16	10.5308	0.547015	X
3A	11	11.6152	0.655403	XXX
Sec-5	16	11.7208	0.680133	XXX
2B	16	12.1551	0.547892	XX
1B	16	12.2229	0.548681	XX
Sec-4	16	12.4715	0.545456	X

Table 7 and Table 8 present the statistical results from the PLC system on the TOM-F sections. The results show both section and CI were significant at the 95 percent confidence level.

Table 7. Analysis of Variance, TOM-F Air Voids, Tested with PLC System.

<i>Source</i>	<i>Sum of Squares</i>	<i>Df</i>	<i>Mean Square</i>	<i>F-Ratio</i>	<i>P-Value</i>
Model	188.842	8	23.6052	5.18	0.0000
Residual	496.713	109	4.557		
Total (Corr.)	685.554	117			

Table 8. Type III Sums of Squares, TOM-F Air Voids, Tested with PLC System.

<i>Source</i>	<i>Sum of Squares</i>	<i>Df</i>	<i>Mean Square</i>	<i>F-Ratio</i>	<i>P-Value</i>
F Sec	79.2652	7	11.3236	2.48	0.0209
F PLC CI	37.7333	1	37.7333	8.28	0.0048
Residual	496.713	109	4.557		
Total (corrected)	685.554	117			

Details of this model follow:

$$\text{F Core AV\%} = 11.8082 - 1.07542*I1(1) + 0.790626*I1(2) - 0.901521*I1(3) + 0.722778*I1(4) + 0.182888*I1(5) - 1.04697*I1(6) + 1.03916*I1(7) - 0.621805*F \text{ PLC CI}$$

where

$I1(1) = 1$ if F Sec=1A, -1 if F Sec=Sec-5, 0 otherwise
 $I1(2) = 1$ if F Sec=1B, -1 if F Sec=Sec-5, 0 otherwise
 $I1(3) = 1$ if F Sec=2A, -1 if F Sec=Sec-5, 0 otherwise
 $I1(4) = 1$ if F Sec=2B, -1 if F Sec=Sec-5, 0 otherwise
 $I1(5) = 1$ if F Sec=3A, -1 if F Sec=Sec-5, 0 otherwise
 $I1(6) = 1$ if F Sec=3B, -1 if F Sec=Sec-5, 0 otherwise
 $I1(7) = 1$ if F Sec=Sec-4, -1 if F Sec=Sec-5, 0 otherwise

R-Squared = 27.5458 percent
R-Squared (adjusted for d.f.) = 22.2281 percent
Standard Error of Est. = 2.13471
Mean absolute error = 1.66813
Durbin-Watson statistic = 1.94687 (P=0.3871)

Figure 29 shows the observed versus predicted core air voids from this model.

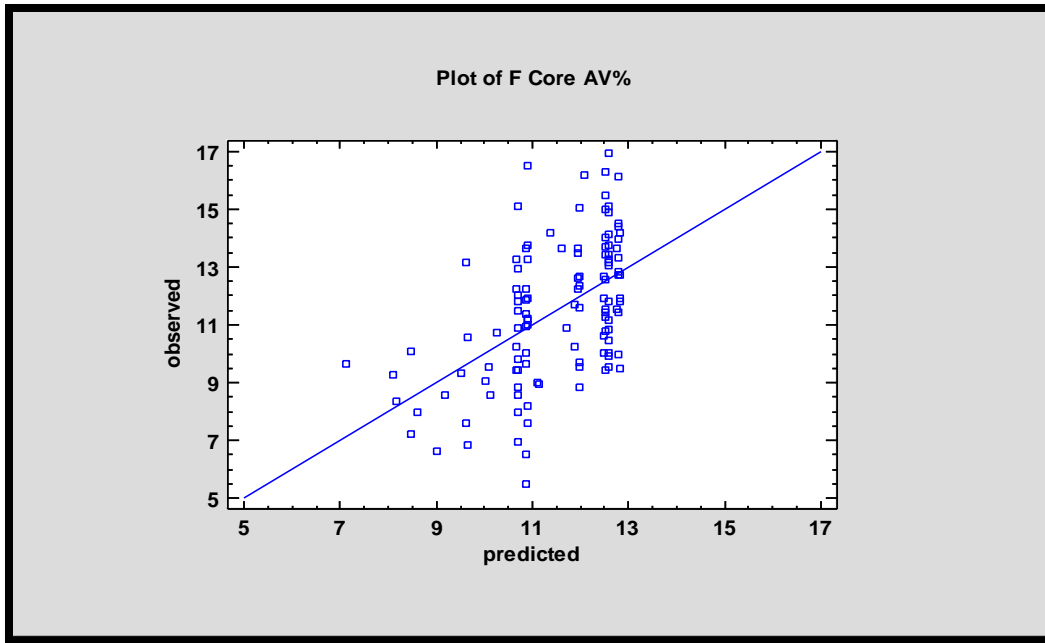


Figure 29. Observed versus Predicted Air Voids, TOM-F, Tested with PLC System.

Analysis of PC CI for TOM F Mixes

Figure 30 and Table 9 present which sections had equivalent air voids. In many cases, the mean air voids were equivalent across several different sections. The data include 118 observations.

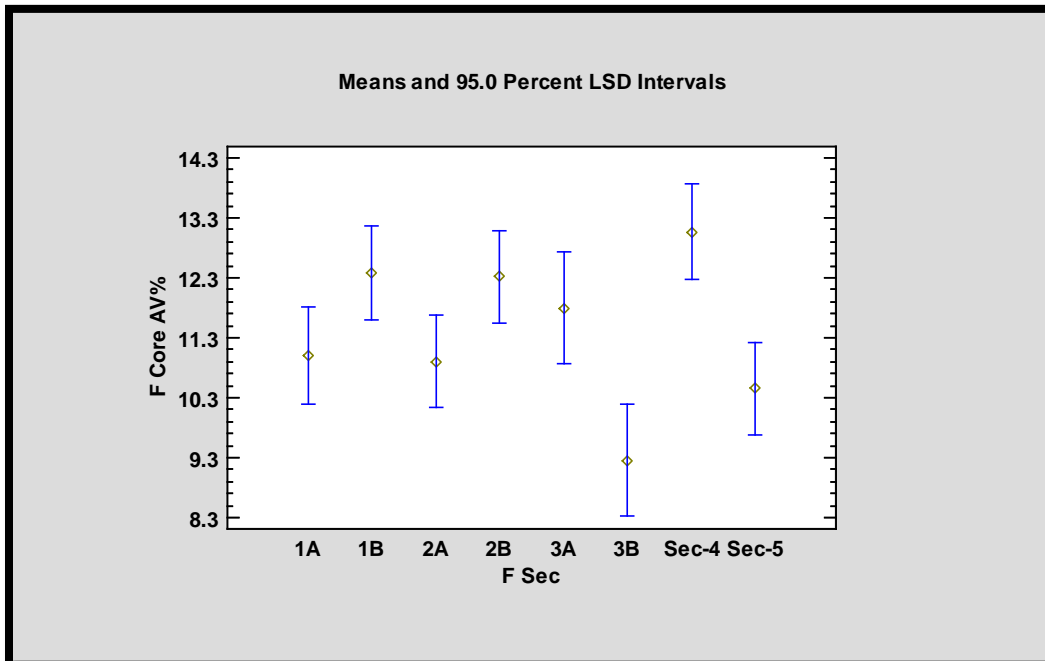


Figure 30. Means Plot, TOM-F, Sections Tested with PC System.

**Table 9. Multiple Comparisons TOM-F Air Voids,
Sections Tested with PC System.**

<i>F Sec</i>	<i>Count</i>	<i>LS Mean</i>	<i>LS Sigma</i>	<i>Homogeneous Groups</i>
3B	11	9.25827	0.658446	X
Sec-5	16	10.4555	0.546623	XX
2A	16	10.9063	0.546093	XXX
1A	16	11.0047	0.57422	XX
3A	11	11.7889	0.666314	XXX
2B	16	12.3146	0.557153	XX
1B	16	12.371	0.559699	XX
Sec-4	16	13.0614	0.566159	X

Table 10 and Table 11 present the statistical results from the PC system on the TOM-F sections. The results show the section was significant at the 95 percent confidence level, but CI was not. The results show CI was significant at the 90 percent confidence level.

Table 10. Analysis of Variance, TOM-F Air Voids, Tested with PC System.

<i>Source</i>	<i>Sum of Squares</i>	<i>Df</i>	<i>Mean Square</i>	<i>F-Ratio</i>	<i>P-Value</i>
Model	165.968	8	20.746	4.35	0.0001
Residual	519.586	109	4.76684		
Total (Corr.)	685.554	117			

Table 11. Type III Sums of Squares, TOM-F Air Voids, Tested with PC System.

<i>Source</i>	<i>Sum of Squares</i>	<i>Df</i>	<i>Mean Square</i>	<i>F-Ratio</i>	<i>P-Value</i>
F Sec	144.826	7	20.6894	4.34	0.0003
F PC CI	14.8599	1	14.8599	3.12	0.0803
Residual	519.586	109	4.76684		
Total (corrected)	685.554	117			

Details of this model follow, with Figure 31 presenting the observed versus predicted air voids.

$$\text{F Core AV\%} = 12.6331 - 0.390371 \cdot \text{I1}(1) + 0.975907 \cdot \text{I1}(2) - 0.48876 \cdot \text{I1}(3) + 0.919475 \cdot \text{I1}(4) + 0.393847 \cdot \text{I1}(5) - 2.13681 \cdot \text{I1}(6) + 1.66629 \cdot \text{I1}(7) - 0.346203 \cdot \text{F PC CI}$$

where

I1(1) = 1 if F Sec=1A, -1 if F Sec=Sec-5, 0 otherwise

I1(2) = 1 if F Sec=1B, -1 if F Sec=Sec-5, 0 otherwise

I1(3) = 1 if F Sec=2A, -1 if F Sec=Sec-5, 0 otherwise

I1(4) = 1 if F Sec=2B, -1 if F Sec=Sec-5, 0 otherwise

I1(5) = 1 if F Sec=3A, -1 if F Sec=Sec-5, 0 otherwise

I1(6) = 1 if F Sec=3B, -1 if F Sec=Sec-5, 0 otherwise

I1(7) = 1 if F Sec=Sec-4, -1 if F Sec=Sec-5, 0 otherwise

R-Squared = 24.2094 percent

R-Squared (adjusted for d.f.) = 18.6467 percent

Standard Error of Est. = 2.18331
Mean absolute error = 1.69624
Durbin-Watson statistic = 1.9338 (P=0.3604)

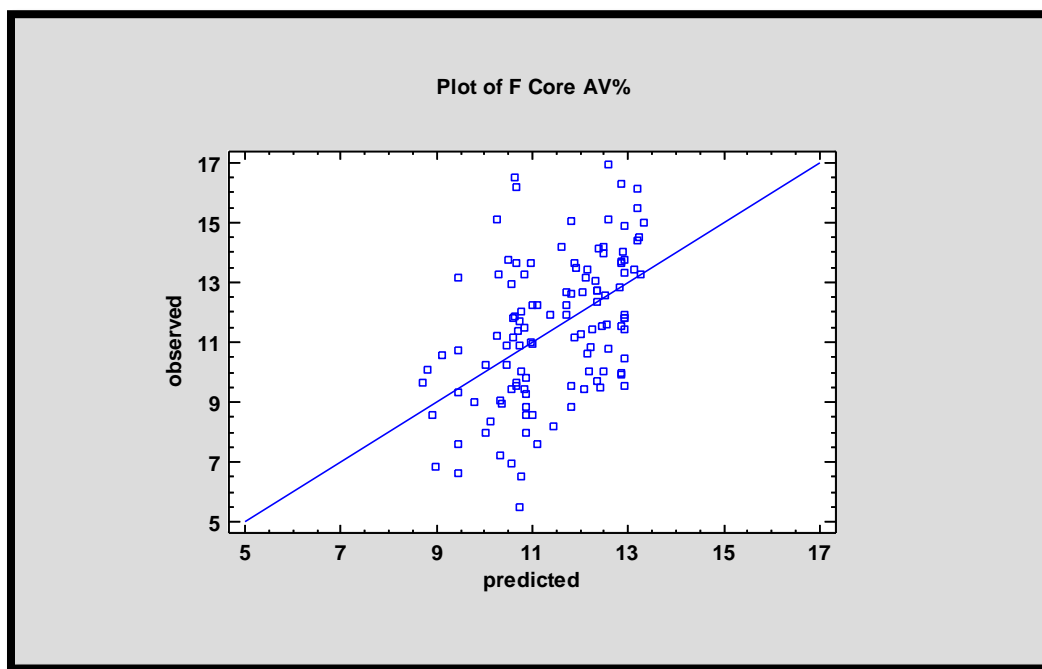


Figure 31. Observed versus Predicted Air Voids, TOM-F, Tested with PC System.

Construction Project Testing

SH 77

The Contractor placed a 2-inch SP-D mix containing 11 percent RAP and 3 percent RAS. A CAT CB66B breakdown roller (7 ft drum width, 11.3 ft wheel base) was used to compact the entire mat with a rolling pattern of three passes with vibration and three static passes. The mix temperature after laying down was approximately 260°F and monitored.

Researchers selected three different zones to collect cores and conduct density tests based on the mix temperature right before the first roller pass as follows:

- Zone-1: compaction temperature of 260°F.
- Zone-2: compaction temperature of 210°F.
- Zone-3: random locations.

Figure 32 shows the spot test locations for use in evaluating the ability of the CMS model to estimate density.

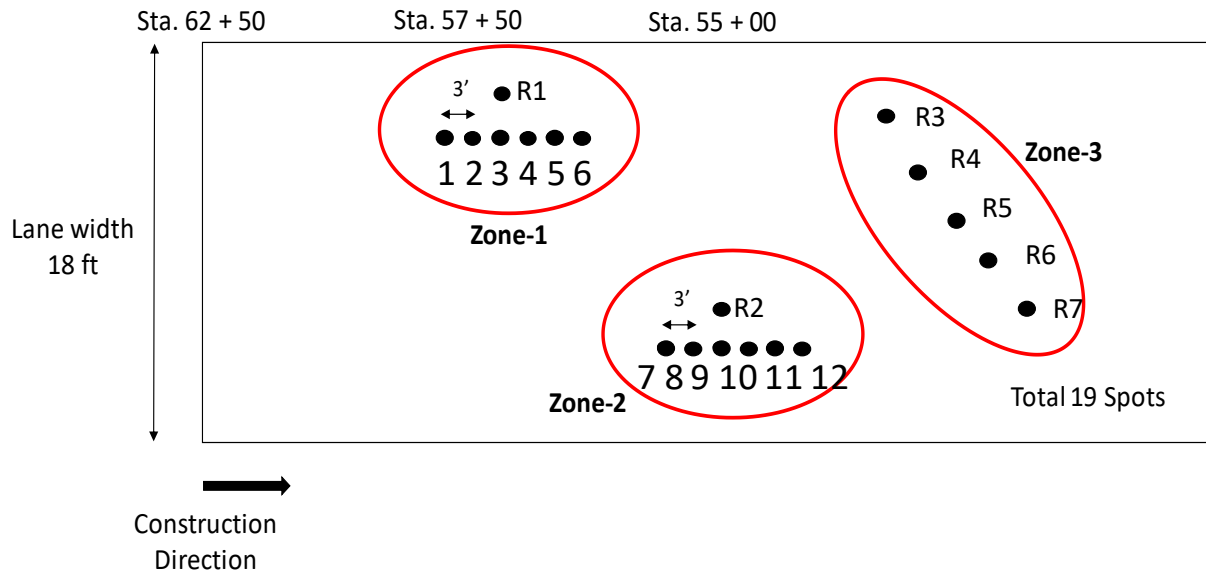


Figure 32. SH 77 Density and Core Locations.

IH 45

The Contractor placed a 2-inch SMA on top of the existing surface. A CAT CB64 breakdown roller (7 ft drum width, 11.3 ft wheel base) was used to compact the entire mat with a rolling pattern of three passes with vibration and two static passes. Figure 33 illustrates that 21 cores were collected over testing covering three days of production.

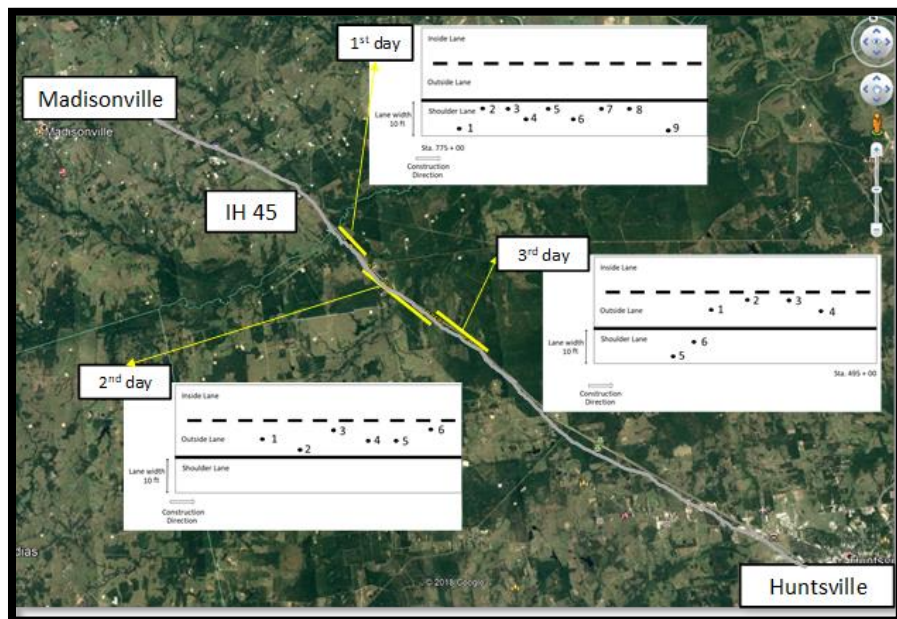


Figure 33. IH 45 Density and Core Locations.

FM 158

The Contractor placed a 2-inch SP-D mix after milling of the existing surface. A HAMM HD 140 breakdown roller (7 ft drum width, 11.3 ft wheel base) was used to compact the entire mat with a rolling pattern of two passes with vibration and one static pass. Figure 34 illustrates CMS testing underway, and preparation for spot testing three core locations.

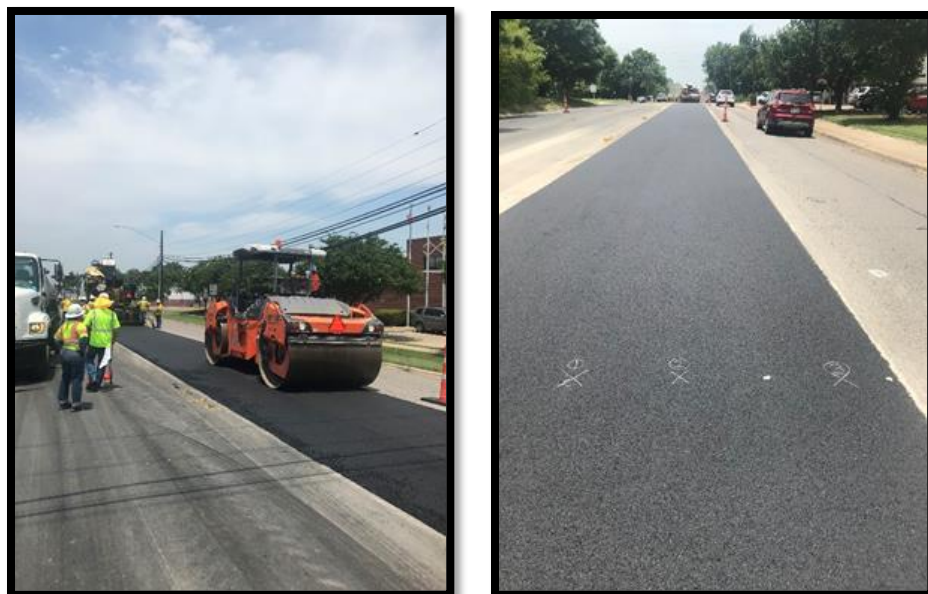


Figure 34. CMS Test Activities on FM 158.

Figure 35 illustrates that density tests were performed at a total of eight locations during two days, and the cutting of eight total cores was then performed at the testing locations.

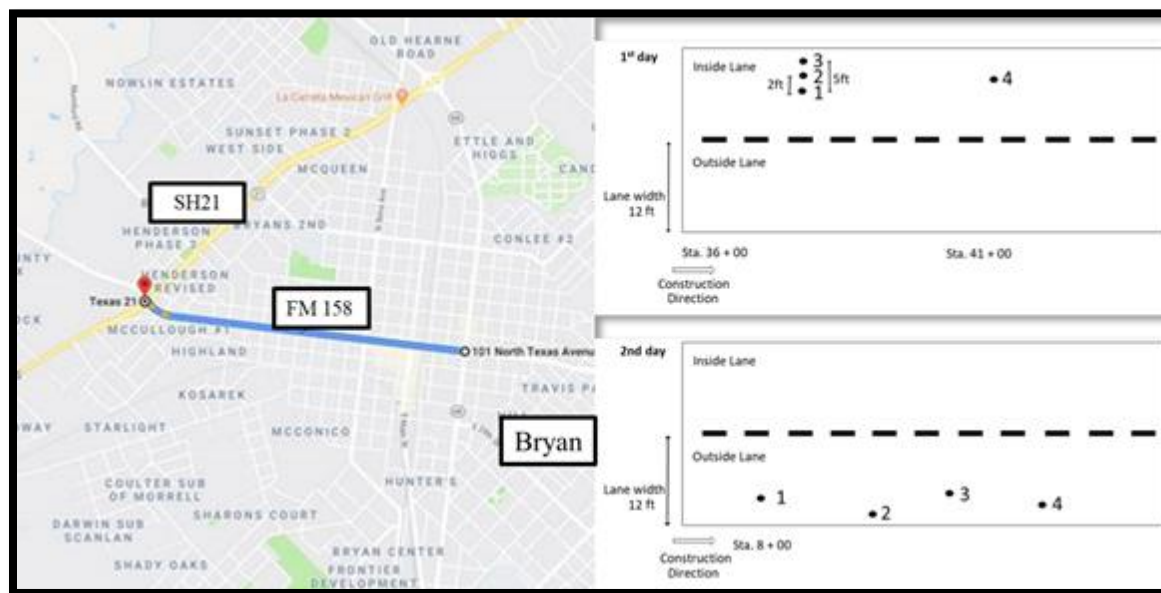


Figure 35. FM 158 Density and Core Locations.

SH 40

The Contractor placed a 3-inch SP-C on top of the existing surface. A HAMM HD 140 breakdown roller was used to compact the entire mat with a rolling pattern of three passes with vibration. After this breakdown roller, a pneumatic 5-tire roller applied two passes. Another roller conducted 2 passes with vibration on the entire lane around 30 minutes after the initial breakdown roller.

Figure 36 illustrates that density tests were performed at a total of eight locations during two days, and the cutting of eight total cores was then performed at the testing locations.

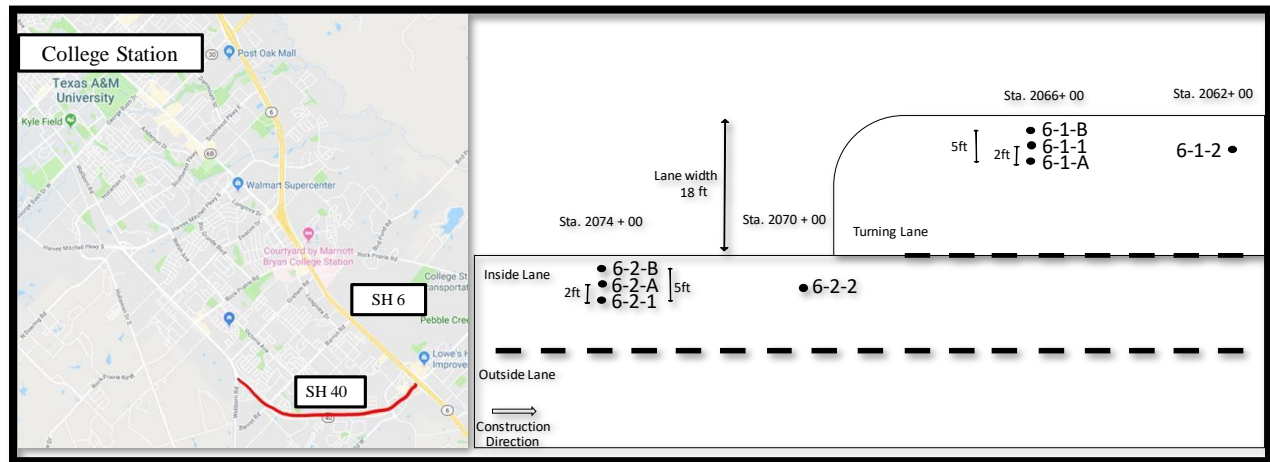


Figure 36. SH 40 Density and Core Locations.

OVERALL RESULTS FROM CONSTRUCTION PROJECT DEPLOYMENTS

Figure 37 presents a summary of CMS results from the cross section of all data collected. These data included:

- Type-D mix, RELLIS test site, on flexible foundation.
- Type-D mix, RELLIS test site, on rigid foundation.
- 2-inch SP-D, SH 77.
- 2-inch SMA, IH 45.
- 2-inch SP-D, FM 158.
- 3-inch SP-C, SH 40.

No data points were eliminated, although some statistical tests identified a few suspect data points, and no factor for job or mix type was included in the analysis.

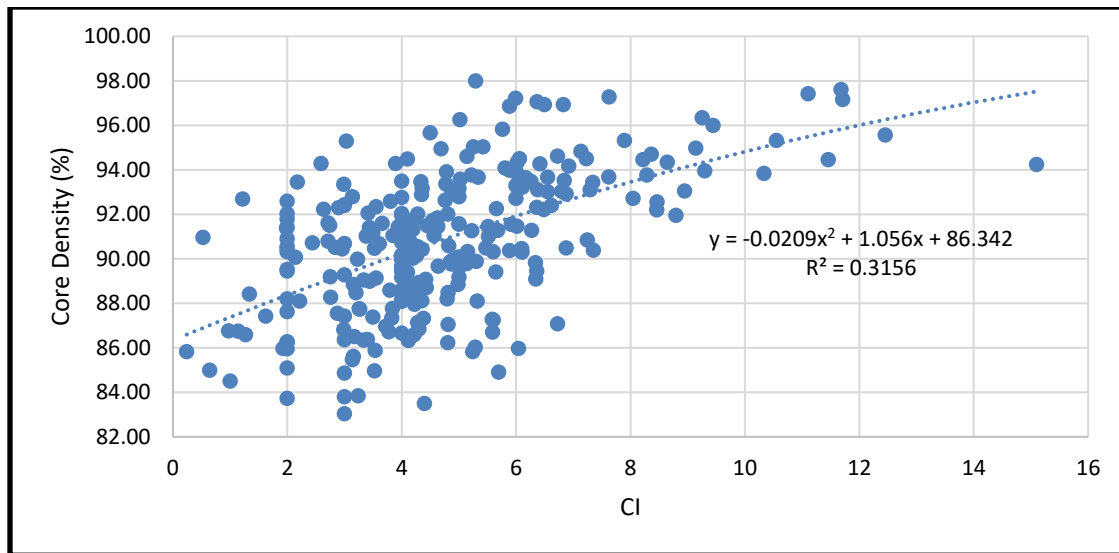


Figure 37. Core Density Results versus Compaction Index from All Projects.

DENSITY PREDICTION MODEL DEVELOPMENT

Throughout field deployments, researchers explored refinements to the CI model and also explored a lab compaction index for relation to the field. Researchers updated the drum factor and identified an approach to include a temperature factor. No suitable approach for modeling the vibration or foundational support factor was found with the available data; an approach for vibration was enabled based on whether the drum was vibrating or not. The version enabled for the PLC system is:

$$CI = CI + \left(\left(\frac{\text{Drum Factor}}{\text{Effective Compaction Effort}} \right) * \text{Temperature Factor} * \text{Vibration Factor} * 100 \right) \quad (30)$$

Appendix D presents details of developing these factors and exploration of the lab compaction index.

CONCLUSIONS

Results from Phase II of this project evaluating the use of the compaction monitoring system for process control during asphalt mixture paving show:

- The CMS can document if the prescribed rolling pattern has been applied.
- The CMS can record temperature at breakdown.
- The model to predict air voids from the compaction index can be expanded to include different drum weighting factors, a vibration factor, and a temperature factor.

- While these factors can be included, a generalized simple model may be sufficient, as the data suggest density estimates from the CMS regardless of model are not accurate for applications other than general process control information.
- The best potential use of the CMS is likely in process control to provide continuous feedback with far more testing coverage than routine use of a density gauge.

CHAPTER 3.

HIGH FREQUENCY GROUND-PENETRATING RADAR FOR DENSITY OF ASPHALT MIXTURE CONSTRUCTION

BACKGROUND

Attaining required density during asphalt mixture construction significantly influences the ability of the newly constructed layer to meet design expectations. Current random QC/QA testing only tests one location per subplot and results in significant risk to both Contractor and Owner/Agency. Often, localized defects govern pavement life.

High frequency GPR can provide near-continuous testing coverage of the uniformity and density of new asphalt layers. Additionally, in forensic applications, the question often arises of whether widespread density problems exist on a section. Phase I of this project demonstrated strong correlation between GPR measurements and actual reference value core densities. This chapter presents further refinements of the technology and recommends applications where GPR could provide substantial contribution to the state-of-the practice.

PROCEDURES

Researchers deployed the 3-channel, 2.5 GHz radar system shown in Figure 38 on multiple projects representing different mixture types and geographic regions. They integrated the original pushcart system into a vehicle. They used the GPR system to scan near full-coverage over evaluation sections, generally representing as a minimum line profiles of both wheel paths and either the mat centerline or the longitudinal joint.



Figure 38. GPR System for Measuring Density of Asphalt Mixture Construction.

To measure the mat density, researchers collected GPR readings over specific calibration core locations. They then collected the cores and measured their density and air voids in the lab to develop a calibration using the following:

$$Voids = ae^{bDiel} \quad (31)$$

where *Voids* = Core air void content, %.

Diel = Surface dielectric from the RDM.

a, b = Calibration coefficients.

Researchers included deployments of the GPR tool both in construction settings and forensic settings. Researchers also performed a laboratory sensitivity analysis of mixture variability. The sensitivity analysis addresses the question about whether a new calibration is required for slight changes in job mix formula during mixture production.

New Construction

Researchers identified construction projects throughout East, Central, and West Texas for field and laboratory evaluation. The projects represented a cross section of lift thicknesses, gradations, aggregate types, and asphalt contents as summarized in Table 12.

Table 12. Asphalt Mixture Summaries.

Project ID	Mix Type	Binder Type	Optimum AC (%)	Aggregate Type	Theo. Max SG	Thickness (in.)
SH 6-Valley Mills (WAC)	DG-D	64-22	5.2	Dolomite Gravel RAP	2.447	2.0 (approx.)
SH 6-Waco (WAC)	TOM-C	76-22 + Evotherm	6.6	Sandstone Dolomite	2.434	1.25
SH 30-College St. (BRY)	SMA-C	76-22	6.0	Sandstone Dolomite RAP	2.405	2.0
RELLIS Campus (BRY)	DG-D	64-22	5.0	Limestone	2.533	2.25
	TOM-F	76-22	7.2	Dolomite	2.515	0.9
SL 79-Del Rio (LRD)	DG-B	64-22	4.5	Gravel	2.451	3.5
SH 149-Beckville (ATL)	SP-C	76-22	5.3	Igneous	2.470	1.5
IH 45-Huntsville (BRY)	SMA-D	76-22	6.2	Limestone	2.392	2.0
FM 158-Bryan (BRY)	SP-D	64-22	5.2	Sandstone Limestone	2.446	2.0
US 59-Texarkana (ATL)	SMA-D	76-22	6.4	Gravel	2.362	2.0
SH 40-College St. (BRY)	SP-C	64-22	5.0	Sandstone Limestone	2.465	3.0

After performing calibrations, researchers continued to measure density on additional sublots, generally over two additional days (or nights as applicable) of paving. They used random core locations to validate the air void content as measured with GPR.

Forensic Investigations

Researchers performed forensic testing on two paving projects to assess if compaction concerns existed. Table 13 summarizes the mixtures from these projects.

Table 13. Asphalt Mixture Summary for Forensic Projects.

Project ID	Mix Type	Binder Type	Optimum AC (%)	Aggregate Type	Theo. Max SG	Thickness (in.)
US 287-Groveton	SP-C	64-22	4.8	Sandstone Limestone	2.504	2.0
SS 248-Tyler	DG-C	64-22	4.6	Sandstone Limestone	2.485	2.0

On US 287, researchers performed two passes of the vehicle in the southbound and northbound directions, resulting in six dielectric profiles spaced about 2-ft apart. To perform a calibration, spot-specific dielectric measurements were made at locations identified as having low, moderate, and high dielectric values in the southbound lane. A core was taken at each location and measured in the lab for air voids. Using the calibration, density maps were made for the entire project.

For SS 248, researchers collected dielectric profiles down the center and in the wheel paths of each lane. Calibration cores were taken from the westbound outside lane and in the center turn lane. Using the calibration, air voids maps and air void histogram distributions were made for the entire project. Areas with severe fatigue cracking, which resulted in excessively high air voids calculations (not indicative of the as-built pavement), were excluded from the analysis.

Figure 39 illustrates testing and the distress that was occurring on SS 248. Forensic applications could be a meaningful utilization of the GPR tool from this research.



Figure 39. Using GPR for Forensic Investigation.

Laboratory Sensitivity Analysis of Mixture Variability

To develop the laboratory test design, the actual production variation in seven completed projects was evaluated. The projects represent a range of mix types, and each project had a minimum of 10 production lots. A summary of the range in asphalt content, theoretical maximum specific gravity

(SG), and air voids is shown in Table 14. The laboratory test factors were then chosen to exceed these values.

Table 14. Production Summary and Expected Project Variance.

Project ID	Mix Type	AC (%)		Theo. Max SG		Air Voids (%)	
		Avg.	St. Dev.	Avg.	St. Dev.	Avg.	St. Dev.
US 385-Hartley	DG-C	5.00	0.205	2.45	0.007	6.13	1.07
FM 3083-Montgomery	DG-D	5.17	0.098	2.47	0.013	6.08	0.87
US 84-Freestone	SP-C	5.20	0.090	2.45	0.005	5.53	0.87
US 175-Kaufman	SP-D	5.38	0.136	2.47	0.008	6.75	0.91
IH 30-Tarrant	SMA-C	6.10	0.092	2.46	0.005	5.30	1.29
SH 171-Limestone	SMA-D	6.09	0.097	2.44	0.007	5.94	1.18
US 290-Travis	TOM-C	6.41	0.092	2.41	0.011	NA	NA
Overall		5.62	0.116	2.45	0.008	5.95	1.03
Expected range of property within a project (1.97*St Dev.)		±0.22		±0.016		±2.0	

The laboratory test design included five unique mixtures (Table 15). The test design varied the asphalt content, coarse aggregate, and air void content. While the change in aggregate type is not likely to occur on a given project, these data would be useful in exploring mechanistic-based calibration models. Table 16 shows an example test matrix from one mixture. The other mixtures varied in a similar manner except used their respective design asphalt contents and target air voids.

Researchers varied the asphalt content ± 0.5 percent from the target, the coarse aggregate blend ± 12 percent by weight, and the air voids ± 2.6 percent. In each design, the predominant coarse aggregate was substituted with the same limestone aggregate. In total, researchers fabricated and tested 40 unique slabs.

Table 15. Baseline Mixture Designs for Lab Mixture Variability Study.

Mixture Name	Mix Type	Binder Type	Optimum AC (%)	Theo. Max SG	RAP/RAS
SH 6-Valley Mills-DG D	DG-D	64-22	6.1	2.416	Yes
SH 6-Lake Waco-TOM C	TOM-C	76-22	6.6	2.397	No
SH 30-College St-SMA C	SMA-C	76-22	6.0	2.380	Yes
SH 149-Beckville-SP C	SP-C	76-22	5.3	2.469	Yes
SL 79-Del Rio-DG B	DG-C	64-22	4.5	2.453	Yes

Table 16. Example Test Plan for One Mixture in Lab Variability Study.

Slab ID	AC Rank	Coarse Agg Substitution Rank	Air Voids Rank	AC, %	Coarse Agg. Substitution, %	Air Voids, %
SH 6-DG D-1	M	M	L	5.2	0	3.3
SH 6-DG D-2	M	M	H	5.2	0	8.5
SH 6-DG D-3	L	M	M	4.7	0	5.9
SH 6-DG D-4	H	M	M	5.7	0	5.9
SH 6-DG D-5	M	L	M	5.2	-12	5.9
SH 6-DG D-6	M	H	M	5.2	12	5.9
SH 6-DG D-7	L	H	L	4.7	12	3.3
SH 6-DG D-8	H	L:	H	5.7	-12	8.5

Each mixture was batched and then slabs molded using an asphalt roller compactor at the target air voids content. Researchers measured the surface dielectric of each slab was measured using one GPR antenna along five linear profiles as Figure 40 illustrates. Care was taken to avoid the slab edges, which significantly alter the behavior of reflecting radar signals. To further mitigate possible edge effects, other asphalt slabs were placed adjacent to the target slab during testing.

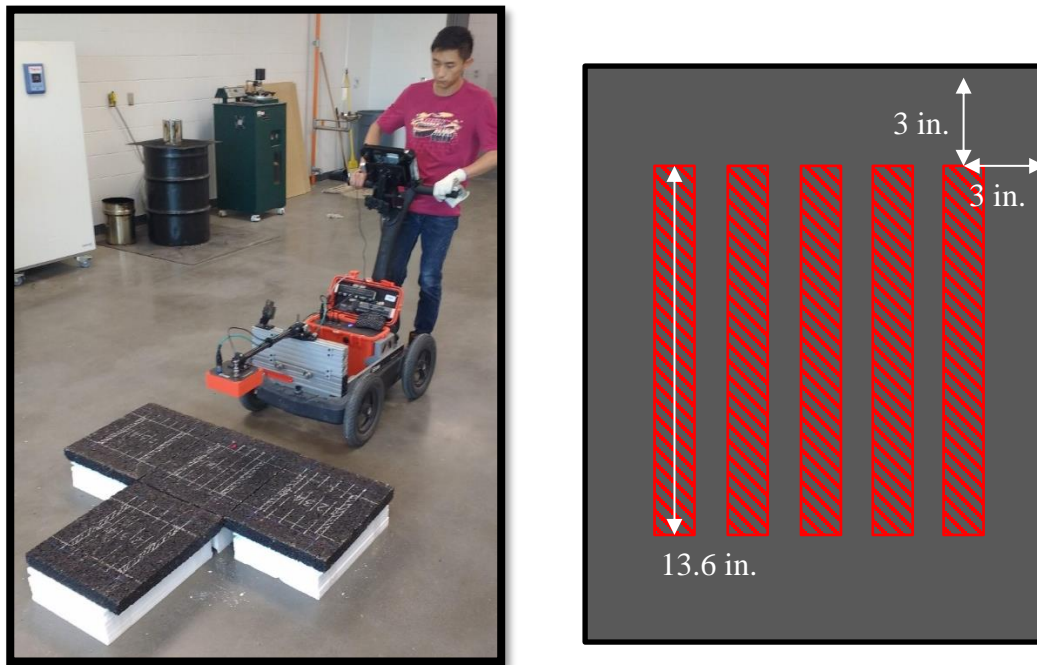


Figure 40. Surface Dielectric Profiling on Lab Slabs.

After dielectric testing, the bulk SG and air voids content of each slab were measured. The outer 2 inches of each slab were trimmed away, as this part of the slab had little influence on the dielectric measurements. Then the slabs were melted, uncoated aggregate removed, and the mixture theoretical maximum SG was tested. The theoretical maximum SG for each mixture was the average of this value and the value taken at the time of molding. The asphalt content was measured with an ignition oven following Tex-236-F. The asphalt correction factor used in the

associated TxDOT mix design was also applied to these mixtures. The bulk SG for each coarse aggregate was measured according to Tex-201-F. The aggregate SG was used as a surrogate for the coarse aggregate substitution and also as a surrogate for the aggregate dielectric constant.

Researchers analyzed the results using an analysis of variance with the response variable and model factors shown in Table 17.

Table 17. ANOVA Response Variable and Model Factors

Response Variable	Model Factor
Surface Dielectric	Mix Design
	Air voids
	Coarse Aggregate SG
	Asphalt Content
	Mix Design * Coarse Aggregate SG
	Mix Design * Asphalt Content

RESULTS

Shadow Quality Assurance Testing on New Construction

Figure 41 presents the empirical calibrations developed from the new construction projects tested. The data show that the calibration must be determined for each mix. Even if the mix type is the same, different mineralogy of aggregates and other mixture design factors mean that a calibration must be performed to each job. Appendix E presents details of test data from each construction project.

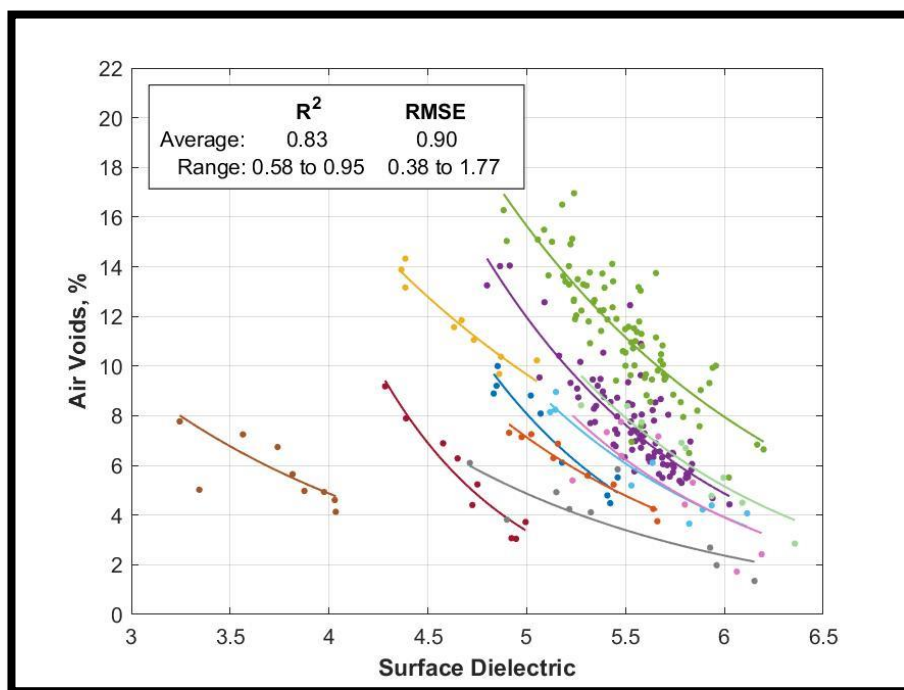


Figure 41. Calibrations to Air Voids from GPR for All Projects.

Figure 42 presents the fit of measured versus predicted voids when using GPR for density measurement. The first plot represents the prediction of air voids for cores taken from the same lot as the calibration. In this case, little bias exists, and the air void measurement from GPR for any specific point on the mat should be within 2 percent air voids of the actual air void content at that location.

The second plot shows the prediction of air voids for cores taken from a different production lot than the calibration. The margin of error is still 2 percent, but the average bias is 0.5 percent air voids, and individual projects show a bias ranging from -1.6 to 2.1 percent air voids. Figure 43 further illustrates this finding, where some projects show no bias in the data while others have significant bias.

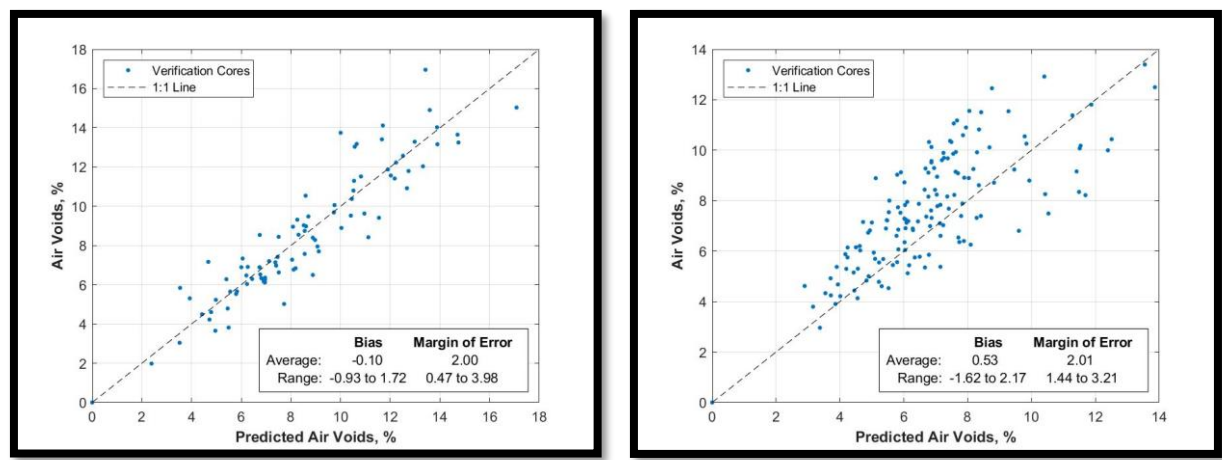


Figure 42. Predicted vs Actual Air Voids.

left: same lot as calibration; right: different lots than calibration

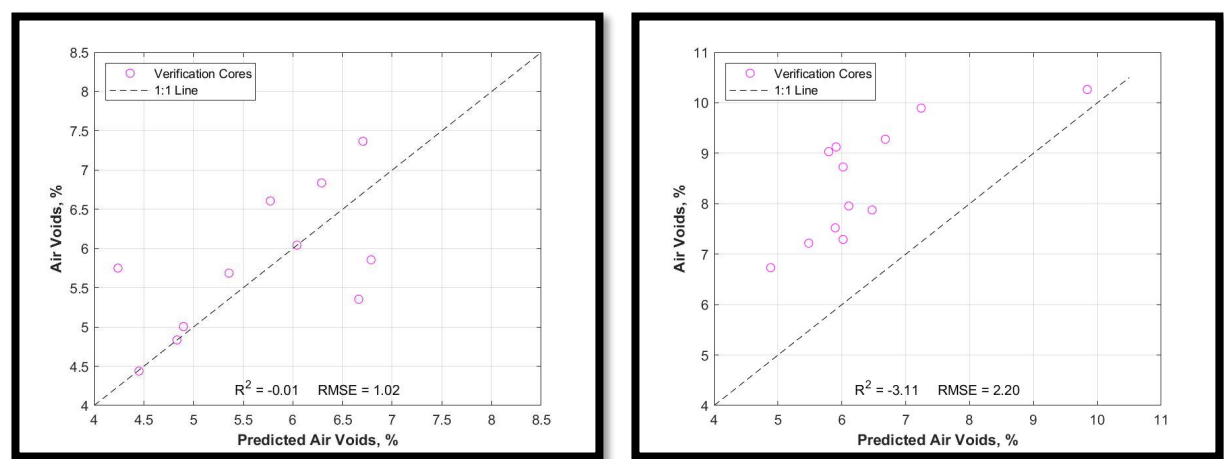
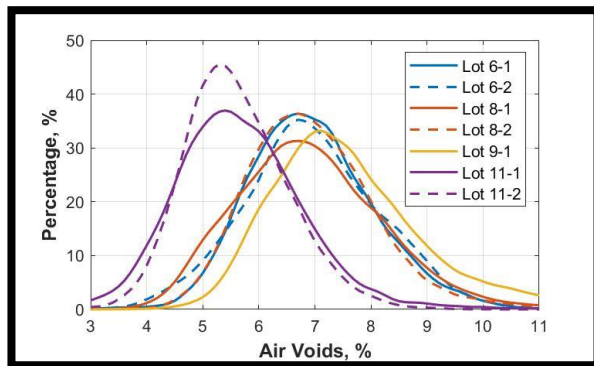


Figure 43. Examples of Non-Biased (Left) and Biased (Right) Predictions.

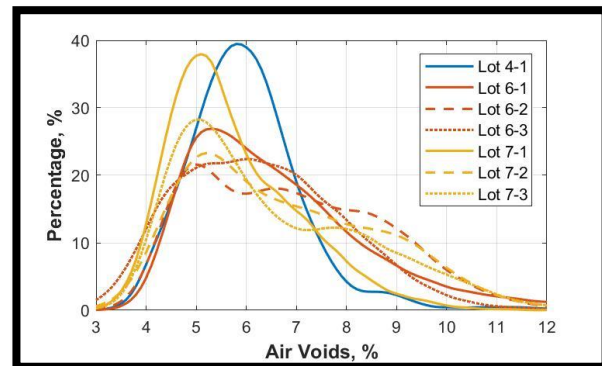
Table 18 and Figure 44 illustrate how the GPR tool can be used to identify the statistical distribution of the air voids over a constructed area. These data, particularly in Figure 44, show that even with a particularly project the air void distributions can change significantly across production lots.

Table 18. Example Summary Statistics of Air Voids on Two Projects.

Project	Lot	Sublot	Predicted Air Voids (%)				
			Average	St. Dev.	Median	5th_Percentile	95th Percentile
SH 6-Valley Mills	6	1	6.9	1.1	6.9	5.3	8.9
		2	6.9	1.2	6.9	5.0	9.0
	8	1	6.9	1.3	6.8	4.9	9.2
		2	7.0	1.2	6.9	5.3	8.9
	9	1	7.7	1.6	7.4	5.7	10.6
	11	1	5.7	3.2	5.6	4.0	7.6
		2	5.6	0.9	5.5	4.2	7.2
IH 45-Huntsville	4	1	6.0	1.2	5.9	4.4	7.9
	6	1	6.8	3.3	6.3	4.5	10.6
		2	6.9	1.9	6.7	4.4	10.2
		3	6.3	1.9	6.2	3.9	9.1
	7	1	5.8	1.3	5.5	4.1	8.2
		2	6.8	1.9	6.4	4.2	10.1
		3	6.5	1.9	6.0	4.2	10.1



(a)



(b)

Figure 44. Example Distribution of Air Voids by Sublot: (a) SH 6-Valley Mills and (b) IH 45-Huntsville.

Figure 45 illustrates a heat map display of the measured air voids over the constructed mat area and provides a quick visual reference of potential problem zones of high air voids or, less commonly observed, over-compacted locations. The first map shows the playback view from the GPR manufacturer's software. The presented data can be smoothed in the direction of travel using a moving average, but interpolation between the different line scans is not possible. To generate the second heat map, the data may be post-processed using other software. This map was created in Surfer; similar plots can be created using data analysis and plotting software like MatLab.

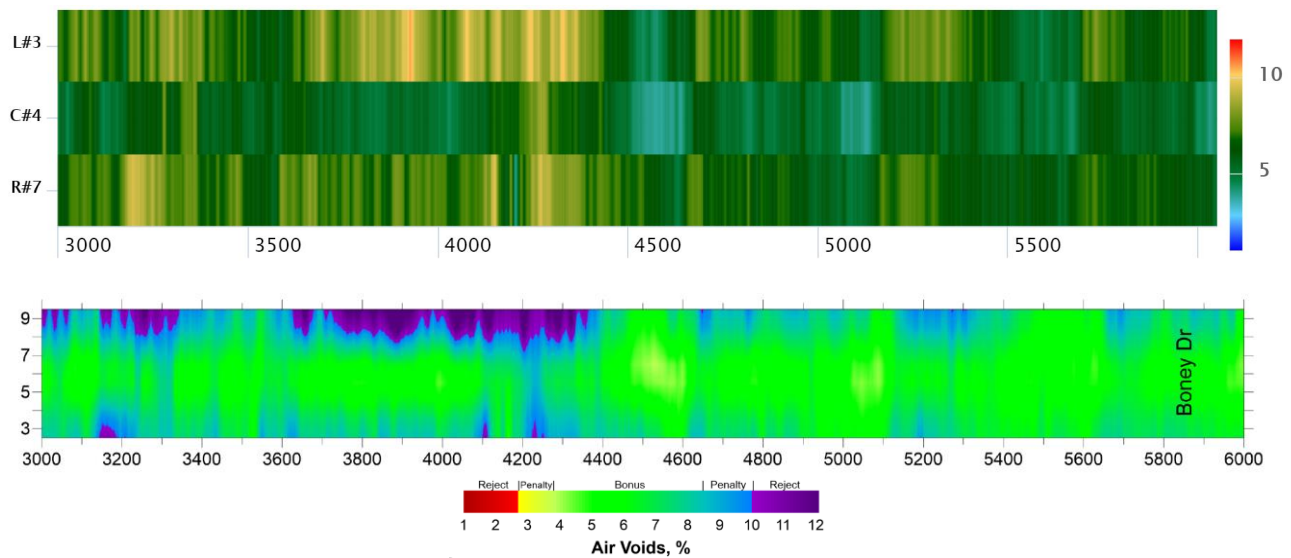


Figure 45. Example Air Voids Heat Maps for SS 248-Tyler: (a) Built-in Software and (b) Mapping Software after Post-Processing.

Forensic Testing

US 287 – Groveton

The resulting density calibration in Figure 46 had an R^2 -value of 0.82, which is typical of this work. Applying this calibration to the rest of the project, Figure 47 illustrates the average air voids for the north and southbound lanes were 4.0 and 3.7 percent, respectively. The spread on the data was considerably tight with most of the data lying within a 2 percent air voids spread. Compared to the in-place air voids payment table in Item 344, the pavement seems to meet density requirements, and if anything, may be over-compacted. However, making this comparison is not entirely appropriate, since the road had been in service for over 6 months at the time of testing.

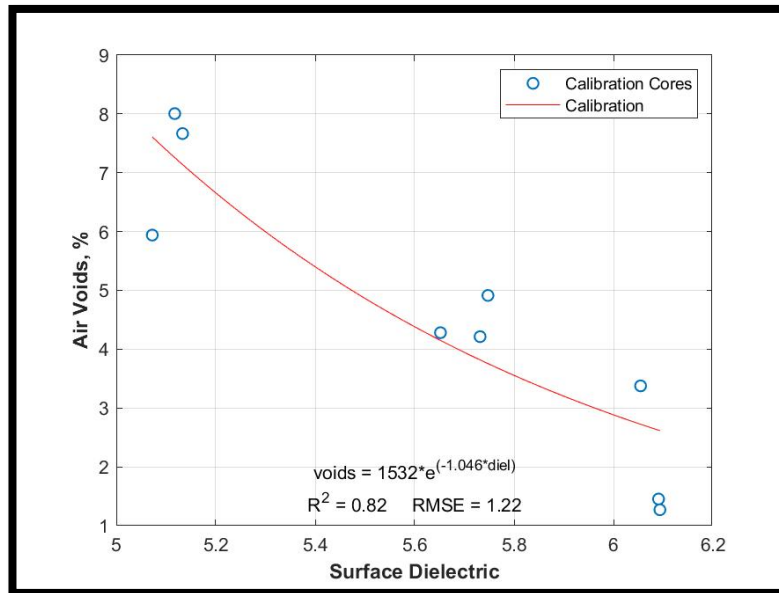


Figure 46. Dielectric to Air Voids Calibration for US 287.

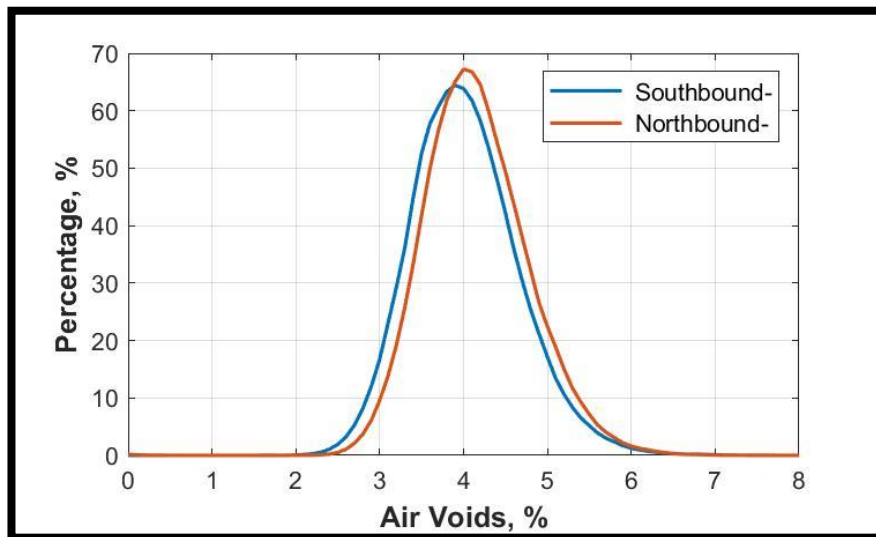


Figure 47. Overall Air Voids Distributions for US 287.

Figure 48 presents an excerpt of the heat map of air void distributions. The color legend on these maps is set to match the pay-penalty factors of Item 344: green = bonus, orange and blue hues = penalty, solid red and purple = remove and replace. If this were newly constructed pavement, most of the project would have been over-compacted. There is evidence though of traffic-related compaction as higher density within the wheel path is noticeable.

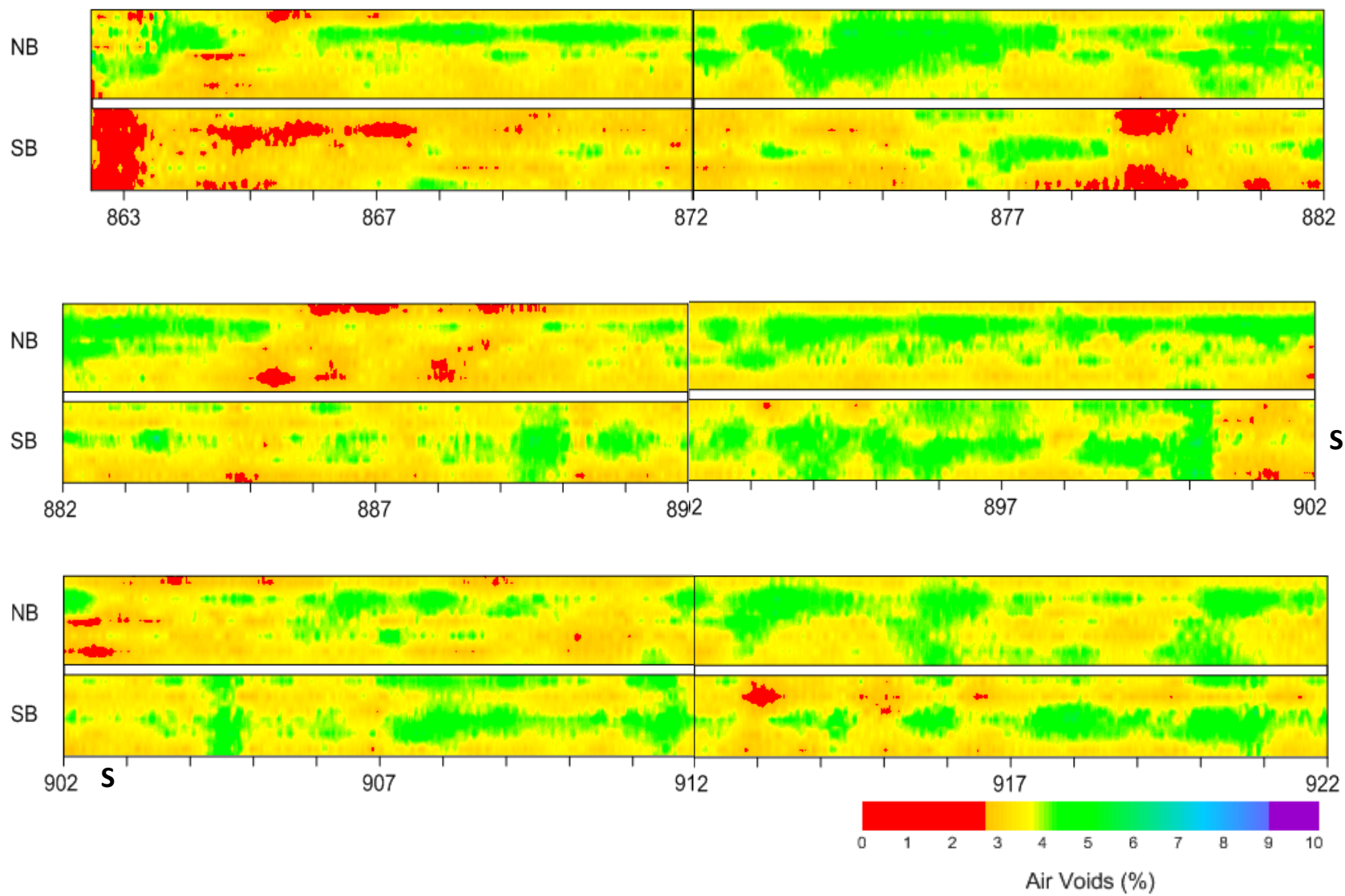


Figure 48. Excerpt from Air Void Distribution Map for US 287.

Figure 49 presents the calibration developed on SS 248. Applying this calibration to the rest of the project, Table 19 presents the percent within each placement pay factor region only from between the wheel paths, which is considered untrafficked and therefore as representative of as constructed as possible.

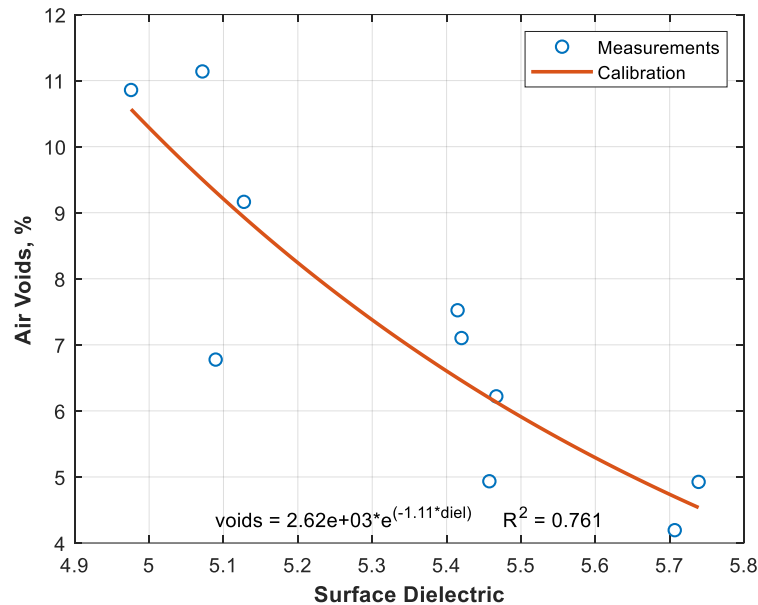


Figure 49. Calibration of Air Voids to GPR on SS 248.

Table 19. Percent within Placement Categories for SS 248, between Wheel Paths Only.

Section	Air Voids (%)		Payment, Percent Within Limits		
	Avg.	St Dev	Bonus	Penalty	Remove and Replace
EBOL	6.0	1.04	97.3	2.4	0.3
WBOL	5.8	0.80	99.4	0.6	0.1
EBIN	5.3	0.85	98	1.9	0.1
WBIL	5.3	0.65	99.7	0.3	0.0
CTL	6.3	1.12	95.3	4.0	0.6

Laboratory Sensitivity Testing

Table 20 summarizes three sensitivity models. The models consider which mixture properties have the greatest influence on the surface dielectric. Appendix E presents the full laboratory and statistical results.

Table 20. Summary of Dielectric Sensitivity Study.

Model #	Model R ²	Model Factor	Parameter Estimate	p-value	Significant
1	0.72	Air Voids	−0.08	<0.001	Yes
		Coarse Agg. SG	−3.47	<0.001	Yes
		Asphalt Content	−0.12	0.011	Yes
2	0.92	Mix Design	From −0.32 to 0.10	<0.001	Yes
		Air Voids	−0.11	<0.001	Yes
		Coarse Agg. SG	−0.08	0.133	No
		Asphalt Content	−0.09	0.941	No
3	0.95	Mix Design	−0.97 to 3.19	0.036	Yes
		Air Voids	−0.12	<0.001	Yes
		Coarse Agg. SG	22.6	0.022	Yes
		Asphalt Content	−0.13	0.020	Yes
		Coarse Agg. SG * Mix Design	−27.0 to 90.9	0.012	Yes

In the first model, all three parameters (air voids, coarse aggregate SG, and asphalt content) were statistically significant. The parameter with the most leverage (greatest influence) was the air voids content. The effect of coarse aggregate SG and asphalt content also had a significant effect on the dielectric, which explains why different mix designs require different calibrations.

By including a mix design factor in the second model, researchers evaluated the dielectric sensitivity from varying each property within a given mix design. The mix design itself accounted for most of the change in dielectric between certain designs. Some designs were not statistically different. Changes in the aggregate SG and in air voids were also significant, though less influential than in the first model.

The last model included an aggregate SG*mix design interaction term. All factors and the interaction were significant. The most influential factor was air voids, followed by the aggregate SG*mix design interaction. The interaction parameter estimate ranged from −27 to 90, suggesting that the trend between dielectric and aggregate SG was positive in some cases and negative in others. Asphalt content was also significant, with moderate overall influence.

The lab sensitivity study shows that day-to-day changes in the mixture within the range studied do have influence on the dielectric, though not as significantly as air voids content or switching to a different mix design. Table 21 summarizes the expected change in dielectric within a project. The effect of asphalt content would only change the dielectric by ± 0.03 . Changing the aggregate SG does change the dielectric, but within the test range of 12 percent substitution, the change in dielectric would only be ± 0.04 to ± 0.08 .

Table 21. Application of Sensitivity Results.

Property	Expected Change of Property Within a Construction Project		Estimated Change in Dielectric
Avg. Air Voids (%)	±2.0		±0.24
Coarse Agg. SG	In practice:	Likely only with mix design change	NA
	In lab study:	±0.019	±0.04 to ±0.08*
Asphalt Content (%)	±0.2		±0.03

* Will vary considerably based on the original and substitute aggregate.

CONCLUSIONS

Results from Phase II of this project evaluating the use of new GPR solutions for the air void evaluation of asphalt construction show:

- This GPR tool works for evaluating the density of asphalt mixtures.
- The empirical calibration approach provides accurate measurements of air voids, though there may be some unexplained bias among calibrations on different days. This may be mitigated by testing a standard reference material each day.
- The GPR tool can help with decision making on forensic projects.
- The dielectric is sensitive to air voids, aggregate SG (a surrogate for the aggregate dielectric), and asphalt content; however, on a given project, the dielectric is almost exclusively sensitive to air voids.

Many avenues of possible use for GPR exists in a construction setting, including:

- A no risk process control enhancement.
- For pay factor or acceptance framework.
- To evaluate longitudinal joints.
- To evaluate lots or sublots when random QC/QA cores result in a remove/replace decision. Use the GPR assessment to define how widespread the problem is and identify areas that do not need correction.
- For forensic investigations; however, it is difficult to predict backward in time what the air void content or distribution may have been at the time of construction. A density evaluation with GPR in a forensic investigation can provide a snapshot of what densities currently exist, but cannot rule out the uncertainty that densification may have happened in the wheel paths since the time of construction.

Awareness of GPR for asphalt mixture air void assessment is growing, and the technology readiness is high. Departments should seriously consider how they could leverage this technology to enhance process control and construction quality inspection moving into the future.

CHAPTER 4. CONCLUSIONS

This project expanded on the technology readiness of three non-destructive tools for potentially enhancing quality inspection, asset management, or forensic investigations in flexible pavements. These tools included:

- Mechanics-based models for base course.
- CMS for asphalt mixture process control.
- GPR for asphalt mixture construction quality assessment.

The first and third of these topics share heavy use of GPR, while the CMS relies upon precise tracking of a breakdown roller's passes and a CI concept. This chapter summarizes the results for each technology.

MECHANICS BASED MODELS FOR BASE COURSE

Mechanics-based approaches using the self-consistent model, PaveSCM, showed good promise for estimating base course density and moisture content. The approach for estimating base layer modulus with LayerMAPP at a controlled test site tracked reasonably with the FWD with an average error of about 14 ksi or less. Results estimating modulus did not match well with a base containing a very low percent of non-plastic fines, suggesting an alternate model is needed for these special cases. In an asset management context, estimating modulus with LayerMAPP shows general promise, but researchers recommend a minimum $\frac{3}{4}$ -inch thick surface layer to avoid distortion of the GPR signal.

Exploratory work using the mechanics-based models also suggest PaveSCM may be a suitable tool for density or moisture content measurement of stabilized materials. Additionally, researchers derived a potential non-destructive framework to measure stabilizer content in the field.

Consideration should be given to further validate the PaveSCM approach, better define proper operating environments for LayerMAPP's modulus prediction, and further research estimating stabilizer content from NDT.

COMPACTION MONITORING SYSTEM

The CMS provides real-time feedback of adequacy of rolling patterns. While this concept is not new, the ability of a quick and temporary install may be of interest to some potential users. The driving factor in CMS development, specifically to estimate density from the compaction index concept on a breakdown roller, proved quite complex. Even after development of revised drum efficiency factors, a mix temperature factor, and an approach to account for vibration in the compaction index model, the ability of the CMS to truly estimate density is limited. The best potential use of the CMS is likely in process control to provide continuous feedback with far more testing coverage than routine use of a density gauge.

GPR FOR ASPHALT MIXTURE CONSTRUCTION QUALITY

Industry continues to demonstrate growing interest in GPR for asphalt mixture quality evaluations. The empirical approach to relate the GPR-measured surface dielectric constant to the asphalt mixture air void works. This calibration currently must be determined for each project. In some cases, there is unexplained bias among calibrations on different days, though this may be mitigated by testing a standard reference material each day. Due to the quantity of observations, in a potential QC or even QA setting, the acceptance risk to both Contractor and Owner/Agency are significantly reduced.

Many avenues of possible use for GPR's ability to measure asphalt mixture density exist. In a construction setting, some potential approaches could include:

- As a no risk process control enhancement.
- For pay factor or acceptance framework.
- To evaluate longitudinal joints.
- To evaluate lots or sublots when random QC/QA cores result in a remove/replace decision. Use the GPR assessment to define how widespread the problem is and identify areas that do not need correction.
- For forensic investigations.

The promising results from this tool in both construction and forensic settings, combined with the magnitude of development history and case studies during the Phases of this project, make GPR for asphalt mixture density evaluation a good candidate for implementation efforts.

Consideration should be given to provide demonstrations to Contractors in a construction setting, define key output desired by stakeholders in a standardized format, and develop methods to quickly produce that output on a routine basis. Consideration should also be given to wider spread use, as appropriate, of this tool in forensic settings.

Further research topics warranting efforts include expedited, benchtop methods to determine the calibration, refined regression methods to handle the influence of outliers in the calibration data set, and exploration of how this tool could be used on mixes such as PFC or TOM, which are not currently accepted based on density measurements.

APPENDIX A. TEST PLAN FOR RELIS TEST SITE WITH COMPACTION MONITORING SYSTEM

ROLLING PATTERNS FOR ASPHALT LAYERS

Researchers specified rolling patterns for both the Type-D layer and TOM-F layer during compaction. Three different compaction levels were considered for the test sections. The compaction level and rolling pattern of each test section were specified as shown in Figure 50 and Table 22. A Dynapac CC522VHF breakdown roller was used to compact all asphalt layers during construction. The number of roller passes and the vibration (on or off) were primary factors to control the rolling patterns and compaction levels. Each section was divided into three strips (approximately 150 ft long) and had a transition zone of 50 ft long.

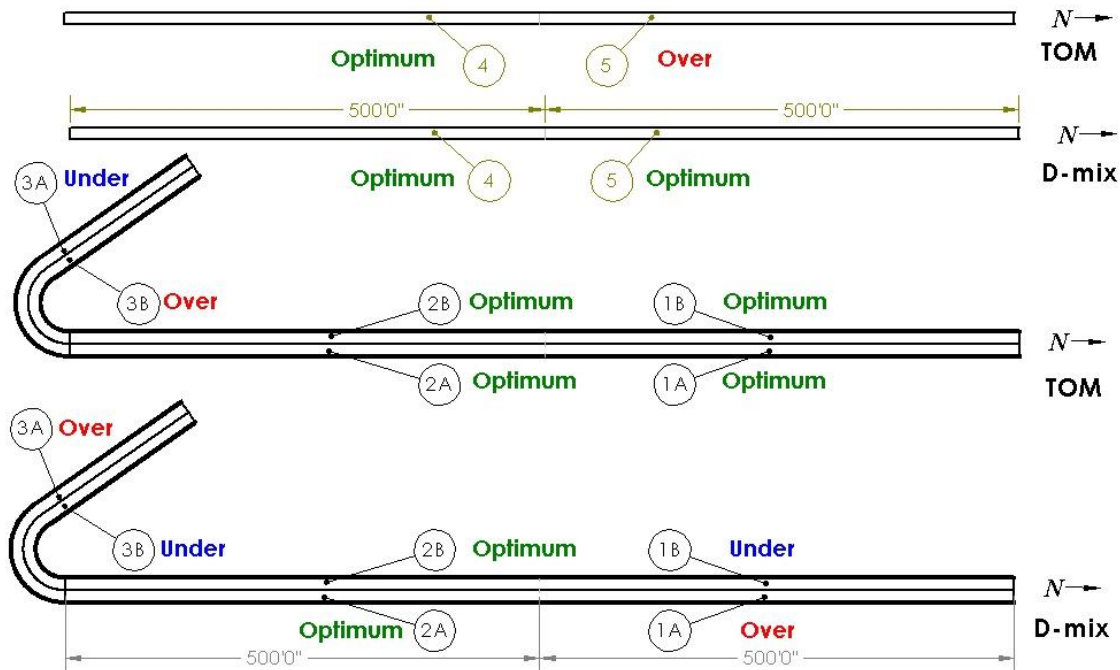
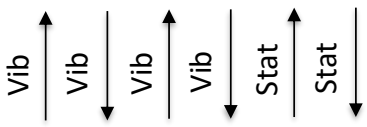
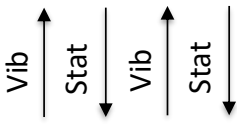
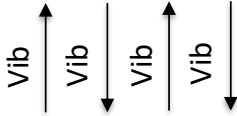
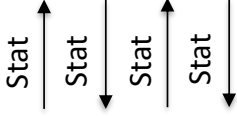
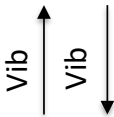
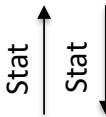


Figure 50. Layout for Test Section Compaction Levels.

Table 22. Rolling Patterns Used for Asphalt Layers.

Levels	Type-D Layer	TOM-F Layer
Over		
Optimum		
Under		

FIELD TESTS AND LABORATORY TESTS

Various field tests were performed to fully characterize each layer of the test sections during construction. Table 23 presents the field tests performed on each layer. During construction and field testing on asphalt layers, loose asphalt mixtures and field cores were collected for laboratory study.

Table 23. Field Tests on RELLIS Pavement Test Site.

Flexible Pavement Test Section				
Subgrade	Lime Treated Subgrade	Flexible Base	Type-D	TOM-F
- DCP ⁽¹⁾	- LWD ⁽²⁾ - 1-GHz GPR ⁽³⁾	- DCP - LWD - FWD ⁽⁴⁾ - 1-GHz GPR	- FWD - 1-GHz GPR - TPAD ⁽⁵⁾ - Cores - Nuclear density	- FWD - 1-GHz GPR - TPAD - Cores - Nuclear density
Rigid Pavement Test Section				
Existing Concrete			Type-D	TOM-F
- FWD - 1 GHz GPR - TPAD			- FWD - 1-GHz GPR - TPAD - Cores - Nuclear density	- FWD - 1-GHz GPR - TPAD - Cores - Nuclear density - Water flow
(1): Dynamic cone penetration test (2): Light weight deflectometer test (3): Ground penetration radar test (4): Falling weight deflectometer test (5): Total pavement acceptance device test				

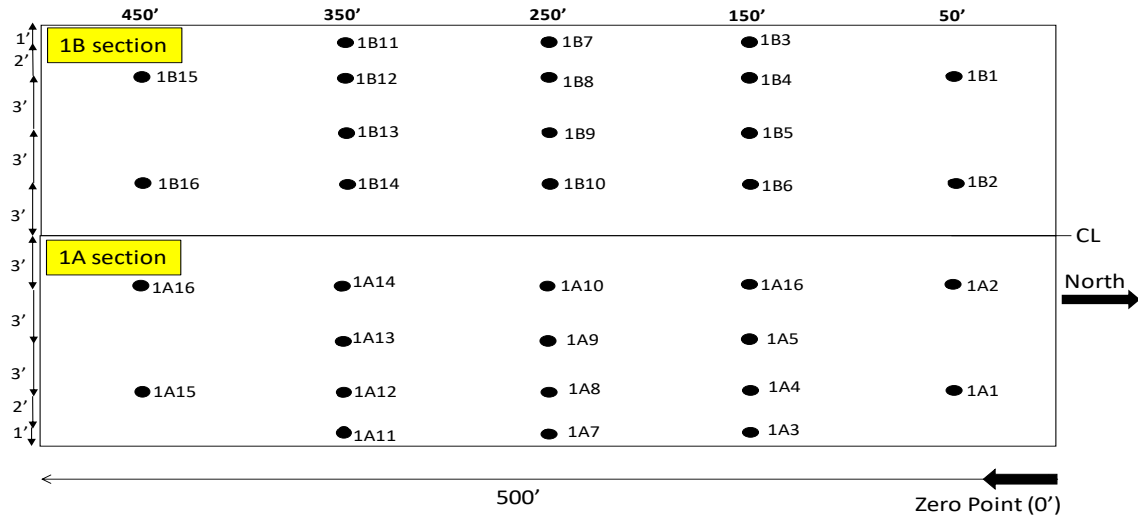
Table 24 presents a series of laboratory tests performed on field cores and loose asphalt mixtures.

Table 24. Lab Tests on Cores and Loose Asphalt Mixtures.

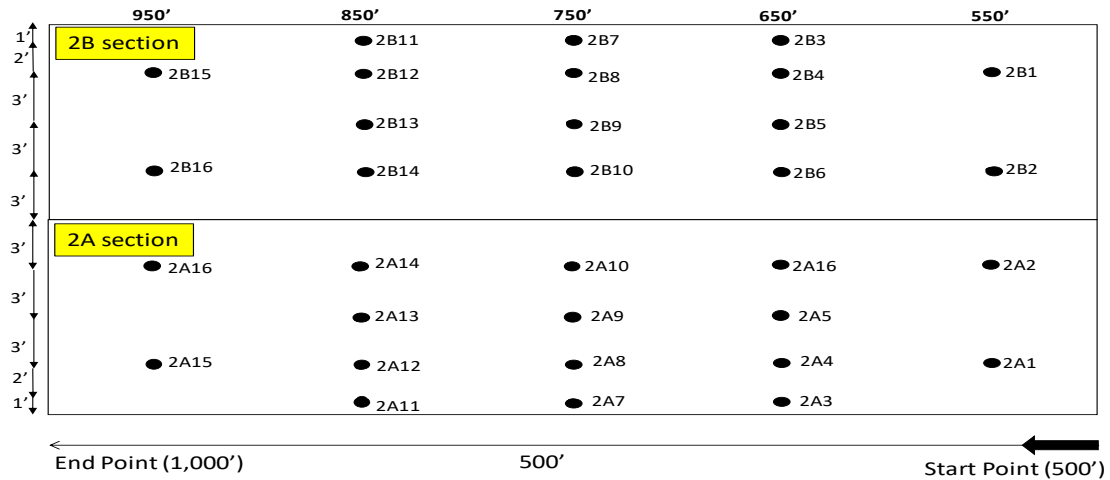
Material	Core	Loose mix
Type-D mix	<ul style="list-style-type: none"> - Thickness measurement - Bulk specific gravity test - Mr test - IDT test - Hamburg test - Overlay test 	<ul style="list-style-type: none"> - Rice specific gravity test - Mr test - IDT test (Mr testing samples) - Hamburg wheel tracking test - Overlay test - Dynamic modulus test - Repeated load test
TOM-F mix	<ul style="list-style-type: none"> - Thickness measurement - Bulk specific gravity test 	<ul style="list-style-type: none"> - Rice specific gravity test - Mr test - IDT test (Mr testing samples) - Hamburg wheel tracking test - Overlay test - Dynamic modulus test - Repeated load test

DENSITY TESTS ON ASPHALT LAYERS

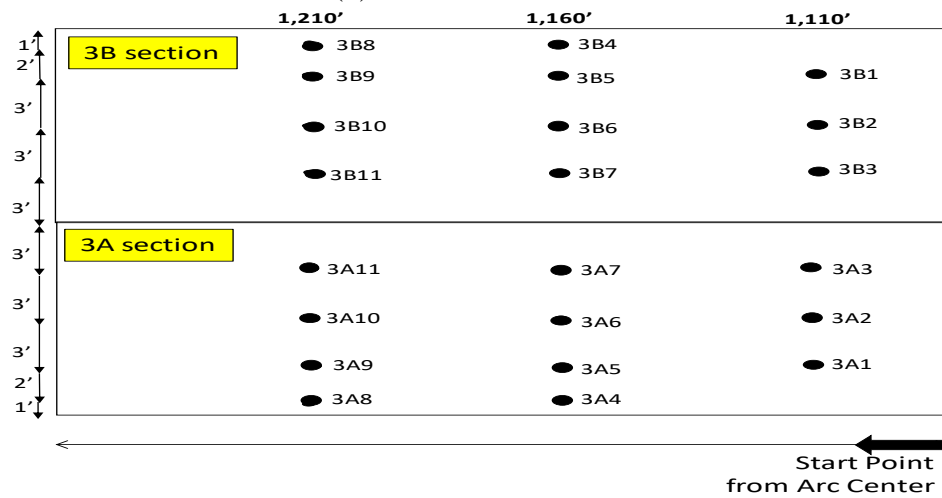
Figure 51 and Figure 52 show a total of 118 locations for each asphalt layer (86 locations in flexible pavement section and 32 locations in rigid pavement section). The cutting of 118 total cores for each asphalt layer was then performed at the testing locations. The lab measured each core's air voids and thickness. In addition, the GPS coordinate of each core's location was recorded to calculate the compaction index at those locations from the CMS.



(a) Section-1A and 1B



(b) Section-2A and 2B



(c) Section-3A and 3B

Figure 51. Density and Core Locations in Flexible Pavement Section.

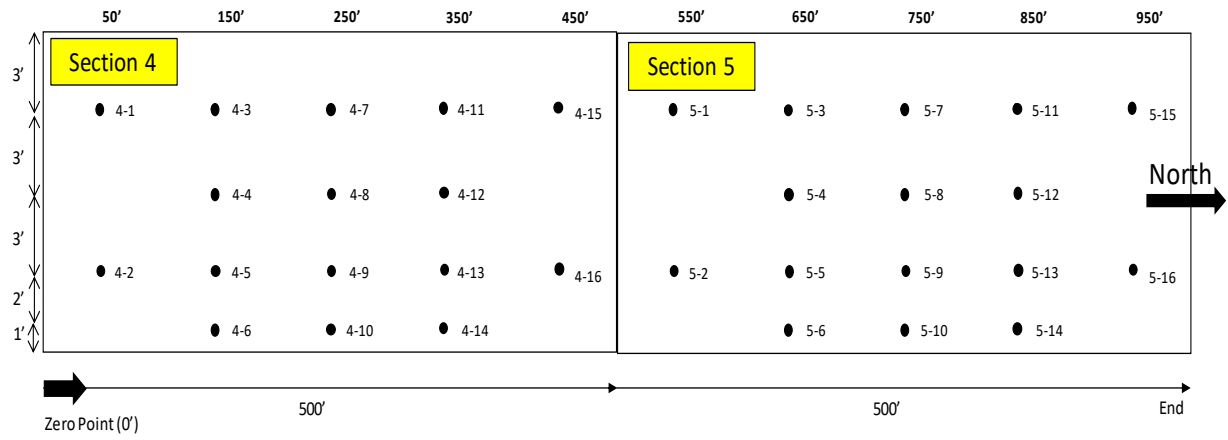


Figure 52. Density and Core Locations in Rigid Pavement Test Section.

APPENDIX B. SCHEDULE OF RELIS TEST SITE ACTIVITIES

Table 25. Daily Activity Record.

Date	Contractor	TTI
7-11-2017	- Pre construction meeting	
7-24-2017	- Began constriction - Cleaned and graded natural subgrade	- Checked progress
7-25-2017	- Cleaned and graded natural subgrade - Ran proof rolling	- Checked progress
7-26-2017	- Finished cleaning and grading natural subgrade	- Performed field tests on natural subgrade (DCP, Boring, Percometer)
7-27-2017	- Applied lime to natural subgrade (total amount delivered was 70.52 tons) - Added water and mixed	- Checked progress
7-28-2017	- Watered - Mellowing period	- Checked progress
7-29-2017	- Mellowing period	
7-30-2017	- Mellowing period	
7-31-2017	- Pulverized and mixed - Watered	- Ran sieve analysis on lime stabilized subgrade - Ran nuclear density gauge to check moisture content - Collected loose field mix
8-1-2017	- Compacted LTS layer	- Checked progress
8-2-2017	- Curing	- Measured density and thickness of LTS layer
8-3-2017	- Compacted LTS layer	- Measured density of Section-3 - Sampled base material from contractor's yard
8-4-2017	- Compacted and graded LTS layer	- Measured density of Section-3 - Sampled LTS material from Section-3 to run a M-D curve
8-5-2017	- Curing period	
8-6-2017	- Curing period	
8-7-2017	- No activities due to rain	
8-8-2017	- Dewatered	- Checked progress
8-9-2017	- Drying	- Checked progress
8-10-2017	- Drying and grading surface	- Measured densities and moistures
8-11-2017	- Graded surface	- Checked progress
8-12-2017	- Curing period	
8-13-2017	- Curing period	
8-14-2017		- Ran field tests on LTS layer (LWD, 1 GHz GPR, and 2.5 GHz GPR) - Installed sensors
8-15-2017	- Curing period	
8-16-2017	- Curing period	
8-17-2017	- Delivered flexible base materials	- Checked progress
8-18-2017	- Delivered flexible base materials	- Sampled base materials
8-21-2017	- Compacted base layer	- Ran compaction monitoring system - Checked embedded sensors
8-22-2017	- Compacted base layer	- Ran compaction monitoring system - Checked embedded sensors - Measured densities and moistures
8-23-2017	- Compacted base layer	- Measured densities and moistures
8-24-2017	- No activities due to hurricane	

8-30-2017	- No activities due to hurricane	
8-31-2017	- Dewatered	- Checked progress
9-1-2017	- Compacted base layer	- Measured densities and moistures
9-5-2017		- Ran FWD, GPR, percometer tests on base layer
9-6-2017		- Ran LWD and DCP tests on base layer
9-13-2017	- Finalized base layer	- Checked progress
9-14-2017	- Applied tack coat onto top of base layer	-TPAD and FWD tests on rigid section (before Type-D placement)
9-15-2017	- Placed Type-D mix on flexible section	- Collected CMS data - Directed roller operations and patterns - Performed inspection and nuclear density tests - Collected loose mix
9-16-2017		- Ran FWD tests on Type-D mix layer in flexible section
9-17-2017		- Ran nuclear density tests on 86 spots of Type-D mix layer in flexible section
9-18-2017	- Placed Type-D mix on rigid section	- Collected CMS data - Directed roller operations and patterns - Performed inspection and nuclear density tests - Collected loose mix - Ran GPR and TPAD tests on Type-D mix layer in flexible section - Cut 86 cores of Type-D mix layer in flexible section
9-19-2017		- Ran FWD, GPR, and TPAD tests on Type-D mix layer on rigid section - Cut 32 cores of Type-D mix layer on rigid section
9-20-2017	- Placed TOM-F mix on both flexible and rigid sections - Finished construction	- Collected CMS data - Directed roller operations and patterns - Performed inspection and nuclear density tests - Collected loose mix - Ran nuclear density tests on 86 spots of TOM-F mix layer in flexible section - Ran nuclear density tests on 32 spots of TOM-F mix layer in rigid section - Ran GPR and Flow tests on both flexible and rigid sections
9-21-2017		- Ran FWD and TPAD tests on both flexible and rigid sections - Cut 86 cores of TOM-F mix layer on flexible section - Cut 32 cores of TOM-F mix layer on rigid section - Finished field tests

APPENDIX C.

CONSTRUCTION ACTIVITIES FOR PAVEMENT LAYERS AT RELLIS TEST SITE

SUBGRADE

Construction began with the natural subgrade in the flexible pavement test section. The contractor cleaned, graded the natural subgrade, and finished in three working days including proof rolling. Prior to subgrade construction, natural soil samples were collected to characterize the soil properties in the laboratory. The soil had liquid limit of 48, plastic limit of 16, and plastic index of 32. The optimum moisture content and the maximum dry density of the soil were determined as 98.4 pcf at 20.2 percent moisture. Figure 53 shows the construction process of the natural subgrade.



(a) Cleaning and grading

(b) Proof rolling

Figure 53. Subgrade Layer Construction.

LIME TREATED SUBGRADE

A total of 70.52 tons of pebble lime was applied to stabilize the natural subgrade. After a three-day mellowing period, the lime treated subgrade (LTS) layer was compacted targeting 6 inches thick and cured for several days until the measured density met at least 95 percent of the determined maximum density. The maximum dry density of the LTS material was 94.9 pcf at the optimum moisture content of 23.3 percent. Figure 54 shows the construction process of the LTS layer.



(a) Pebble lime application



(b) Pulverization and mix



(c) Compaction



(d) Thickness check



(e) Density check



(f) Surface Finalization

Figure 54. Construction of LTS Layer.

FLEXIBLE BASE

Flexible base materials were sampled from the contractor's yard before placement. The determined maximum dry density of the base material was 136.1 pcf at the optimum moisture content of 7.5 percent. Flexible base materials were delivered and placed for two working days. Thereafter, the base materials were compacted targeting 8 inches thick. During construction of the base layer, Hurricane Harvey interrupted activities, so the base layer had to be reworked and finalized several days later. Figure 55 shows the construction of the base layer.



(a) Base material delivery



(b) Compaction



(c) Final base surface

Figure 55. Construction Process of Flexible Base Layer.

TYPE-D ASPHALT LAYER

A Type-D asphalt mix was designed by the contractor. A PG 64-22 asphalt binder was used to produce the Type-D mixture with an asphalt content of 5.1 percent. The mixture was placed on both flexible and rigid pavement test sections. Prime coat was applied on the top of the flexible base layer, and tack coat to the existing concrete pavement, prior to placing the Type-D mixture. The target lift thickness on the both flexible and rigid pavement test sections was 2 inches.

Figure 56 shows the construction process of the Type-D mixture the flexible section, while Figure 57 shows placement of the Type-D mixture on the rigid section.



(a) Prime coat applied



(b) Type-D mix placement



(c) Compaction with CMS system

Figure 56. Type-D Placement at Flexible Pavement Test Section.



(a) Tack coat application



(b) Type-D mix placement



(c) Compaction with CMS system

Figure 57. Type-D Placement at Rigid Pavement Test Section.

THIN OVERLAY MIX-F (TOM-F) ASPHALT LAYER

As the final surface layer, a TOM-F asphalt mix was placed on the Type-D layer at both flexible and rigid pavement test sections. The TOM-F mixture was designed by researchers using materials available to the Contractor. A PG 76-22 asphalt binder was used to produce the mixture with asphalt content of 7.21 percent. The target lift thickness on the both flexible and rigid pavement test sections was 0.75 inches. Figure 58 shows the placement of the TOM-F mixture on both flexible and rigid pavement sections.



(a) Flexible pavement section



(b) Rigid pavement section

Figure 58. TOM-F Placement.

APPENDIX D. COMPACTION INDEX MODEL DEVELOPMENT

DRUM FACTOR

Figure 59 presents the revised drum factor developed during the course of this project. Currently, the models are not changeable by the user in the PLC.

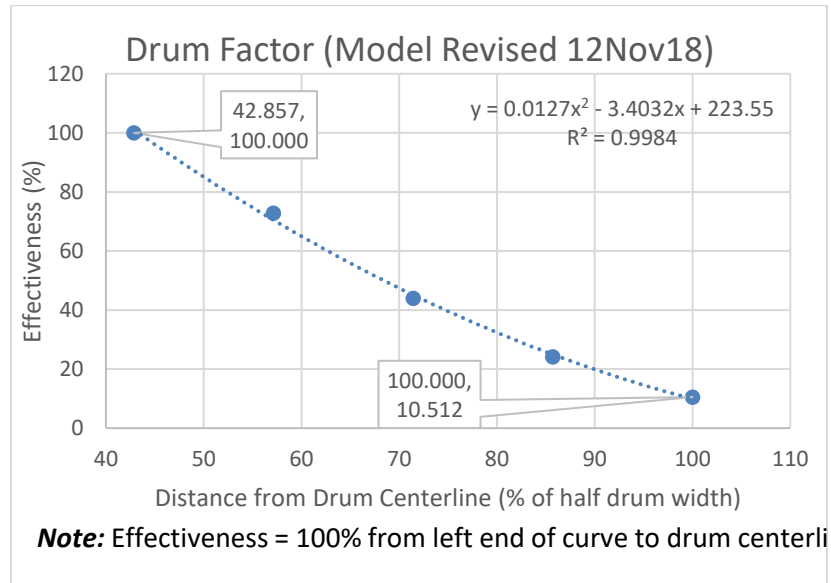


Figure 59. Revised Drum Efficiency Factor.

TEMPERATURE FACTOR

Researchers developed a temperature factor for the nominal 7 percent air void tests using SGC compaction curves. Figure 60 illustrates the results from IH 45.

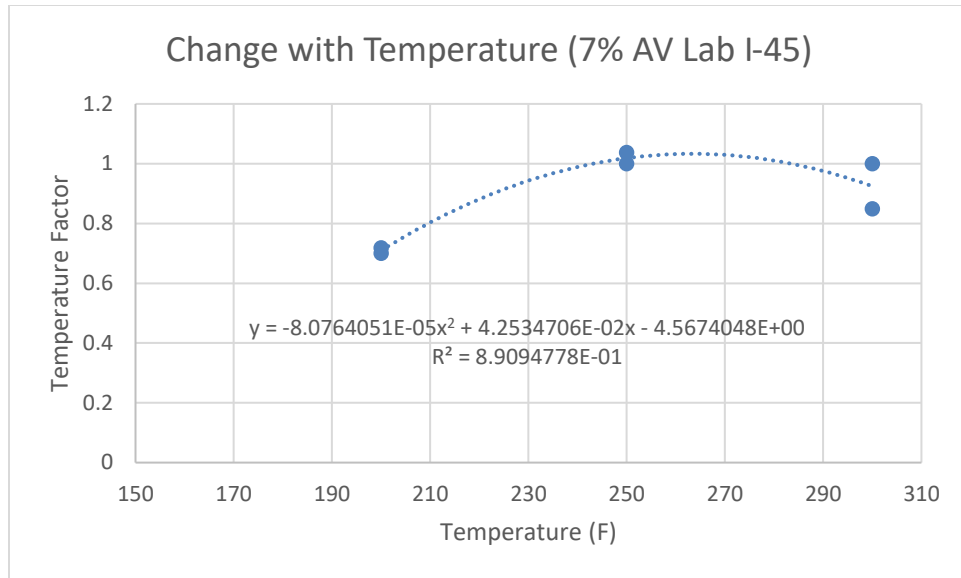


Figure 60. Temperature Factor Curve for IH 45 SMA Mix.

Because the target breakdown temperature may vary from mix to mix and job to job, it is not the best procedure to try to use one equation based on an average target temperature. Therefore, an approach based on a temperature difference between the target breakdown temperature and the actual temperature measured by the CMS was developed. Figure 61 and Figure 62 illustrate this approach. Unless a curve specific to the mix is developed using lab data, the polynomial fit on all data combined and forced through 1.0 as shown in Figure 62 is suggested for use in the CMS.

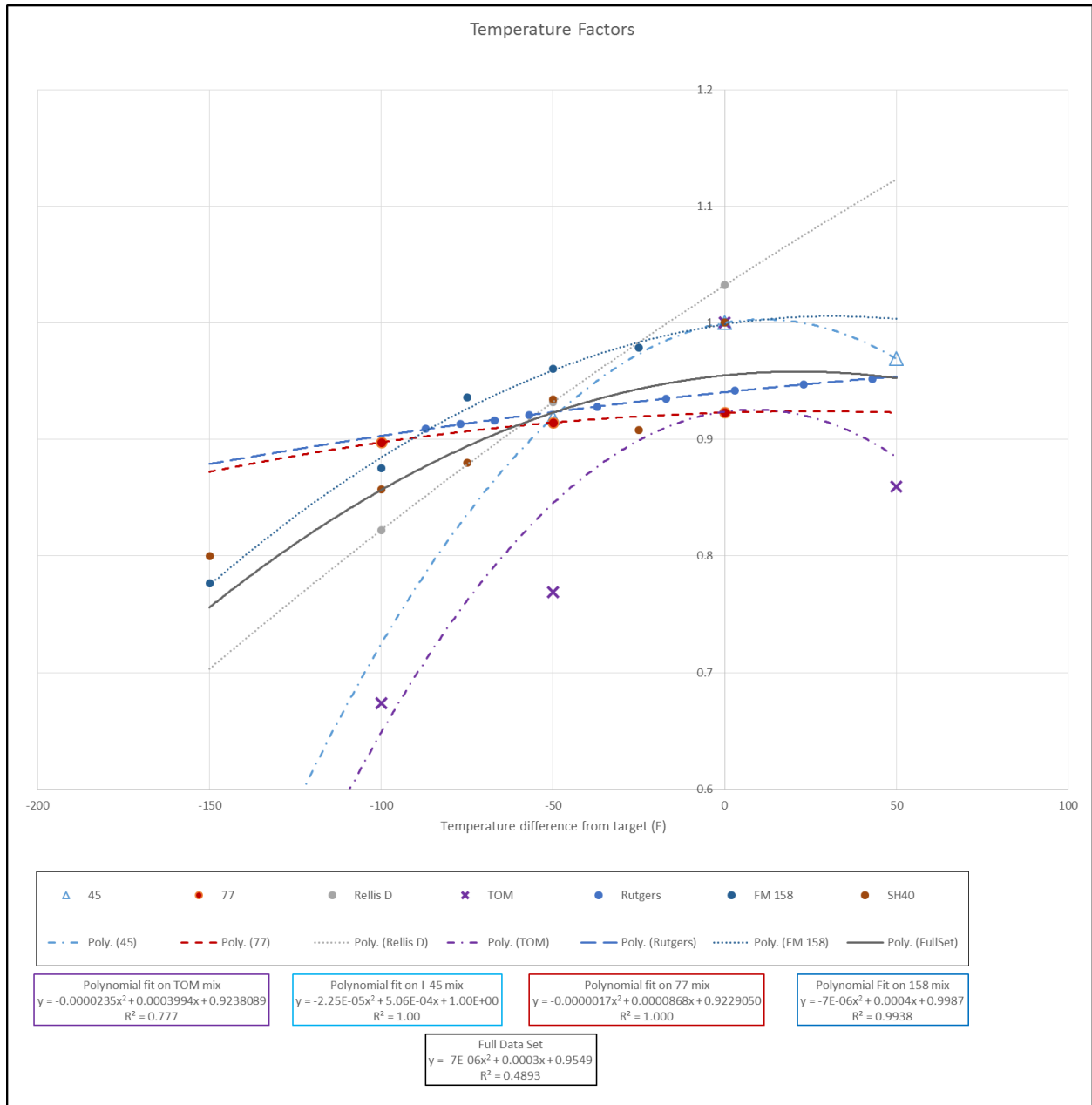


Figure 61. Temperature Factor Estimates Derived from Lab Compaction.

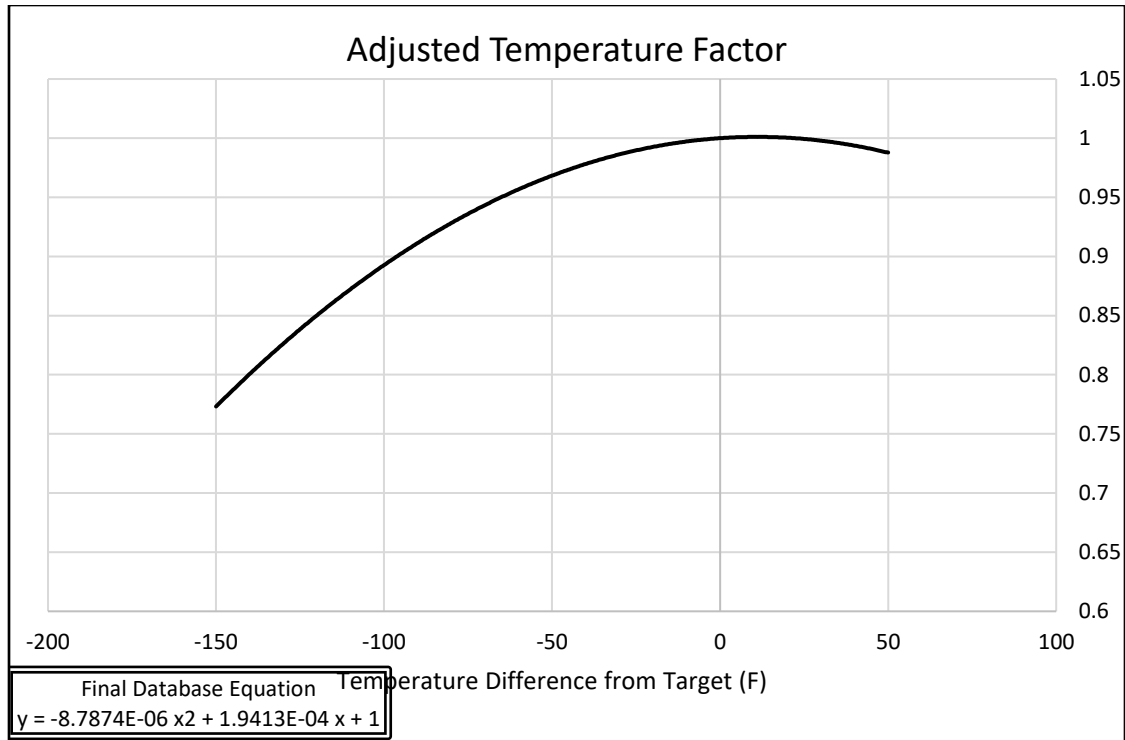


Figure 62. Recommended General Temperature Factor.

VIBRATION FACTOR

At this time, there has been no effective method developed to model the effect of vibration and the effect of the supporting structure.

Analysis was performed on data from all the RELLIS test sections in an attempt to develop a Vibration factor model. The following equations were used to evaluate the data:

Coverage Parameter

$$= \frac{\text{Coverages with Vibration}}{\text{Planned Optimum Coverages with Vibration}} + \frac{(\text{Total Coverages} - \text{Coverages with Vibration})}{\text{Planned Optimum Total Coverages}}$$

The Coverage Parameter was used as the effective Planned Rolling Pattern (X-axis) and then related to Nuclear Density measurements at the site. The Nuclear Median Factor (Y-axis) variable was computed as:

$$\text{Nuclear Median Factor} = \frac{\text{Nuclear Median Value for the Section}}{\text{Target Optimum Nuclear Median Value for the mix}}$$

Figure 63–Figure 65 present the results of the above analysis. While the results seem promising, there were not enough treatments on the high side (over-compaction above the expected optimum, $X > 1.0$) to confidently identify the peak and therefore how the model might be modified to give a factor of 1.0 at the planned optimum rolling pattern, yet show a drop on both the under- and over-compacted side of that point if appropriate. Such modification might involve curve shifting both vertically and horizontally.

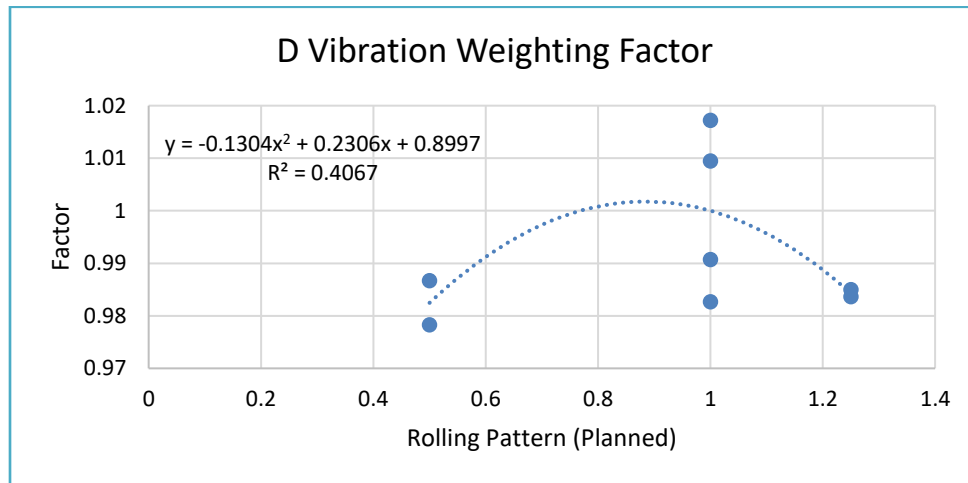


Figure 63. Type D Mix Vibration Factor Development.

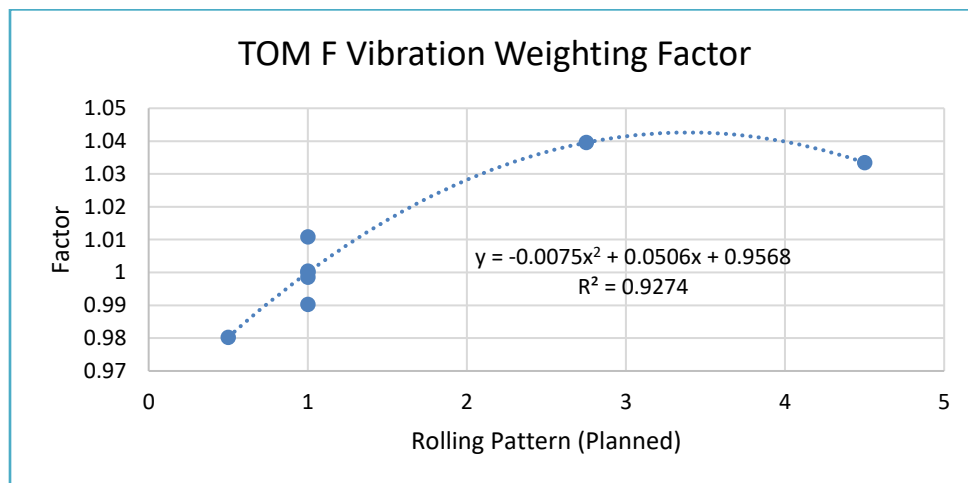


Figure 64. TOM F Mix Vibration Factor Development.

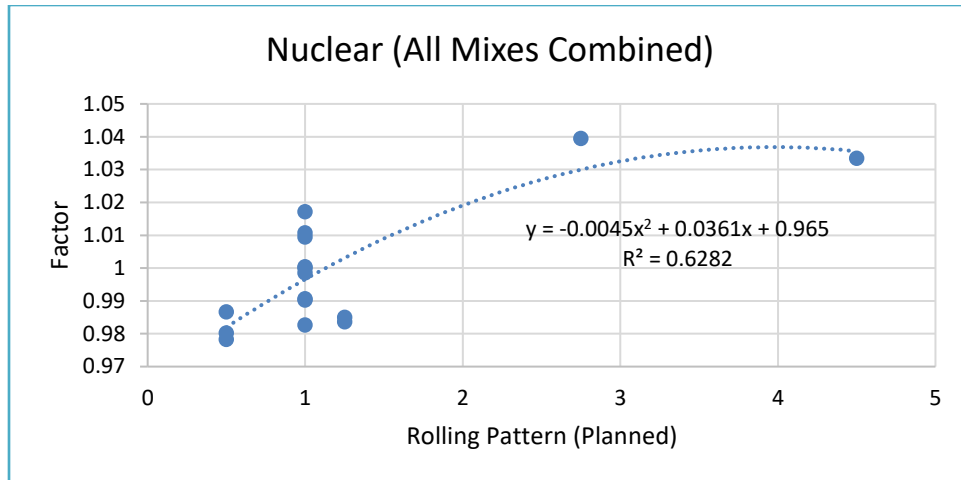


Figure 65. Vibration Factor Development (All RELLIS Sections Combined).

Due to the limited data available to vibration factor, researchers developed an alternative method. The following pseudo-code is currently used for the vibration factor computation in the PLC system. In this implementation, a coverage with vibration is simply assumed to be weighted twice the weighting factor of a static coverage. This simplification was implemented based on typical results from accelerometer measurements mounted on the compactors. In many cases, the accelerations appeared to be approximately 2 g, which is where the factor of 2 originated. However, when the compactor was of a type, such as an oscillating compactor, where the accelerometers could read accelerations substantially in direct contact with the mix (instead of damped by the suspension system), the accelerations were approximately double that of the damped measurements (i.e., approximately 4 g to -3 g).

IF vibration is included on the Defaults screen

 THEN *Effective Compaction Effort* = (*Total Coverages* –
Coverages with Vibration) + (2 * *Coverages with Vibration*)

 ELSE *Effective Compaction Effort* = *Total Coverages*

ENDIF

IF the compactor is actually vibrating (i.e. accelerometers are reading vibration)

 THEN Vibration Factor = 2.0

 ELSE Vibration Factor = 1.0

ENDIF

LAB COMPACTION INDEX

Researchers worked to develop a lab compaction index (LCI) that could be used to estimate the minimum field compaction index required to attain the target density. The LCI is defined as:

$$LCI = 100 * \frac{a^{1.2}}{b}$$

Where a and b are the absolute value of the slope and the intercept of the lab compaction curve, respectively.

Figure 66 illustrates how the compaction curves from the SGC determine the constants for a given mixture.

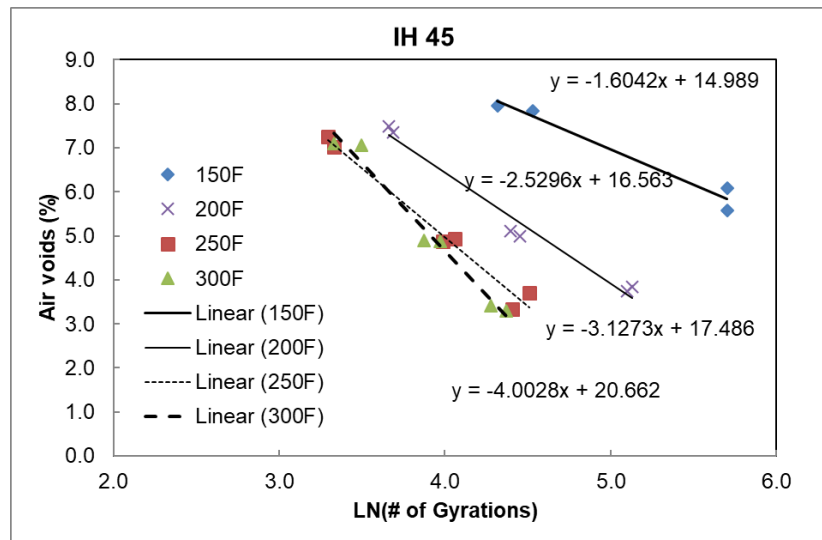


Figure 66. Example SGC Compaction Curves for Developing LCI.

Figure 67 illustrates that, when pooling the six mixes used in Phase II of this project with data available from 20 other mixes, a general trend may exist between the two values.

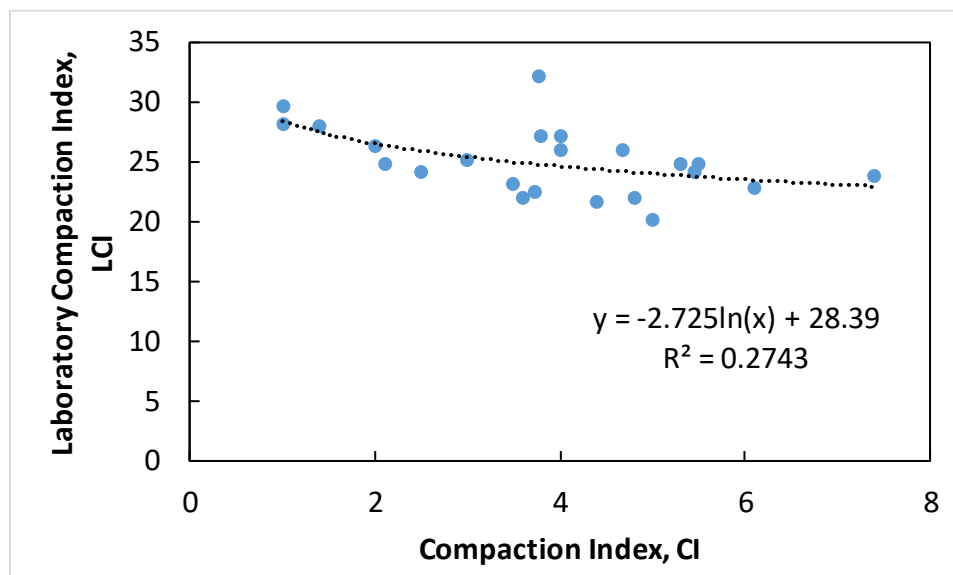


Figure 67. Correlation between LCI and CI.

APPENDIX E. TEST DETAILS OF GPR FOR ASPHALT MIXTURE CONSTRUCTION

FIELD PROJECTS

Table E.1. Calibration Summaries.

Project	R ²	RMSE	a	b
SH 6-Valley Mills-DG D	0.92	0.76	1679.7	-1.060
SH 30-College St-SMA C	0.94	0.45	490.9	-0.844
SH 6-Lake Waco-TOM C	0.91	0.73	183.5	-0.588
RELLIS-DG D	0.80	0.98	1213.5	-0.919
RELLIS-TOM F	0.85	1.07	550.7	-0.709
SL 79-Del Rio-DG B	0.97	0.55	336.8	-0.725
SH 149-Beckville-SP C	0.97	0.56	4529.0	-1.448
IH 45-Huntsville-SMA C	0.95	0.58	4308.1	-1.130
FM 158-Bryan-SP D	0.62	1.80	1307.3	-0.994
SH 40-College St-SP TyC	0.94	0.50	256.9	-0.785
US 59-Texarkana-SMA D	0.82	0.79	79.8	-0.698

Table E.2. Prediction Performance by Project.

Project	Prediction Within Calibration Lot*				Prediction for Subsequent Lots		
	R ²	RMSE	Bias (%)	Margin of Error (%)	RMSE	Bias (%)	Margin of Error (%)
SH 6-Vlly Mills-DG D	NA	NA	-0.88	±0.47	1.61	0.78	±2.84
SH 30-Cllg St-SMA C	0.93	0.21	-0.04	±0.5	1.28	0.98	±1.66
SH 6-Lk Waco-TOM C	0.81	0.50	-0.42	±0.65	1.98	-1.62	±2.3
RELLIS-DG D	0.82	0.84	-0.20	±1.63	2.36	2.17	±1.87
RELLIS-TOM F	0.53	1.62	0.17	±3.22	NA	NA	NA
SL 79-Del Rio-DG B	0.84	0.95	-0.31	±2.16	0.89	0.31	±1.7
SH 149-Beckville-SP C	0.79	0.77	0.43	±1.54	1.02	0.35	±1.96
IH 45-Huntsvll-SMA C	0.02	1.60	-0.66	±3.5	1.64	-0.48	±3.21
FM 158-Bryan-SP D	-2.84	1.80	1.72	±1.32	2.20	2.05	±1.66
SH 40-Cllg St-SP TyC	-0.11	1.66	0.07	±3.98	1.27	1.06	±1.44
US 59-Txrkn-SMA D	-12.4	1.57	-0.93	±3.02	0.72	-0.30	±1.48

* Within-lot calibrations made using 66% of the calibration cores (typically 6 cores), and the remaining cores used for verification.

Red cells indicate bias greater than ±1%.

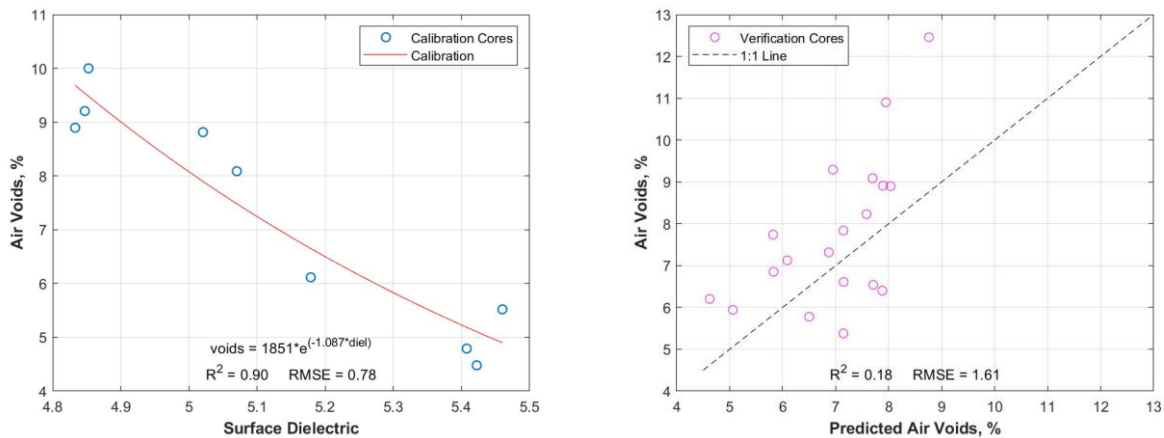


Figure E.1. SH 6-Valley Mills Calibration and Verification.

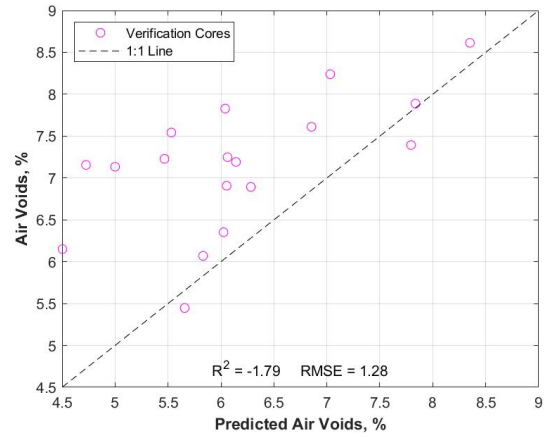
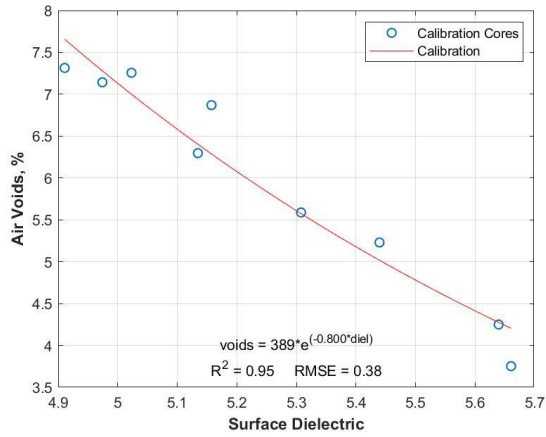


Figure E.2. SH 30-College Station Calibration and Verification.

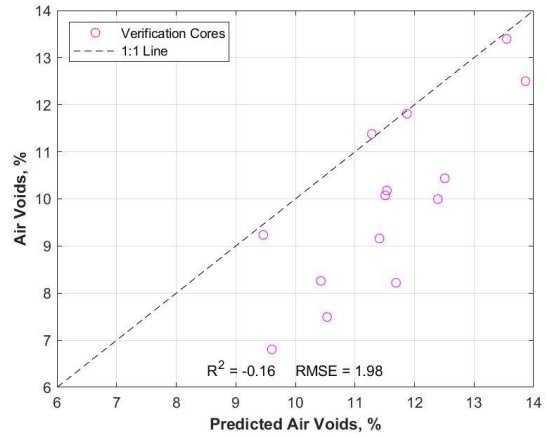
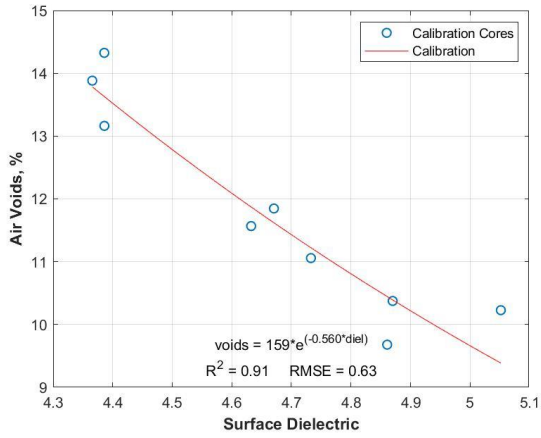


Figure E.3. SH 6-Lake Waco Calibration and Verification.

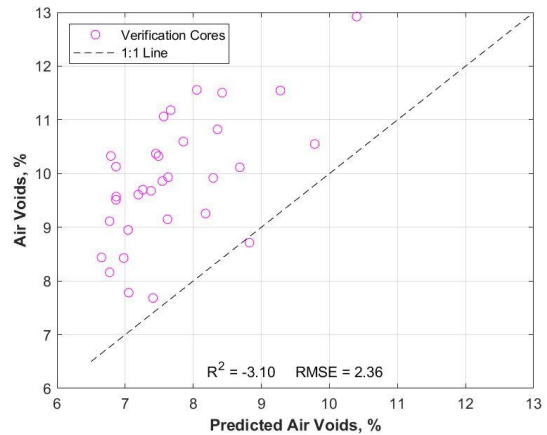
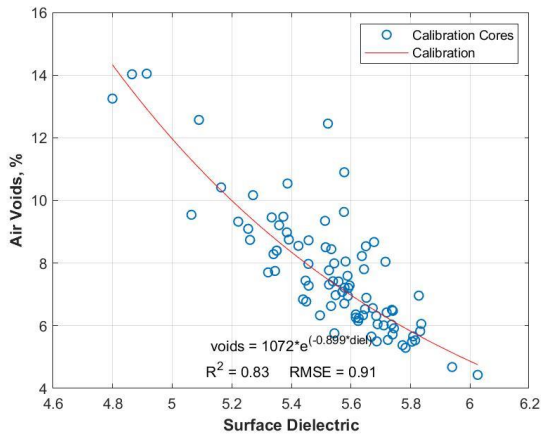


Figure E.4. RELLIS-DG D Calibration and Verification.

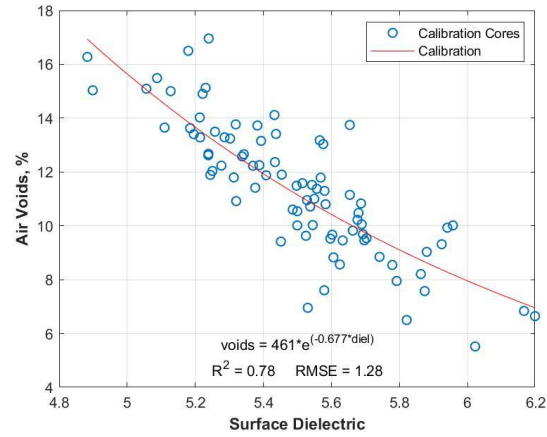


Figure E.5. RELLIS-TOM C Calibration.

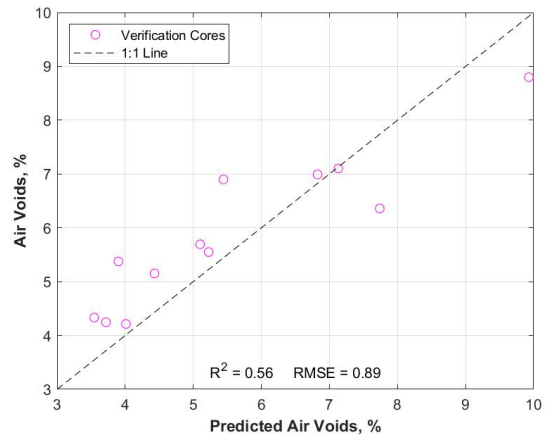
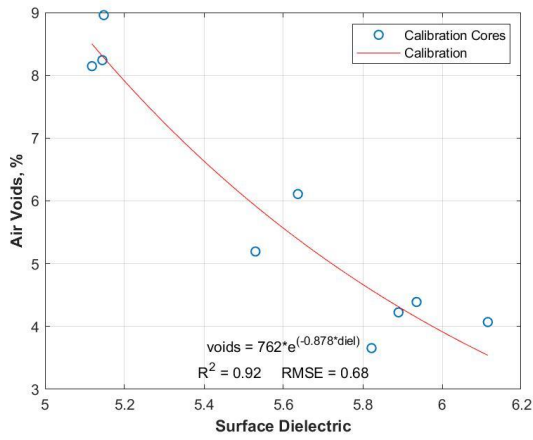


Figure E.6. SL 79-Del Rio Calibration and Verification.

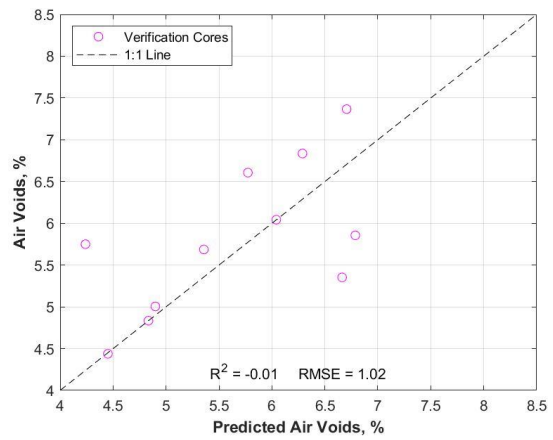
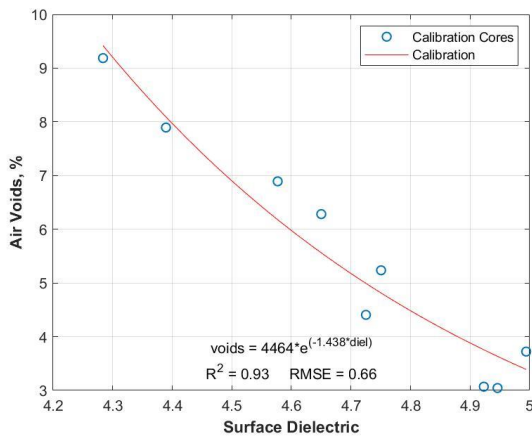


Figure E.7. SH 149-Beckville Calibration and Verification.

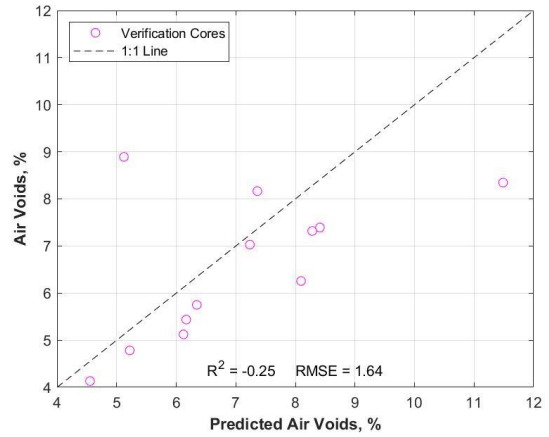
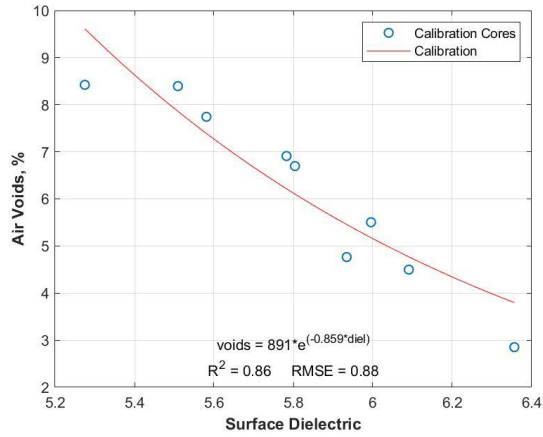


Figure E.8. IH 45-Huntsville Calibration and Verification.

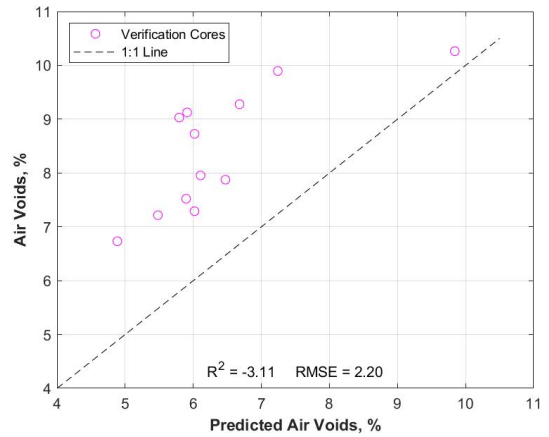
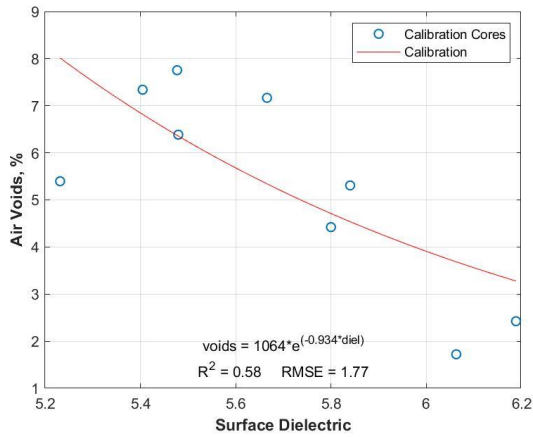


Figure E.9. FM 158-Bryan Calibration and Verification.

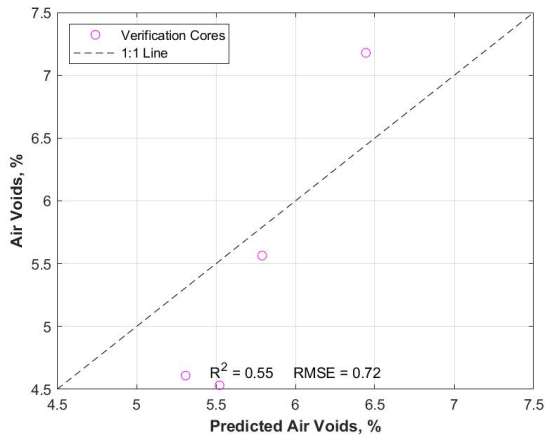
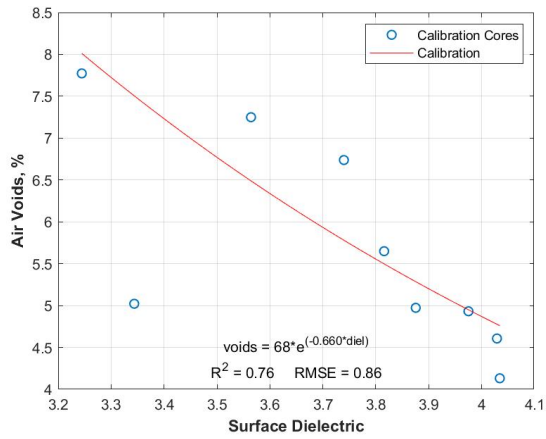


Figure E.10. US 59-Texarkana Calibration and Verification.

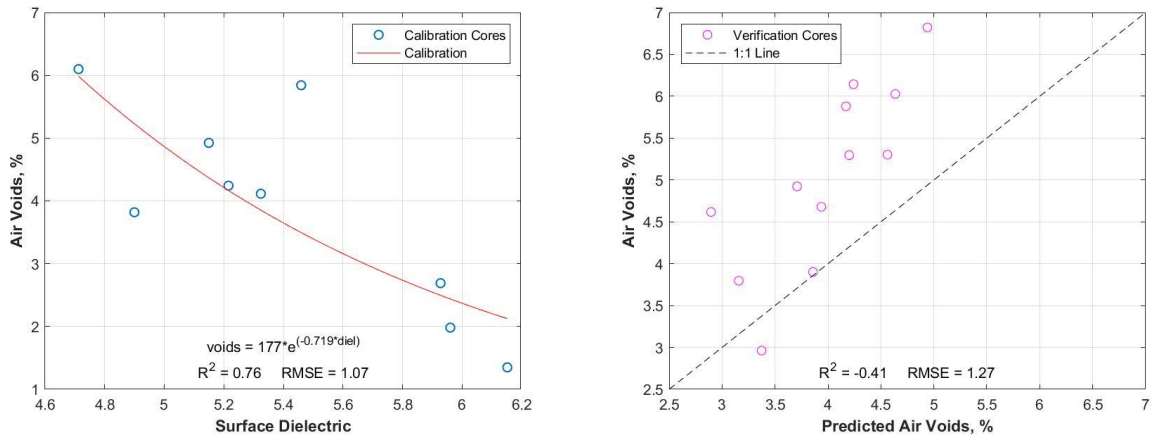


Figure E.11. SH 40-College Station Calibration and Verification.

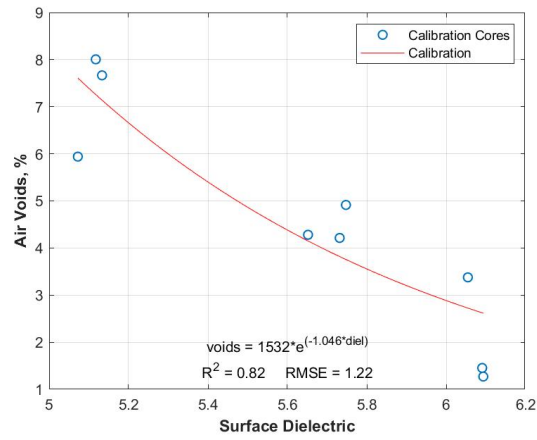


Figure E.12. US 287-Groveton Calibration.

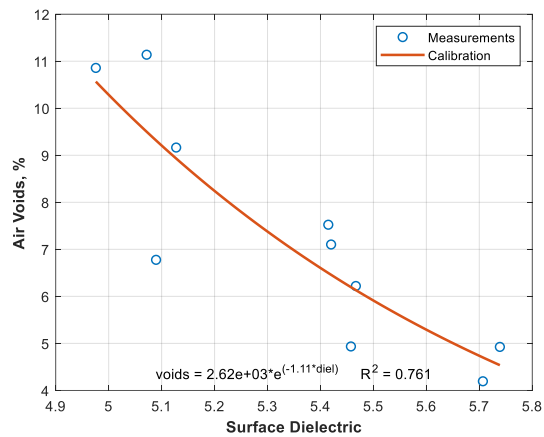


Figure E.13. SS 248-Tyler Calibration.

Table E.3. Predicted Air Void Summary Statistics.

Project	Lot	Predicted Air Voids (%)				
		Average	St. Dev.	Median	5th_Percentile	95th Percentile
SH 6-Valley Mills	6-1	6.9	1.1	6.9	5.3	8.9
	6-2	6.9	1.2	6.9	5.0	9.0
	8-1	6.9	1.3	6.8	4.9	9.2
	8-2	7.0	1.2	6.9	5.3	8.9
	9-1	7.7	1.6	7.4	5.7	10.6
	11-1	5.7	3.2	5.6	4.0	7.6
	11-2	5.6	0.9	5.5	4.2	7.2
SH 30-College Station	2-1	5.9	1.0	5.8	4.3	7.5
	3-1	5.8	1.0	5.7	4.4	7.6
	3-2	6.3	0.8	6.2	5.0	7.6
	3-3	6.3	0.9	6.3	5.1	7.8
	4-2	5.7	0.9	5.7	4.2	7.2
	4-3	5.7	0.9	5.6	4.3	7.2
	4-4	5.4	1.0	5.3	4.0	7.0
SH 6-Lake Waco	2-1	11.3	1.2	11.2	9.5	13.5
	3-1	10.6	1.2	10.6	8.8	12.4
	3-2	11.4	1.0	11.3	9.8	13.0
	3-3	11.2	1.2	11.3	9.3	13.1
	8-1	12.0	1.6	11.9	9.6	14.8
	8-2	11.8	1.1	11.8	10.0	13.7
SL 79-Del Rio	6-2	4.6	0.9	4.5	3.3	6.3
	6-3	4.3	0.7	4.3	3.3	5.5
	7-1	5.0	0.8	4.9	3.8	6.4
	7-2	4.3	0.7	4.3	3.3	5.5
	7-3	4.9	0.7	4.9	3.8	6.2
	8-2	4.3	0.7	4.2	3.2	5.5
	8-3	4.2	0.7	4.1	3.2	5.4
	8-4	4.1	0.9	4.1	3.0	5.4
SH 149-Beckville	2-3	5.7	1.4	5.5	3.6	8.2
	2-4	4.2	1.6	3.8	2.2	7.0
	3-1	5.9	1.6	5.7	3.8	8.5
	2-2	5.6	1.3	5.5	3.7	7.9
	4-1	6.4	1.4	6.2	4.4	9.1
	4-2	5.6	1.0	5.5	4.0	7.4
	4-3	4.6	1.0	4.5	3.3	6.3

Table E.3. Predicted Air Void Summary Statistics (Continued).

Project	Lot	Predicted Air Voids (%)				
		Average	St. Dev.	Median	5th_Percentile	95th Percentile
IH 45-Huntsville	4-1	6.0	1.2	5.9	4.4	7.9
	6-1	6.8	3.3	6.3	4.5	10.6
	6-2	6.9	1.9	6.7	4.4	10.2
	6-3	6.3	1.9	6.2	3.9	9.1
	7-1	5.8	1.3	5.5	4.1	8.2
	7-2	6.8	1.9	6.4	4.2	10.1
	7-3	6.5	1.9	6.0	4.2	10.1
FM158-Bryan	2-1	5.3	4.0	5.0	3.4	7.6
	4-1	6.4	3.6	6.1	4.3	9.1
	4-2	6.8	1.2	6.7	5.2	9.0
	5-1	6.4	1.6	6.2	4.3	9.1
	5-2	6.7	1.8	6.4	4.3	9.7
	6-1	5.6	1.3	5.5	3.8	7.9
	6-2	6.1	1.3	6.0	4.3	8.4
US59-Texarkana	2-4	5.4	0.5	5.4	4.7	6.2
	3-1	5.4	0.5	5.4	4.7	6.2
	3-2	5.5	0.4	5.4	4.8	6.2
	3-3	5.4	0.4	5.4	4.8	6.1
SH40-College Station	5-1	4.0	0.8	3.9	2.9	5.2
	5-2	3.7	0.7	3.6	2.8	5.3
	5-3	3.6	0.9	3.4	2.5	5.3
	6-1	3.9	0.7	3.8	3.0	5.2
	6-2	3.9	0.8	3.8	2.8	5.2
	6-3	3.8	0.7	3.7	2.9	5.4
	7-1	4.3	0.8	4.2	3.0	5.6

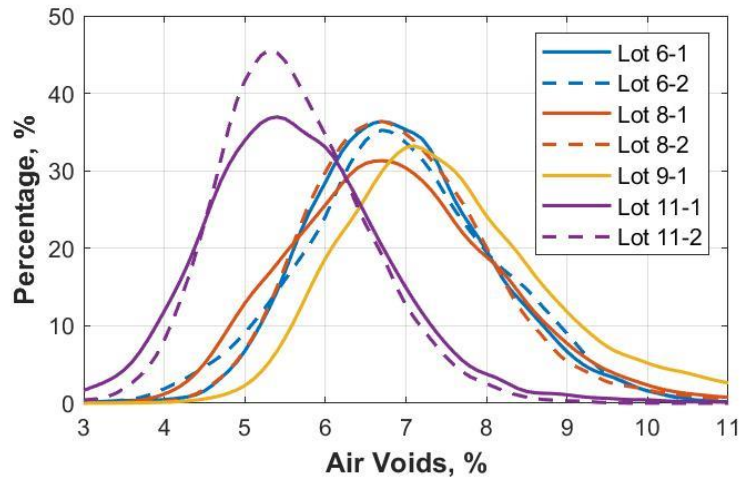


Figure E.14. SH 6-Valley Mills Air Void Distributions.

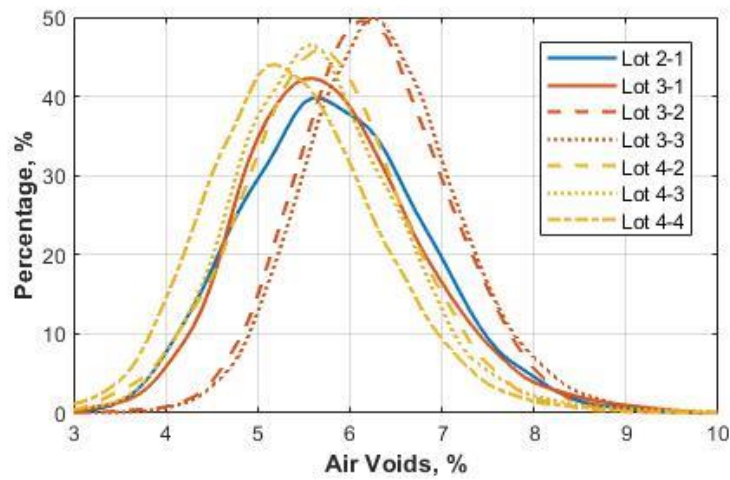


Figure E.15. SH 30-College Station Air Void Distributions.

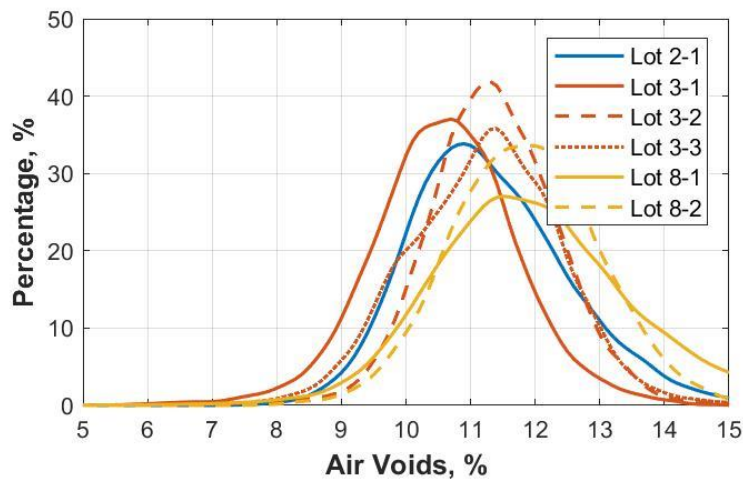


Figure E.16. SH 6-Lake Waco Air Void Distributions.

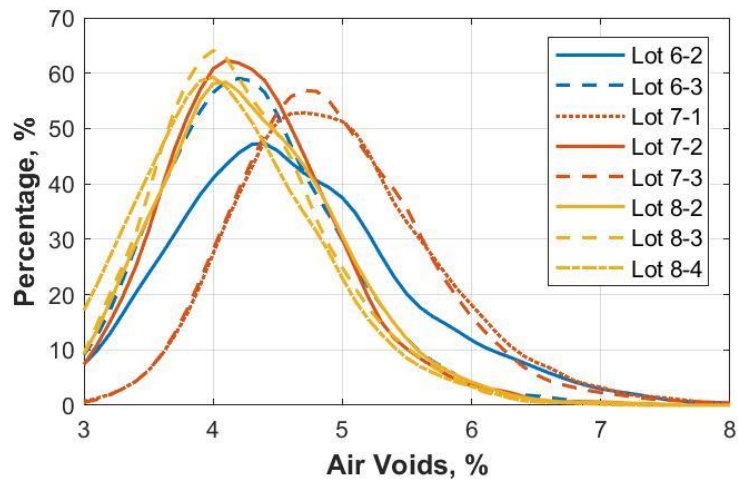


Figure E.17. SL 79-Del Rio Air Void Distributions.

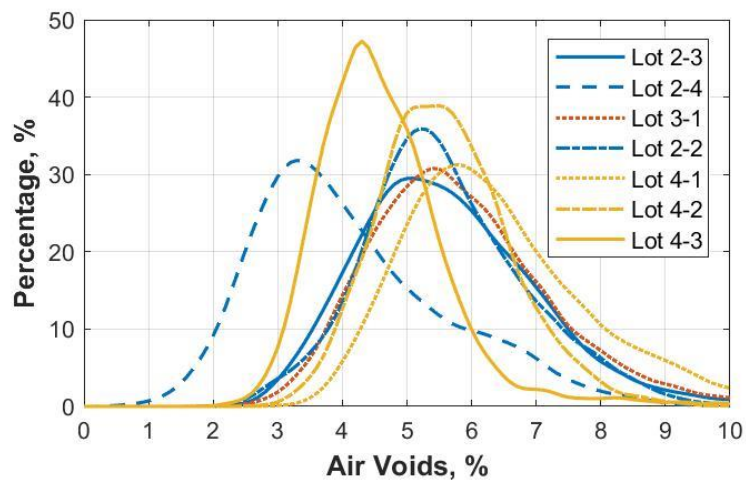


Figure E.18. SH 149-Beckville AirVoid Distributions.

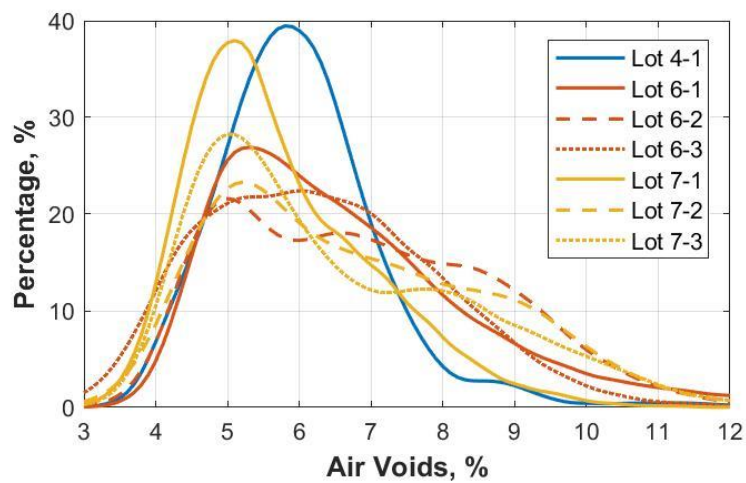


Figure E.19. IH 45-Huntsville Air Void Distributions.

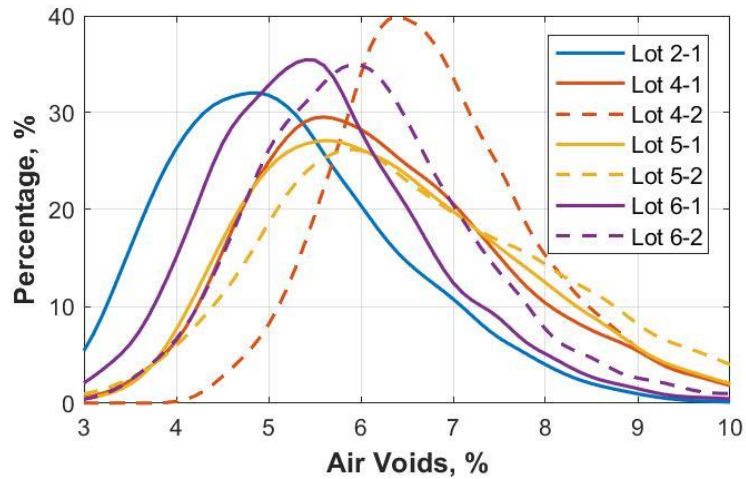


Figure E.20. FM 158-Bryan Air Void Distributions.

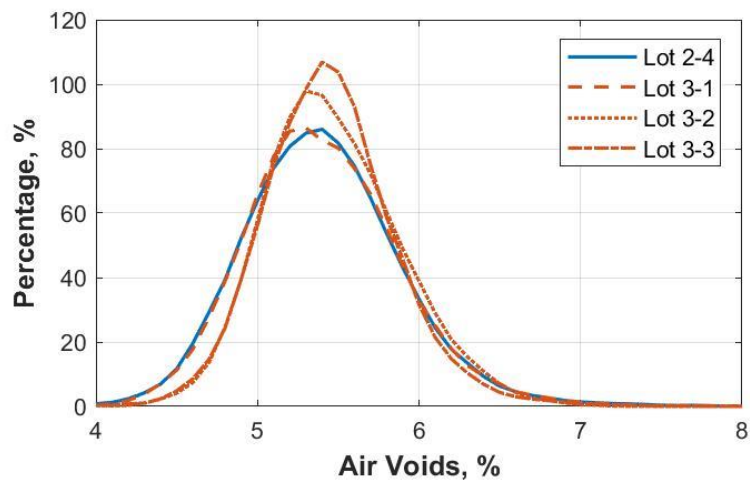


Figure E.21. US 59-Texarkana Air Void Distributions.

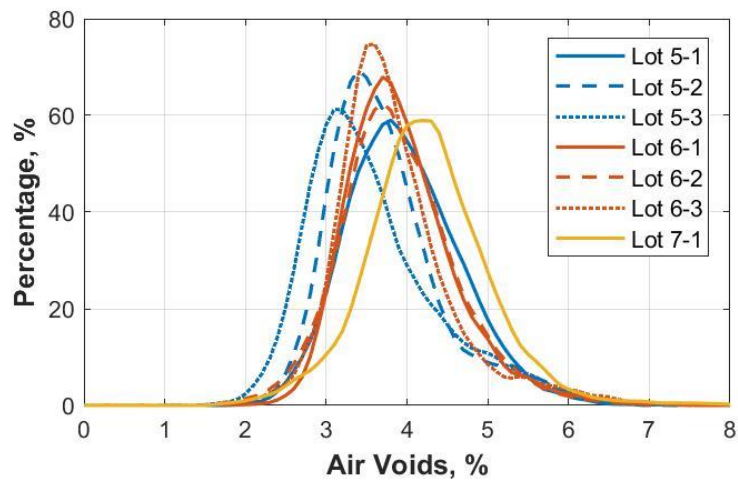


Figure E.22. SH 40-College Station Air Void Distributions.

LABORATORY SENSITIVITY TESTING

Table E.4. Laboratory Results for Dielectric Sensitivity Study.

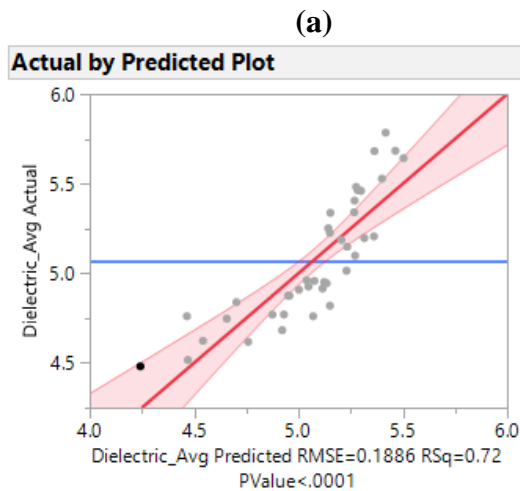
Project	Date Tested	Design						Actual					Surface Dielectric	
		AC Rank	Coarse Agg Rank	Voids Rank	Asphalt Content (%)	Coarse Agg Sub. (%)	Air Voids (%)	Asphalt Content (%)	Gmm	Gmb	Coarse Agg SG	Air Voids (%)	Average	St Dev
SH 6-Valley Mills-DG D	10/24/2018	2	2	1	5.2	0	3.3	5.39	2.420	2.265	2.567	6.43	5.01	0.08
SH 6-Valley Mills-DG D	10/24/2018	2	2	3	5.2	0	8.5	5.97	2.412	2.219	2.567	8.01	4.96	0.13
SH 6-Valley Mills-DG D	10/24/2018	1	2	2	4.7	0	5.9	5.12	2.424	2.233	2.567	7.89	4.82	0.16
SH 6-Valley Mills-DG D	10/24/2018	3	2	2	5.7	0	5.9	6.04	2.407	2.226	2.567	7.50	4.76	0.06
SH 6-Valley Mills-DG D	10/24/2018	2	1	2	5.2	-12	5.9	5.96	2.419	2.216	2.583	8.37	4.88	0.15
SH 6-Valley Mills-DG D	10/24/2018	2	3	2	5.2	12	5.9	5.50	2.413	2.214	2.551	8.22	4.94	0.05
SH 6-Valley Mills-DG D	10/24/2018	1	3	1	4.7	12	3.3	5.16	2.425	2.285	2.551	5.80	5.21	0.06
SH 6-Valley Mills-DG D	10/24/2018	3	1	3	5.7	-12	8.5	6.01	2.416	2.190	2.583	9.36	4.77	0.18
SH 30-College St-SMA C	10/23/2018	2	2	1	6	0	3	6.35	2.377	2.330	2.554	1.97	5.64	0.20
SH 30-College St-SMA C	10/23/2018	2	2	3	6	0	5.5	6.22	2.384	2.274	2.554	4.61	5.20	0.14
SH 30-College St-SMA C	10/23/2018	1	2	2	5.5	0	3	5.77	2.405	2.324	2.554	3.38	5.68	0.18
SH 30-College St-SMA C	10/23/2018	3	2	2	6.5	0	8	6.52	2.380	2.256	2.554	5.21	5.15	0.12
SH 30-College St-SMA C	10/23/2018	2	1	2	6	-12	5.5	6.43	2.385	2.269	2.555	4.84	5.41	0.11
SH 30-College St-SMA C	10/23/2018	2	3	2	6	12	5.5	6.71	2.380	2.274	2.553	4.47	5.10	0.11
SH 30-College St-SMA C	10/23/2018	1	3	1	5.5	12	3	6.20	2.409	2.322	2.553	3.59	5.53	0.22
SH 30-College St-SMA C	10/23/2018	3	1	3	6.5	-12	8	6.57	2.387	2.241	2.555	6.13	5.34	0.07
SH 6-Lake Waco-TOM C	10/24/2018	2	2	1	6.6	0	7.4	7.31	2.400	2.213	2.622	7.82	4.84	0.04
SH 6-Lake Waco-TOM C	10/24/2018	2	2	3	6.6	0	12.6	7.47	2.394	2.140	2.622	10.61	4.52	0.05
SH 6-Lake Waco-TOM C	10/24/2018	1	2	2	6.1	0	10	6.46	2.426	2.189	2.622	9.75	4.75	0.09
SH 6-Lake Waco-TOM C	10/24/2018	3	2	2	7.1	0	10	7.34	2.395	2.159	2.622	9.86	4.62	0.13
SH 6-Lake Waco-TOM C	10/24/2018	2	1	2	6.6	-12	10	7.33	2.418	2.201	2.664	8.97	4.76	0.05
SH 6-Lake Waco-TOM C	10/24/2018	2	3	2	6.6	12	10	6.90	2.394	2.162	2.579	9.66	4.62	0.09
SH 6-Lake Waco-TOM C	10/24/2018	1	3	1	6.1	12	7.4	6.26	2.404	2.201	2.579	8.42	4.77	0.04
SH 6-Lake Waco-TOM C	10/24/2018	3	1	3	7.1	-12	12.6	7.37	2.417	2.132	2.664	11.80	4.48	0.04

Table E.4. Laboratory Results for Dielectric Sensitivity Study. (continued)

Project	Date Tested	Design						Actual					Surface Dielectric	
		AC Rank	Coarse Agg Rank	Voids Rank	Asphalt Content (%)	Coarse Agg Sub. (%)	Air Voids (%)	Asphalt Content (%)	Gmm	Gmb	Coarse Agg SG	Air Voids (%)	Average	St Dev
SH 149-Beckville-SP C	10/24/2018	2	2	1	5.3	0	3	5.72	2.478	2.370	2.632	4.36	4.95	0.10
SH 149-Beckville-SP C	10/24/2018	2	2	3	5.3	0	8	6.08	2.460	2.302	2.632	6.42	4.68	0.08
SH 149-Beckville-SP C	10/24/2018	1	2	2	4.8	0	5.5	5.64	2.484	2.370	2.632	4.58	4.92	0.06
SH 149-Beckville-SP C	10/24/2018	3	2	2	5.8	0	5.5	6.80	2.449	2.345	2.632	4.25	4.91	0.12
SH 149-Beckville-SP C	10/24/2018	2	1	2	5.3	-12	5.5	5.95	2.464	2.358	2.602	4.29	5.19	0.07
SH 149-Beckville-SP C	10/24/2018	2	3	2	5.3	12	5.5	6.03	2.479	2.357	2.659	4.91	4.88	0.06
SH 149-Beckville-SP C	10/24/2018	1	3	1	4.8	12	3	5.64	2.497	2.400	2.659	3.89	4.96	0.06
SH 149-Beckville-SP C	10/24/2018	3	1	3	5.8	-12	8	6.42	2.440	2.303	2.602	5.61	4.93	0.04
SL 79-Del Rio-DG B	11/23/2018	2	2	1	4.5	0	3	5.12	2.451	2.328	2.569	5.04	5.68	0.10
SL 79-Del Rio-DG B	11/23/2018	2	2	3	4.5	0	8	5.14	2.455	2.264	2.569	7.78	5.23	0.11
SL 79-Del Rio-DG B	11/23/2018	1	2	2	4	0	5.5	4.75	2.470	2.304	2.569	6.75	5.48	0.20
SL 79-Del Rio-DG B	11/23/2018	3	2	2	5	0	5.5	5.32	2.438	2.292	2.569	5.99	5.34	0.15
SL 79-Del Rio-DG B	11/23/2018	2	1	2	4.5	-12	5.5	4.95	2.456	2.293	2.563	6.61	5.46	0.09
SL 79-Del Rio-DG B	11/23/2018	2	3	2	4.5	12	5.5	4.96	2.456	2.312	2.575	5.86	5.46	0.20
SL 79-Del Rio-DG B	11/23/2018	1	3	1	4	12	3	4.58	2.474	2.352	2.575	4.91	5.78	0.06
SL 79-Del Rio-DG B	11/23/2018	3	1	3	5	-12	8	5.36	2.437	2.247	2.563	7.79	5.25	0.12

STATISTICS

Table E.5. Dielectric Sensitivity Study Statistical Results:
(a) Model 1, (b) Model 2, and (c) Model 3.



Summary of Fit

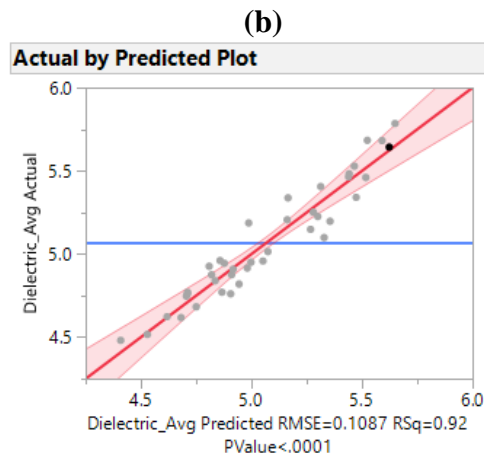
RSquare	0.724724
RSquare Adj	0.701784
Root Mean Square Error	0.18859
Mean of Response	5.07108
Observations (or Sum Wgts)	40

Analysis of Variance

Source	DF	Sum of Squares	Mean Square	F Ratio
Model	3	3.3708866	1.12363	31.5926
Error	36	1.2803850	0.03557	Prob > F
C. Total	39	4.6512716		<.0001*

Parameter Estimates

Term	Estimate	Std Error	t Ratio	Prob> t
Intercept	15.273472	2.297724	6.65	<.0001*
AC_Perc	-0.119897	0.044979	-2.67	0.0114*
CoarseAgg_SG	-3.468216	0.926989	-3.74	0.0006*
Voids_Perc	-0.076843	0.014439	-5.32	<.0001*



Summary of Fit

RSquare	0.918744
RSquare Adj	0.90097
Root Mean Square Error	0.108677
Mean of Response	5.07108
Observations (or Sum Wgts)	40

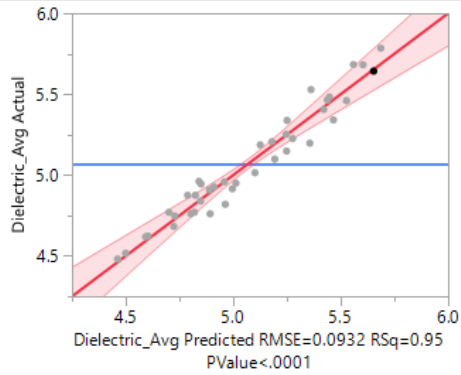
Analysis of Variance

Source	DF	Sum of Squares	Mean Square	F Ratio
Model	7	4.2733299	0.610476	51.6884
Error	32	0.3779418	0.011811	Prob > F
C. Total	39	4.6512716		<.0001*

Parameter Estimates

Term	Estimate	Std Error	t Ratio	Prob> t
Intercept	6.4797945	2.651319	2.44	0.0202*
Voids_Perc	-0.105352	0.017951	-5.87	<.0001*
CoarseAgg_SG	-0.078637	1.048723	-0.07	0.9407
AC_Perc	-0.085687	0.055652	-1.54	0.1335
Project[SH 149-Beckville-SP C]	-0.325942	0.066416	-4.91	<.0001*
Project[SH 30-College St-SMA C]	0.0954944	0.071636	1.33	0.1919
Project[SH 6-Lake Waco-TOM C]	0.0129058	0.071594	0.18	0.8581
Project[SH 6-Valley Mills-DG D]	-0.064355	0.05264	-1.22	0.2304

(c)

Actual by Predicted Plot**Summary of Fit**

RSquare	0.947749
RSquare Adj	0.927221
Root Mean Square Error	0.093166
Mean of Response	5.07108
Observations (or Sum Wgts)	40

Analysis of Variance

Source	DF	Sum of Squares	Mean Square	F Ratio
Model	11	4.4082368	0.400749	46.1702
Error	28	0.2430348	0.008680	Prob > F
C. Total	39	4.6512716		<.0001*

Parameter Estimates

Term	Estimate	Std Error	t Ratio	Prob> t
Intercept	-50.98008	23.83654	-2.14	0.0413*
Voids_Perc	-0.118315	0.016669	-7.10	<.0001*
CoarseAgg_SG	22.561547	9.33405	2.42	0.0224*
AC_Perc	-0.126467	0.051376	-2.46	0.0203*
Project[SH 149-Beckville-SP C]	-0.976187	0.333167	-2.93	0.0067*
Project[SH 30-College St-SMA C]	3.1926274	1.271055	2.51	0.0181*
Project[SH 6-Lake Waco-TOM C]	-0.795603	0.318661	-2.50	0.0187*
Project[SH 6-Valley Mills-DG D]	-0.845518	0.318828	-2.65	0.0130*
Project[SH 149-Beckville-SP C]*(CoarseAgg_SG-2.58861)	-27.02458	9.444478	-2.86	0.0079*
Project[SH 30-College St-SMA C]*(CoarseAgg_SG-2.58861)	90.944021	37.05563	2.45	0.0206*
Project[SH 6-Lake Waco-TOM C]*(CoarseAgg_SG-2.58861)	-20.40139	9.348854	-2.18	0.0376*
Project[SH 6-Valley Mills-DG D]*(CoarseAgg_SG-2.58861)	-21.0013	9.526321	-2.20	0.0359*

